UNIVERSITÄT HAMBURG
DEPARTMENT PHYISK

The structural and magnetic properties of Fe/native-oxide systems resolved by x-ray scattering and spectroscopy methods

Dissertation zur Erlangung des Doktorgrades des Fachbereichs Physik der Universität Hamburg

vorgelegt von

Sébastien Couet
aus Villers-la-ville, Belgien

Hamburg
2008

Gutachter der Dissertation:

PD. Dr. R. Röhlsberger
Prof. Dr. H.P. Oepen

Gutachter der Disputation:

PD. Dr. R. Röhlsberger
Prof. Dr. W. Wurth

Datum der Disputation:

03 december 2008

Vorsitzender des Prüfungsausschusses:

Dr. M. Martins

Vorsitzender des Promotionsausschusses:

Prof. Dr. J. Bartels

MIN-Dekan der Fakultät Physik:

Prof. Dr. A. Frühwald

Abstract

Since the discovery of the giant magnetoresistance (GMR) effect in metallic magnetic multilayers and its industrial application in magnetic read heads, the data storage density and reading speed of hard disks steadily increased. But now the point is reached where conventional conductive multilayer structures suffer from parasitic eddy currents which decrease the signal to noise ratio of the system. To tackle this problem, new classes of materials have to be studied. One approach is to introduce ultra thin oxide layers in a metallic iron structure to reduce the conductivity while keeping a high net magnetization. This can be achieved by alternating metal deposition and controlled oxidation to produce metal/metal-oxide multilayers. However, the magnetic structure that forms in such multilayer is still rather unexplored.

The aim of this work was to achieve a better understanding of the magnetic structure that forms in such iron/native-oxide multilayers. For that purpose, x-ray and neutron scattering experiments were carried out to determine the magnetic structure and its evolution in *ex-situ* and *in-situ* experiments, respectively. It was found that a non-collinear magnetic coupling appears between the metal layers, which is mediated by the antiferromagnetically ordered oxide layer in between. The use of isotope sensitive scattering techniques (namely nuclear resonant scattering and neutron reflectometry) allowed to resolve the magnetic depth profile of the system, showing that the buried oxide carries a net magnetic moment.

The chemical and magnetic structure of the buried oxide was studied by *in-situ* x-ray absorption spectroscopy and nuclear resonant scattering. After oxidation, the layer exhibits a mixture of different oxide phases and incorporates 10 to 15% of Fe with metallic character. Upon deposition of only one atomic layer of metallic Fe, the layer reduces to a single phase FeO-like oxide. This structural change does not lead to a magnetically ordered oxide. Surprisingly, it is observed that the magnetism in the oxide is stabilized only once the layer is covered by several nanometer of Fe.

These findings lead to a comprehensive picture of the structure and magnetic properties of the buried oxide, paving the way for tailored magnetic properties in Fe/native-oxide systems. The results presented in this work lay the foundation for further studies of this relatively unexplored class of systems.

Zusammenfassung

Die Entdeckung des GMR-effekts (engl. giant magneto resistance, deutsch "Riesenmagnetowiderstand") in magnetischen Vielfachschichten und seine industrielle Anwendung in Magnetfeldleseköpfen initiierte einen Prozess stetiger Erhöhung der Festplattenspeicherdichte und ihrer Auslesegeschwindigkeit. Doch dieser Prozess kann durch konventionelle, elektrisch leitendende Vielfachschichtsysteme nicht beliebig fortgesetzt werden, da in diesen bereits heutezutage parasitäte Wirbelströme eine signifikante Verschlechterung des Signal-Rausch-Verhältnisses verursachen. Neue Materialien werden gesucht, um diese Problemstellung zu lösen. Ein Ansatz fundiert auf der Verwendung von ultradünnen Oxidschichten in einer metallischen Eisenumgebung/matrix, um die elektrische Leitfhigkeit abzusenken aber gleichzeitig eine hohe Nettomagnetisierung zu erhalten. Dieses Prinzip kann relativ einfach durch die abwechselnde Beschichtung von Metallschichten und ihre kontrollierte Oxidation realisiert werden. Obwohl die Funktionalität einer solchen magnetischen Schichtstruktur vor einiger Zeit gezeigt werden konnte wurde ihr allgemeines Magnetisierungs- bzw. magnetisches Kopplungsverhalten nicht genauer erforscht.

Als wesentliches Ziel dieser Arbeit galt es, ein besseres Verständnis über die allgemeine magnetisches Struktur in einer solchen Eisen/native-Eisenoxid Vielschichtstruktur zu erlangen. Röntgen- und Neutronenstreuexperimente wurden diesbezüglich *ex-situ* und *in-situ* durchgeführt, um die magnetische Struktur und ihr feldabhängiges Verhalten zu bestimmen. Als ein erstes, wesentliches Ergebnis konnte eine nicht kollineare, magnetische Kopplung der Metallschichten bestimmt werden, die durch eine antiferromagnetische Struktur der Oxidschichten vermittelt wird. Des weiteren offenbarte die Kombination beider Messmethoden das magnetische Tiefenprofil des Systems und ein resultierendes magnetisches Moment des eingebetteten Eisenoxides.

Die chemische und die magnetische Struktur des eingebetteten Oxides wurde mittels einer kombinierten Studie aus *in-situ* Röntgenabsorptionsspektroskopie und (in-situ) Kernresonanzstreuung bestimmt. Diese ergab, dass die kontrollierte Oxidation einer Eisenschicht ein Gemisch aus unterschiedlichen Oxidphasen erzeugt, das zusätzlich 10% bis 15% Einschlüsse aus metallischem Eisen beinhaltet. Die Auftragung einer dünnen Schicht aus metallischem Eisen reduziert nun die komplette Oxidschicht zu einphasigem, FeO-artigem Oxid.

Diese experimentelle Beobachtung führt zu einem umfassenden Bild über die Struktur und die magnetischen Eigenschaften des eingebetten Oxides und zeigt damit einen Weg um die magnetischen Eigenschaften der Eisen/native-Eisenoxid Vielschichtstrukturen zu variieren beziehungsweise zu optimieren. Die Ergebnisse dieser Arbeit können nicht als abgeschlossen gelten und sollten weitere Untersuchungen dieser Klasse von noch relativ unerforschten Systemen nach sich ziehen.

Contents

Chapter 1

Introduction

In 2007, the nobel prize for physics was awarded to P. Grünberg and A. Fert for their common discovery of the giant magnetoresistance (GMR) effect in the late 80's. Ten years later, the first giant magnetoresisitive read heads (based on GMR effect) started to be used in consumer hard drive technology and enabled a significant increase in the data storage density and reading speed.

The GMR effect is based on an *interlayer* magnetic coupling arising between ferromagnetic layers separated by a few nanometer thick non-magnetic metallic spacer layers. Because of the extremely small layer thicknesses involved, and the intrinsically short ranged interactions, it is often said that GMR is one of the first applications of nanotechnology research to large scale industrial production.

With the availability of high sensitivity and high frequency GMR read heads, a great part of research has been devoted to the increase of the data storage density by reducing the size of the magnetic bits on the disks. This led to a steady increase of storage capacity over the last decade, going from magnetic domains magnetized parallel to the disk plane to, more recently, out of plane magnetization. This evolution was possible without significant changes of the GMR head technology.

However, with increasing magnetic bit packing density, the reading speed and therefore the magnetic field switching frequency inside the read head is continuously increasing. Following Lenz's rule, variation of the magnetic field leads to the appearance of parasitic eddy currents which can seriously decrease the signal to noise ratio at high frequency. While a couple of actions can be taken to increase the signal (*e.g.* reduce the head-surface distance or use higher magnetic moment materials), it becomes particularly important to reduce the noise induced by the eddy currents.

In that direction, Beach *et al.* [1, 2] have carried out a pioneering work, proposing to use ferromagnetic layers embedding ultrathin oxide layers to prevent the formation of eddy currents. They proposed to use a very simple preparation scheme were nanometer thick oxide layers are prepared by controlled oxidation of a transition metal, effectively producing metal/native oxide (MNOM) multilayers. These type of systems combine several advantages: The introduction of the native oxide in the structure increases the resistivity (compared to a pure metallic layer) and

effectively reduces the formation of eddy currents well into the gigahertz frequency regime. One can also easily change the thickness of the metal layer to tune the overall resistivity of the structure. It was also shown that such oxide layer carries a net magnetic moment [3], which enables one to keep an overall high net magnetization of the multilayer. The proposed structure therefore allows to reduce the resistivity without compromising the net magnetization.

However, Beach *et al.* did not consider possible magnetic coupling effects arising between the magnetic metal and the magnetic oxide. Furthermore, they carried out *ex-situ* studies, focusing on the layer integrated magnetic properties of the system. The key information on how magnetism appears in the buried oxide is therefore missing. These considerations triggered the study presented in this work. The aim was to study in a layer resolved manner and *in-situ* the magnetic properties of the buried oxide during its formation using the isotope sensitive technique of nuclear resonant scattering (NRS) of synchrotron radiation. It soon turned out that the presence of magnetism in both metal and oxide layers leads to the appearance of strong magnetic coupling effects between the adjacent layers. From there on, the study aimed at a quantitative and direct resolution of the composition of the free and buried native oxide by *in-situ* x-ray absorption spectroscopy. Surprisingly, this study showed that the native oxide adopts a single phase FeO-like structure upon deposition of Fe on its free surface. This crucial knowledge then allowed to better understand the magnetic transition observed in the oxide. The rest of the work was devoted to the study of the interaction between the metal and the adjacent oxide. For that purpose, a layer resolved magnetic study of Fe/Fe-oxide multilayers was carried out by combining the two isotope sensitive techniques of NRS and polarized neutron reflectometry (PNR).

1.1 Outline

This thesis is organized around four articles published in peer reviewed journals. The first three chapters of this work are meant to provide a basic background on the effects discussed in the articles, together with a review of the state-of-the-art knowledge on such magnetic multilayers. The first chapter gives a general overview on magnetic coupling phenomena arising in thin films and multilayered structures. A special emphasis is given on the different *interlayer* magnetic coupling effects appearing between separated magnetic layers. The second chapter is a brief introduction on the experimental techniques used in the course of this study. The common basis for the theoretical description of grazing incidence NRS and PNR techniques should allow the reader to understand the similarities and particularities of both techniques for the study of magnetic thin films. The third chapter gives an introduction to the science of the oxidation of iron surfaces. Chapter 5 deals with a discussion of the typical structure of metal/oxide multilayers, as determined within this work. Chapter 6 and 7 summarize the results obtained and complements the articles with additional results. These give the reader a deeper insight in all the

findings related to this thesis. While the first four chapters can be read stand-alone, it is recommended to read the articles before reading chapters 6 and 7, as a great part of the arguments presented are supported by the articles.

1.2 List of published articles

The results of this works are summarized in four peer reviewed articles. A reprint of these manuscripts is given at the end of the present work. These papers are directly related to the study of Fe/native-oxide multilayers. They will be referenced throughout this manuscript by their bold roman number.

- **Paper I:** S. Couet, Th. Diederich, K. Schlage, R. Röhlsberger, Rev. Sci. Instrum. **79**, 093908 (2008)
  A compact UHV deposition system for in-situ study of ultrathin films via hard x-ray scattering and spectroscopy

- **Paper II:** Th. Diederich, S. Couet, R. Röhlsberger, Phys. Rev. B **76**, 054401 (2007)
  Non collinear coupling of iron layers through native iron oxide spacer layer

- **Paper III:** S. Couet, K. Schlage, K. Saksl, R. Röhlsberger, Phys. Rev. Lett. **101**, 056101 (2008)
  How metallic Fe controls the composition of its native oxide

- **Paper IV:** S. Couet, K. Schlage, Th. Diederich, R. Rüffer, K. Theis-Bröhl, K. Zhernenkov, B. Toperverg, H. Zabel, R. Röhlsberger, New Journal of physics, accepted (2008)
  The magnetic structure of coupled Fe/FeO multilayers revealed by nuclear resonant and neutron scattering methods

Chapter 2

Magnetic properties of multilayered structures

The magnetic interactions and coupling phenomena that appear in thin magnetic films are intrinsically short ranged. Exchange coupling is a direct interaction which determines how neighboring magnetic atoms will arrange relative to each other. In the case of compounds like FeO, indirect superexchange interaction can lead to an antiferromagnetic order between magnetic atoms separated by a diamagnetic anion. In magnetic multilayers, there exist various interlayer coupling mechanisms (RKKY type, orange peel, pinhole) which can effectively stabilize a magnetic structure over distances of several nanometers. In this chapter, a review of the relevant coupling mechanisms appearing in magnetic multilayers is presented. The chapter is organized in a "bottom up" approach, starting with the short range direct exchange interaction and ending with a review of the different long range interlayer coupling schemes relevant for this study. Emphasis is given on the magnetic coupling behavior in the case of non-metallic spacer layers, as it is the case for Fe/Fe-oxide multilayers.

2.1 Exchange interaction

The first step towards interatomic magnetic correlations is to understand the origin of the atomic magnetic moment, which is determined by the atom's electronic shell configuration. In principle, each electron of an atom carries a magnetic moment μ which is the vectorial sum of two terms: the orbital magnetic moment μ^O and the spin magnetic moment μ^S. Each are related to the corresponding orbital (l) and spin (s) momentum of the electron. The projection of these magnetic moments on a reference z-axis (which can be for example defined by applying an external magnetic field) yields distinctive values for each electron in an orbital:

$$\mu_z^O = \frac{e\hbar}{2m_e} m \quad ; \quad \mu_z^S = \frac{e\hbar}{m_e} s, \tag{2.1}$$

where the magnetic quantum number m takes an integer value with $-l \leq m \leq l$ and the spin quantum number $s = \pm\frac{1}{2}$. m_e is the electron mass and $\hbar$ the reduced Planck constant. The value $\frac{e\hbar}{2m_e}$ is called the Bohr magneton μ_B and is the smallest magnetic moment quanta an electron can possess.

According to Pauli's exclusion principle, two electrons cannot have the same quantum numbers. An electronic shell will be complete (or closed) when all the possible values of m and s are occupied by the electrons. Following the above relations, such closed electronic shells will not contribute to the intrinsic magnetic moment of the atom because all the individual orbital and spin momenta of the electrons are compensated.

In an open shell, the electrons fill the energy levels following Hund's rules in order to maximize the total moment of the orbital. This results in a decreasing magnetic moment per atom for the $3d$ transition metal series Fe ($3d^6$, $2.2\,\mu_B$), Co ($3d^7$, $1.7\,\mu_B$) and Ni ($3d^8$, $0.5\,\mu_B$). The non integer value of the magnetic moment is due to the band mixing of the $3d$ and $4s$ electron band (which results in a non integer value of the number of electrons in the d band).

The above mentioned electronic structure can be used to describe the ground state of most atoms. However, this configuration is modified by the presence of neighboring atoms. For example, a two electron system such as the H_2 molecule possess (in its ground state) two possible configurations with the two electron spins aligned either parallel or antiparallel. There exists an energy difference between these two states which is called the exchange energy. This energy term arises as an additional contribution to the pure electrostatic Coulomb interaction and is directly due to the fact that the two electron wavefunctions have to be antisymmetric upon exchange of the electrons. The corresponding exchange Hamiltonian is defined by

$$H = -2J_{ij}\boldsymbol{S}_i \cdot \boldsymbol{S}_j \tag{2.2}$$

where J_{ij} is the exchange integral between the two electron wavefunctions having the spin matrices $\boldsymbol{S}_i$ and $\boldsymbol{S}_j$. If J_{ij} is positive, the two spins will align parallel. In the case of the H_2 molecule, J_{ij} is negative and an antiparallel alignment of the two spins is favored. Because J_{ij} will take measurable values only when the electronic wavefunctions are overlapping, the exchange interaction is intrinsically short ranged and affects only nearest neighbor atoms.

Morrish [4] gives an interesting qualitative analysis of the value of J_{ij} as a function of the distance between the two nuclei. As depicted in Fig. 2.1, J_{ij} takes positive values (ferromagnetic coupling) for large interatomic distances compared to the extent of the electron wavefunction. These conditions are in fact usually met for open d and f electron shells, like the $3d$ shell of Fe. Because of the short range of the exchange interaction, a Hamiltonian of the form of equation (2.2) can sometimes be used to describe system of many spins where a sum of all individual nearest neighbor spin interaction is calculated. This is particularly useful to perform numerical calculation of the magnetic ground state of such systems. A system obeying this simple Heisenberg Hamiltonian is usually referred to has a an

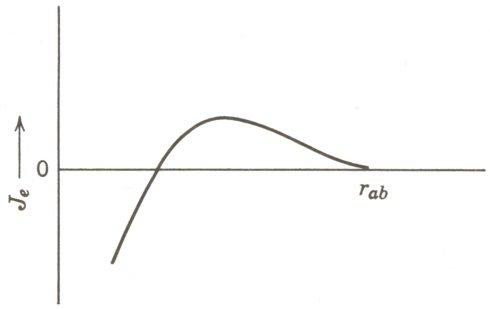

Figure 2.1: Qualitative evolution of the exchange integral J_{ij} as a function of the interatomic distance r_{ab}. Reproduced from [4].

Heisenberg spin system.

However, most of the ferromagnetic materials are conductive metals. The localized exchange interaction model presented above can obviously not be applied to itinerant electrons. Instead, a band model of the ferromagnetism has to be developed, which is briefly outlined hereafter.

In a metal at 0 K, all the electronic levels are filled up to the Fermi level. When an external magnetic field B is applied to a paramagnetic material, the band structure for spins parallel or antiparallel to the external field is modified. The parallel (antiparallel) band gains (looses) an energy equal to μB, where μ is the magnetic moment of the atoms. The band structure changes accordingly to keep the equilibrium of the Fermi level. The result is an excess of electrons aligned parallel to the external magnetic field. A net magnetization is observed.

For ferromagnetic materials, the exchange interaction can be represented as an effective field which polarizes the conduction electrons of the metal and creates a majority spin band. The itinerant electrons act on each individual atom to align their magnetic moment in a similar way as the localized exchange interaction would do. Above a certain temperature T_c (the Curie temperature), collective ferromagnetism breaks down because the gain in exchange energy becomes smaller than the thermal energy of the electrons. Above T_c, the material has a paramagnetic behavior, so that a net magnetization will appear only if an external magnetic field is applied.

2.2 Superexchange

It is often found that the transition metal monoxide compounds like FeO, CoO and NiO possess an antiferromagnetic ground state. In such material, the magnetic ions are separated by a diamagnetic anion and there is virtually no overlap of the $3d$ wavefunctions. As discussed in the previous section, this prevents direct exchange coupling between the magnetic ions.

Anderson [5] reported for the first time a model which accounts for the observed antiferromagnetic coupling in transition metal monoxides. He postulated the coexistence of two states for the metal-oxygen-metal system: The ionic state (no electron transfer) and the excited state where one electron from the p orbital of

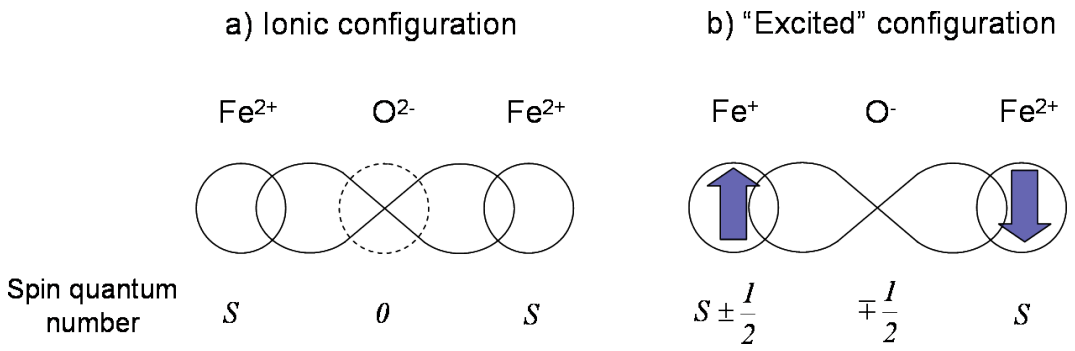

Figure 2.2: Schematic picture of Anderson's electron transfer model of superexchange for the FeO system. In the excited state, an electron transfer from the O $2p$ orbital to one of the $3d$ orbitals of Fe is achieved. This leads to an effective spin polarization of the O $2p$ orbital which is antiparallel to the excited $3d$ orbital.

the anion is transfered to a free d orbital of the magnetic ion, as shown on Fig. 2.2 for the case of FeO. The result is an effective spin polarization of the p orbital which is antiparallel to the d orbital. Because the p orbitals overlap the d wave functions of both magnetic ions, an effective antiferromagnetic coupling between the separated magnetic elements is achieved. The coupling depends crucially on the overlap between the different wavefunctions, and precise calculations of the superexchange effect need to take into account the shape and orientation of each orbital (for a recent review, see [6]). Superexchange therefore also depends on the local geometry in a crystalline material.

In a further development of the superexchange mechanism [7], Anderson demonstrated that superexchange can be efficiently described by a similar Hamiltonian as for the direct exchange case. The main difference is that the antiparallel spin configuration lowers the total energy of the system. Antiferromagnetic coupling is favored when the effective coupling constant J_{SE} is positive.

It should be noted that another condition for the occurrence of superexchange is that the material behaves as a "poor conductor", *i.e.* that the electrons remain localized around their original orbitals. This is in fact the case for the transition metal monoxides MnO, FeO, CoO and NiO. In these systems, superexchange leads to a long range antiferromagnetic coupling of magnetic ions mediated by the oxygen $2p$ orbital. The system is characterized by its Néel temperature T_N above which the antiferromagnetic order disappears.

2.3 Magnetic anisotropy

Ferromagnetic materials often exhibit an intrinsic *easy axis* of magnetization (along which spontaneous magnetization occurs) and a *hard axis* of magnetization (where an external field has to be applied to align the magnetization). This magnetic anisotropy is of great importance in thin films, both from technological and fun-

damental interest, as it allows the system to adopt a well defined magnetic state, even in the absence of an external field (remanence). The next paragraphs briefly review the most important contributions to magnetic anisotropy in thin films. A detailed overview of theoretical models as well as comparisons with experimental findings can be found in review articles [8, 9].

Microscopically, the two main sources of magnetic anisotropy arise from the dipolar interaction and the spin-orbit coupling. The long range character of the dipolar interaction results in a contribution which depends on the shape of the specimen and leads to a so-called *shape anisotropy* in thin films. In a ferromagnetic sample, the dipolar interaction can be described by an anisotropic demagnetizing field $\vec{H}_d = -\mathcal{N}\vec{M}$ where $\vec{M}$ is the magnetization vector and $\mathcal{N}$ the demagnetizing tensor. In a thin film, all tensor elements are zero except for the direction perpendicular to the plane: $\mathcal{N}_\perp = 1$.

Since the magnetostatic energy can be expressed as:

$$E_d = -\frac{\mu_0}{2V}\int_V \vec{M}\cdot\vec{H}_d\,dv \tag{2.3}$$

where μ_0 is the permeability of vacuum, it results in an anisotropy energy contribution per unit volume of a film:

$$E_d = \frac{1}{2}\mu_0 M_s^2 \cos^2\alpha \tag{2.4}$$

where M_s is the saturation magnetization and α the angle between the magnetization and the film normal. This results in a preferred in-plane alignment of the magnetization for thin films. As it is discussed below, other terms appear in the anistropy energy in the case of ultrathin films.

In a crystalline material and in the absence of spin-orbit interaction, the energy of the electrons is independent of the magnetization direction. In fact, the spin-orbit interaction couples the spin to the orbit of the electrons, which is itself coupled to the crystal lattice. This results in a total electron energy which depends on the relative orientation of the magnetization compared to the lattice. The *easy* and *hard* axis of magnetization in bulk materials therefore reflects the crystal symmetry. This is the *magneto-crystalline anisotropy* contribution.

The lowered symmetry at an interface strongly modifies this magneto-crystalline contribution, and leads to a so called *interface anisotropy*. In ultrathin films, the proportion of interface anisotropy can overcome the "bulk" magneto-crystalline anisotropy. This can induce for example a transition from parallel to perpendicular to the film plane easy axis of magnetization.

Another contribution is the *magneto-elastic anisotropy* which is due to stress or strain in the material. It can have important effect in the case of epitaxially grown multilayers, where a lattice mismatch can introduce large strain at the interface. In particular, strain can lead to a reorientation of the film magnetization near the interface.

In polycrystalline materials, there are usually no strong strain fields, and the magneto-elastic anisotropy is neligible. The magneto-crystalline anisotropy is averaged due to the random distributions of grain orientations. However, it can play a significant role in the case of textured samples (preferred orientation of the grains). A uniaxial anisotropy (due to any one of the above mentioned contributions) can usually be represented by a unidirectional anisotropy term in the total energy calculation of the system:

$$E_u = K_u \sin^2\varphi \tag{2.5}$$

where φ is the angle between the magnetization and the anisotropy axis. K_u is the anisotropy constant whose value accounts for the strength of the uniaxial anisotropy.

2.4 Interlayer coupling

The discovery of the superexchange mechanism more than 50 years ago demonstrated that magnetic interactions can propagate across non magnetic elements in poorly conducting oxides. In 1986, Grünberg *et al.* [10] reported for the first time the occurrence of antiferromagnetic (AFM) coupling of Fe layers separated by a thin Cr spacer layer. This discovery demonstrated that strong magnetic coupling can effectively occur over larger distances.

Bilinear-biquadratic coupling

The discovery of AFM coupling in Fe/Cr multilayer triggered an enormous interest for multilayers consisting of magnetic layers separated by non magnetic metallic spacers. Parkin *et al.* [12] later generalized the results to other metallic multilayer systems like Co/Ru and Co/Cr. They additionally observed an oscillatory behavior of the magnetic coupling (either ferromagnetic or antiferromagnetic) which depended on the spacer thickness.

The coupling energy density of such multilayer system is usually described by the following phenomenological equation:

$$E_B = -J_1 \cos\theta + J_2 \cos^2\theta \tag{2.6}$$

where θ is the angle between the magnetic moment of the adjacent magnetic layers. J_1 is the bilinear coupling constant which relates to pure ferromagnetic ($J_1 > 0$) or antiferromagnetic ($J_1 < 0$) coupling. As shown on Fig. 2.3a, its magnitude oscillates from positive to negative values depending on the spacer layer thickness and results in a corresponding oscillation of the effective coupling, as depicted on Figs. 2.3b and c. J_2 is the biquadratic coupling constant which was introduced to account for the orthogonal (90°) arrangement of adjacent magnetic layers observed in some systems [11].

Numerous models have been used to describe the observed coupling behavior (reviews on this topic can be found in reference [14, 15, 16]). The usual theory

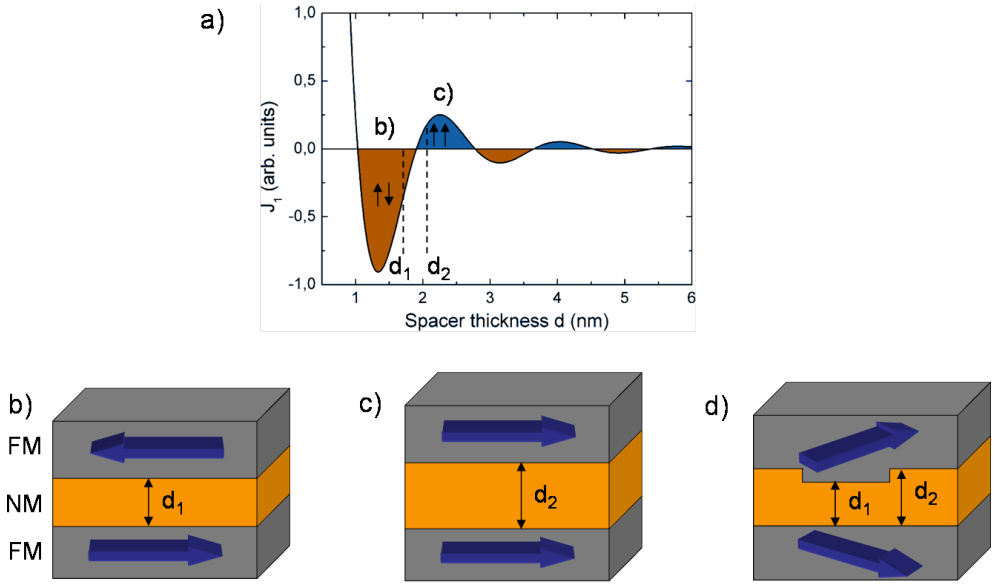

Figure 2.3: a) Spacer thickness dependence of the bilinear coupling constant J_1 according to the RKKY model. b) $J_1 < 0$: Antiferromagnetic coupling is favored. c) $J_1 > 0$: Ferromagnetic coupling is favored. d) In the case that J_1 is closed to zero, the short period oscillation of the bilinear coupling coupled with the roughness of the interfaces leads to measurable value of J_2 and orthogonal coupling is favored.

is very similar to the Ruderman-Kittel-Kasuya-Yosida (RKKY) indirect exchange interaction. According to this model, the long range magnetic coupling arises from the polarization of the conduction electrons in the spacer layer due to the direct contact with the localized spins of the magnetic layer. The oscillations of J_1 with the spacer thickness is due to the creation of polarized electron standing waves in the spacer layer for certain thicknesses. However, the oscillation periods derived from the RKKY model are usually much smaller than what is observed experimentally. In fact, while the RKKY oscillation period is valid for a continuum spacer, the discreteness of the atomic steps leads to an effective oscillation period which is larger than in the continuum case. This phenomenon was described as a kind of aliasing effect [17]. The model accounts for the observed oscillation period of J_1, which is found to be around 1 nm for most metallic systems.

Additionally to that long period oscillation, a short period (around 2 atomic layer) oscillation is also present. Its effect is usually small or statistically canceled out due to the roughness of the interfaces. However, studies have shown [11, 18] that when J_1 is small, the spin frustration induced by the lateral variation of the fast oscillating bilinear coupling can favor the orthogonal arrangement of the adjacent magnetic moments, as depicted in Fig. 2.3d, and leads to measurable value of J_2.

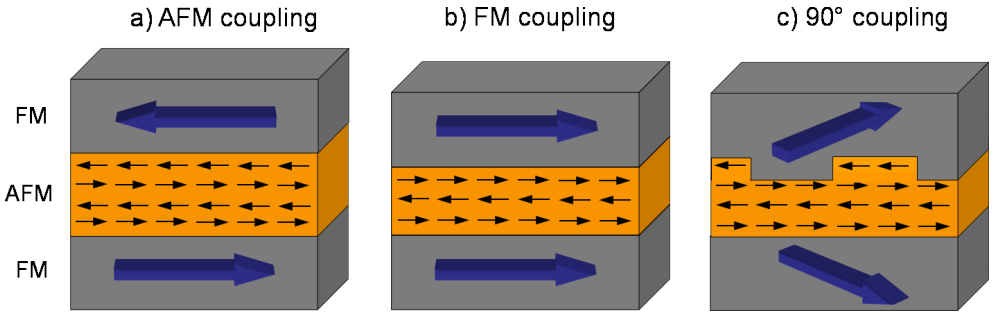

Figure 2.4: Schematic view of the magnetic coupling of two ferromagnetic layers separated by an antiferromagnetic spacer. a) and b) In the case of an even (odd) number of atomic planes in the AFM, an antiparallel (parallel) alignment is favored. c) In a real system with roughness, statistical variations of the AFM spacer thickness leads to an orthogonal arrangement of the magnetic moment of adjacent FM layers.

Proximity magnetism

The RKKY model describes the interlayer magnetic coupling of metallic multilayers. This mechanism relies on the interaction of localized spins with itinerant electrons and therefore requires a non-magnetic conductive spacer layer. However, many magnetic multilayer systems have a spacer layer which can possess some magnetic order (Mn,Cr) or even be completely antiferromagnetically ordered and poorly conducting (like a transition metal monoxide spacer). In the case that the spacer layer is antiferromagnetically ordered, a completely different coupling mechanism takes place. To describe such systems, Slonzcewski [16] developed the proximity magnetism model, which describes the case of ferromagnetic layers separated by an antiferromagnetic spacer layer. In contrast to the RKKY interaction, it is a direct coupling mechanism which is mediated by exchange coupling at the FM/AFM interfaces. The magnetic coupling is transmitted from one FM to the next through the AFM with the condition that direct exchange (ferromagnetic) coupling is achieved at both interfaces. For perfectly flat interfaces, this would lead either to ferromagnetic or antiferromagnetic coupling, depending on the number of AFM planes between the ferromagnets, as shown on Figs. 2.4a and b. Real systems usually exhibit some roughness at the interfaces which leads to statistical variation of the AFM spacer thickness. The induced spin frustration leads to the stabilization of a 90° coupling angle, as depicted on Fig. 2.4c.

It is interesting to note the similarity between Figs. 2.3d and 2.4c. In both cases, a 90° coupling in remanence occurs due to statistical interface roughness. However the coupling is mediated by a completely different mechanism. It is the result of lateral variation of the indirect RKKY interlayer coupling in the first case while it is due to interface coupling between two magnetic materials in the second case. As it will be shown later, this results in a different response of the coupled spin system to an external magnetic field.

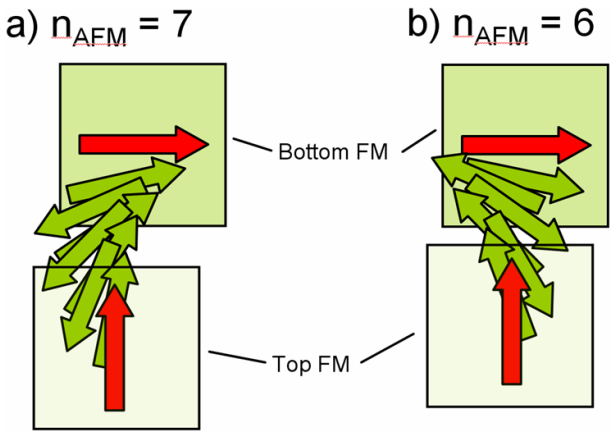

Figure 2.5: Two examples of possible twist structures in the AFM spacer layer when the magnetic moments of the surrounding metal layers are constrained to be orthogonal. Depending on the number of AFM atomic planes (odd or even), the rotation will occur clockwise or counterclockwise.

The phenomenological equation of the coupling energy density in the case of proximity magnetism can be written as:

$$E_P = C_+\theta^2 + C_-(\theta - \pi)^2 \tag{2.7}$$

where θ is the angle between adjacent magnetic layers. C_+ and C_- are the coupling constants associated with ferromagnetic or antiferromagnetic coupling, respectively. It is easily seen that in the case of statistical variations of the layer thickness (leading to an equal proportion of even and odd number of AFM planes), C_+ and C_- are equal and the coupling angle is 90°. In **paper IV** I derive an expression for the energy minimum of such coupled systems. It is worth noting that the coupling angle in remanence is determined only by the ratio of the two coupling constants:

$$\frac{C_+}{C_-} = \frac{\pi - \theta}{\theta} \qquad i.e. \qquad \theta = \frac{\pi}{1 + \frac{C_+}{C_-}} \tag{2.8}$$

The orthogonal arrangement of the FM magnetic moments results in a twist in the AFM with different chirality for the even and odd number of AFM planes. This effect is discussed in **paper IV** and illustrated here in Fig. 2.5. In the original paper from Slonzcewski, it is assumed that the interfacial coupling between the ferromagnet and the antiferromagnet is large and no anisotropy is assumed for the AFM. Xi *et al.* [19] proposed an extended version of the proximity magnetism model which takes into account the finite value of the interfacial exchange coupling and the AFM thickness. One of the results is that compared to Fig. 2.5, the AFM twist is also allowed to have different rotation angle between each AFM planes. An effect which can be of importance when the thickness of the AFM becomes larger.

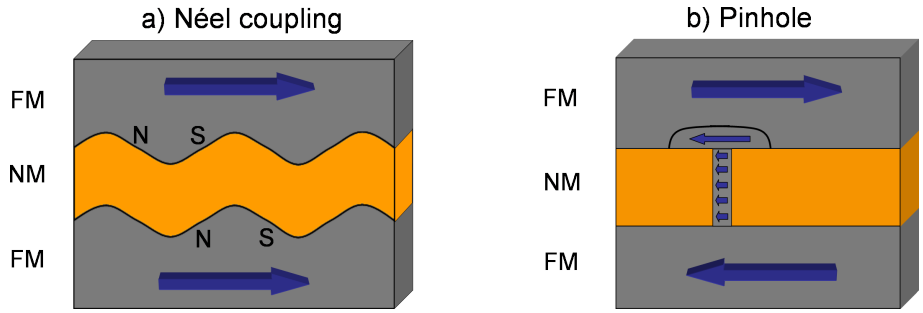

Figure 2.6: Schematic representation of possible coupling arising between two ferromagnetic (FM) layers separated by a non magnetic (NM) spacer. a) Néel (orange peel) dipolar coupling due to the correlated roughness of the layer stack. Magnetic dipoles appear within the FM layers due to the waviness of the interface. These dipoles can couple to local dipoles in the second FM layer through dipolar interaction, which favors FM coupling. b) Pinhole coupling induced by a ferromagnetic bridge in the spacer layer.

Other coupling mechanisms

While the two above mentioned coupling terms are usually dominant, several other mechanisms can influence the observed coupling properties.

Néel [20] introduced for the first time the possibility of direct dipolar magnetic interactions between two infinite ferromagnetic layers separated by a non magnetic spacer. According to this model, local dipoles are created at the interfaces due to roughness. In the case of correlated roughness between the two interfaces, a long range dipolar interaction can appear which favors a parallel alignment of the two ferromagnetic layers, as depicted in Fig. 2.6a. Because this type of coupling is due to the "waviness" of the interfaces, it is often referred to as *orange peel* coupling. The above conclusions were recently generalized to finite layer thickness, with practical applications to spin valve systems [21]. The energy associated with this dipolar interaction is usually small compared to the other type of interlayer coupling and is mainly used as a minor correction to the observed magnetic behavior of a multilayer system.

Another source of perturbation arises from what is called ferromagnetic pinholes. Due to the intrinsically small thickness of the spacer layer (usually around one nm), defects or inhomogeneities in the spacer can lead to a discontinuity of the layer. In that case, it is possible to form a ferromagnetic bridge between the two magnetic layers which can influence greatly the overall interlayer coupling, as depicted in Fig. 2.6b. Fulghum *et al.* [22] have shown that the area influenced by a ferromagnetic pinhole can be as large as 100 times the area of the pinhole itself. This effect can therefore become critical in the case of sub-nanometer thick spacer layers.

Because these effects both favor ferromagnetic coupling, they are usually considered as parasitic effects in antiferromagnetically coupled multilayers.

2.5 Total energy calculation

One of the most important property of a magnetic multilayer is its response to an externally applied magnetic field, which is usually characterized by its hysteresis (or magnetization) curve.

The determination of magnetic spin structure of a multilayer is usually carried out by calculating the minimum of the total energy of the system. For that purpose, the magnetic multilayer is subdivided in N layers. The system is then considered as a one dimensional spin chain and each layer is represented by its macroscopic magnetic moment[23]. One has to sum all the magnetic contributions to the total energy of the system and find the spin configuration which minimizes this energy in a given external magnetic field. In the case of thin layers constrained to an in-plane magnetization, it is usually done by finding the minimum of the derivative $\partial E/\partial\theta_i$ where θ_i is the angle of the magnetization in each layer, relative to the external field.

Summarizing the results of the previous sections, one can write the total energy of a polycrystalline multilayer system consisting of N ferromagnetic layers (separated by spacer layers) of thickness d, in the case of uniaxial in-plane anisotropy K_i and bilinear-biquadratic interlayer coupling J_1 and J_2 respectively:

$$E_N = \vec{H}\cdot\sum_{i=1}^{N}\vec{m_i}d + \frac{1}{2}\sum_{i=1}^{N}K_i(\vec{m_i}\cdot\vec{n})d - J_1\sum_{i=1}^{N-1}\vec{m_i}\cdot\vec{m_{i+1}} + J_2\sum_{i=1}^{N-1}(\vec{m_i}\cdot\vec{m_{i+1}})^2 \quad (2.9)$$

$\vec{m_i}$ are the magnetization vectors of each layer, $\vec{n}$ is a unit vector pointing in the direction of the easy axis and $\vec{H}$ the externally applied magnetic field. The first term of the equation is called the Zeeman energy term and accounts for the influence of the external magnetic field on the system. The second terms describes the influence of the uniaxial anisotropy and the last two terms describe the bilinear and biquadratic interlayer coupling. For each field value, the spin configuration is determined numerically by finding the energy minimum of the spin system. This type of procedure can be used for example to reproduce experimental magnetization curves. In particular, a fit of a magnetization curve using the above equation will not only yield the evolution of the spin configuration, but can also be used to extract the values of anisotropy or coupling constants [24].

In the following paragraph, the formalism is applied to the example of a trilayer system (two ferromagnets separated by one spacer layer). This is used to compare the evolution of the spin configuration if the system is coupled either through a biquadratic interaction or a proximity magnetism interaction (the case of an AFM spacer). The layers are assumed to possess a uniaxial anisotropy. The total energy of the coupled spins for the biquadratic interaction can be written as:

$$E_{2B} = \vec{H}\cdot(\vec{m_1}+\vec{m_2})d + \frac{1}{2}K_u(\sin^2\theta_1 + \sin^2\theta_2)d + J_2(\vec{m_1}\cdot\vec{m_2})^2 \quad (2.10)$$

where θ_1 and θ_2 are the angles of the first and second layer magnetization

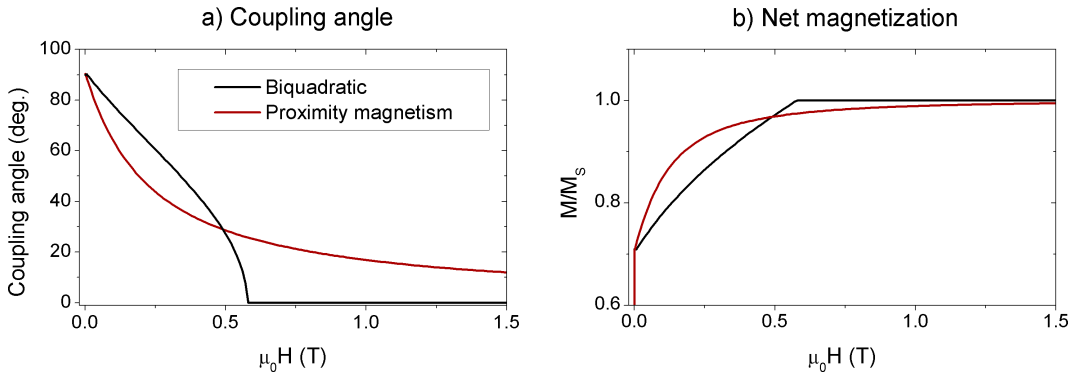

Figure 2.7: Simulated evolution of a trilayer spin structure in an external field for biquadratic coupling and proximity magnetism coupling. a) Evolution of the coupling angle. b) Evolution of the net magnetization parallel to the external field. The curves show distinctive behavior for the two types of coupling.

orientation relative to the uniaxial anisotropy. A similar equation can be written for the case of proximity magnetism:

$$E_{2P} = \vec{H} \cdot (\vec{m_1} + \vec{m_2})d + \frac{1}{2}K_u(\sin^2\theta_1 + \sin^2\theta_2)d + C_+\theta^2 + C_-(\theta - \pi)^2 \qquad (2.11)$$

where θ is the angle between the two adjacent ferromagnetic layers.

In order to understand how the different coupling mechanisms influence the magnetic structure of the system in an external field, the total energy of the spin system is calculated using equations (2.10) and (2.11). The simulated system is composed of two 2 nm thick Fe layers separated by a spacer. The external field is applied perpendicular to the axis of the uniaxial anisotropy. C_+ and C_- are chosen to be equal (to induce a 90° coupling in remanence) with a value $C_+ = C_- = 0.1\,\mathrm{erg/cm^2}$. These values are typical from what is observed experimentally [25]. The biquadratic coupling constant is chosen to $J_2 = 0.5\,\mathrm{erg/cm^2}$, a value which leads to comparable field dependence as for the proximity magnetism model (C_+ and C_- being fixed to experimentally measured values). The coupling angle and the net magnetization as a function of the external magnetic field are determined by finding the energy minimum for each field value.

The results are plotted on Fig. 2.7 where clear differences are seen between the two coupling mechanisms. For the biquadratic coupling, a "cut off" appears at relatively low fields (the value of which depends on the coupling strength) where the moments align parallel to the external field. Proximity magnetism leads to an asymptotic decrease of the canting angle, which would theoretically vanish only at infinitely high fields. The remanent coupling angle is fixed by the ratio of C_+ and C_-. The absolute values of these constants are determined by the strength of the interface exchange coupling between the ferromagnet and the antiferromagnet. Higher values will lead to higher coupling angle in high field. Measuring the evo-

lution of the coupling angle as a function of the external field can therefore yield useful information regarding the interfacial interactions.

The evolution of the net magnetization along the magnetic field axis is plotted in Fig. 2.7. The two curves exhibit different shapes upon reaching saturation. This can therefore be used to distinguish between the two types of coupling via simple magnetometry experiments.

Chapter 3

Experimental techniques

In the present work, grazing incidence nuclear resonant scattering (GI-NRS) and polarized neutron reflectometry (PNR) were combined to resolve the magnetic structure of Fe/Fe-oxide multilayers in a layer specific manner. Because of their isotopic sensitivity, these two techniques are well suited to study systems where the same magnetic element is present in both types of layers. As it is shown in **Paper IV**, the two methods complement themselves ideally in this case, when isotopic probe layers are placed at selected positions in the layer structure.

In this chapter, the scattering formalism of grazing incidence nuclear resonant and neutron scattering is outlined, emphasizing their common basis. Later on, the specificity of both techniques to probe the structure of magnetic multilayers is described, giving the reader the opportunity to better appreciate how these two techniques can be combined to resolve the complex magnetic structure of Fe/Fe-oxide multilayers. The last section of this chapter gives a brief introduction on hard x-ray absorption spectroscopy. This technique is a powerful element specific probe of the chemistry and local order of atoms in matter. It played a central part in this study, enabling to resolve *in-situ* the chemistry of the buried oxide layer that appears in our system.

3.1 Propagation of x-rays in matter

This section summarizes the theoretical description of grazing incidence reflectivity from a multilayered medium. It is meant to give the basic formalism common to x-ray reflectivity, nuclear resonant reflectivity and neutron reflectivity. The theory will therefore be derived for the general scattering case before the particular scattering amplitude, specific to each methods, is discussed.

Forward scattering

In the special case of forward scattering of x-rays (or neutrons), the optical properties of solid do not depend on the microscopic arrangement of the scatterers, but are uniquely determined by the properties of the constituting atoms. In the case

that the internal state of the scattering system is not modified during the scattering process, the discrete ensemble of scatterers can be approximated by a continuous medium having an effective index of refraction $\boldsymbol{n}$:

$$\boldsymbol{n} = 1 + \frac{2\pi}{k_0^2} \sum_i \rho_i \boldsymbol{M_i} \tag{3.1}$$

where k_0 is the wavenumber of the radiation. $\boldsymbol{M}_i$ is the coherent forward scattering length of the ith atom of number density ρ_i. The sum runs over all atoms in the scattering volume. The amplitude in depth z of a slab of material is given by the expression:

$$A(z) = e^{ik_0 n z} A_0 \tag{3.2}$$

In this formula, n is a scalar. It can be extended to take into account the case of anisotropic medium where the index of refraction is dependent on the polarization state of the light. In this case $\boldsymbol{n}$ (and $\boldsymbol{M_i}$) becomes a 2×2 matrix. It should be noted that the specificity related to each type of scattering process (x-ray, neutron,...) involved is all contained in the $\boldsymbol{M}_i$. The particular form of $\boldsymbol{M}$ for NFS or PNR will be developed in a later section of this chapter.

Grazing incidence scattering of x-rays and neutrons can be treated in the forward scattering approximation but has to be treated as a two-beam case of x-ray diffraction. The basic formalism is described in the following subsection and further applied to x-ray (electronic and nuclear) as well as neutron scattering.

Reflection from stratified media

The dynamical theory of x-ray scattering is used to calculate the field amplitudes in all open scattering channels of a given scattering geometry. In the case of a homogeneous medium, the wave field amplitude in all the open scattering channels can be described by an equation having a similar form as equation (3.2):

$$\boldsymbol{A}(z) = e^{i\boldsymbol{F}z} \boldsymbol{A}(0) \tag{3.3}$$

where $\boldsymbol{F}$ is the propagation matrix. The dimensions of $\boldsymbol{F}$ and $\boldsymbol{A}(z)$ are determined by the number of available scattering channels. For example in the case of forward scattering only one channel is open (forward transmitted). It is interesting to note that equation (3.3) has a similar form as equation (3.2). For that reason, x-ray reflection can be treated in the forward scattering approximation with the propagation matrix $\boldsymbol{F}$ replacing the index of refraction $\boldsymbol{n}$.

This formalism can be applied to the case of grazing incidence reflection from a stratified medium. In that case there are two scattering channels open at each boundary: the forward transmitted (A_+) and the specular reflected (A_-) channels, as depicted in Fig. 3.1. $\boldsymbol{F}$ will therefore be a 4×4 matrix (to take into account the different polarization state). In a single layer i, the field amplitude $\boldsymbol{A}(z)$ at depth

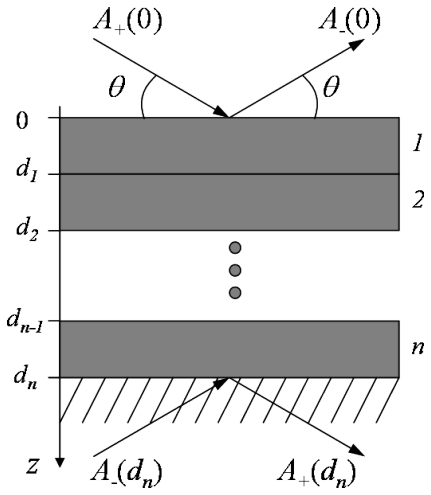

Figure 3.1: Scattering geometry and field amplitudes for the case of grazing incidence reflection from a n layer medium.

z is related to the field amplitude at the surface $\boldsymbol{A}(0)$ by:

$$\boldsymbol{A}(z) = e^{i\boldsymbol{F_i}z}\boldsymbol{A}(0) = \boldsymbol{L_i}(z)\boldsymbol{A}(0) \tag{3.4}$$

where the matrix exponential defines the 4×4 layer matrix $\boldsymbol{L_i}(z)$ of layer i. The propagation matrix $\boldsymbol{F}$ takes the form:

$$\boldsymbol{F} = \begin{pmatrix} \boldsymbol{f} + \boldsymbol{k_{0z}} & \boldsymbol{f} \\ -\boldsymbol{f} & -\boldsymbol{f} - \boldsymbol{k_{0z}} \end{pmatrix} \tag{3.5}$$

and $\boldsymbol{f}$ is given by:

$$\boldsymbol{f} = \frac{2\pi}{k_{0z}} \sum_i \rho_i \boldsymbol{M_i} \tag{3.6}$$

where $\boldsymbol{k_{0z}}$ is the unity matrix multiplied by k_{0z}, the component of the incident wave vector perpendicular to the surface. $\boldsymbol{f}$ is the 2×2 forward scattering matrix. In the case of a multilayer of n layers, the field amplitude in depth z of the sample (located in the ith layer) is given by the product of the corresponding layer matrices:

$$\boldsymbol{A}(z) = \boldsymbol{L_i}(z - d_{i-1})...\boldsymbol{L_2}(d_2)\boldsymbol{L_1}(d_1)\boldsymbol{A}(0) \tag{3.7}$$

In the case of grazing incidence reflection, this equation can be solved analytically. It is convenient to write the solution of this problem in the system of eigenpolarizations of the sample. In this case the 4×4 scattering ($\boldsymbol{F}$) and propagation ($\boldsymbol{L}$) matrices can each be decomposed into two 2×2 matrices. In the following, the expression for the layer matrix $\boldsymbol{L_1}$ is given for one eigenpolarization state:

$$\boldsymbol{L_1}(z) = e^{i\boldsymbol{F}z} = \frac{1}{t_{01}} \begin{pmatrix} 1 & r_{01} \\ r_{01} & 1 \end{pmatrix} \begin{pmatrix} e^{ik_{1z}z} & 0 \\ 0 & e^{-ik_{1z}z} \end{pmatrix} \begin{pmatrix} 1 & r_{10} \\ r_{10} & 1 \end{pmatrix} \frac{1}{t_{10}} \tag{3.8}$$

where k_{1z} is the z-component of the wavevector in the layer, which is related to

the z-component of the incident wavector by :

$$k_{1z} = k_{0z}\beta_1 \quad \text{with} \quad \beta_1 = \sqrt{1 + \frac{2f_1}{k_{0z}}} \tag{3.9}$$

The r_{ij} and t_{ij} are the Fresnel reflection and transmission coefficients of the boundary between layer i and j respectively:

$$r_{ij} = \frac{\beta_i - \beta_j}{\beta_i + \beta_j} \quad \text{and} \quad t_{ij} = \frac{2\beta_i}{\beta_i + \beta_j} \tag{3.10}$$

Using these expressions for the layer matrix and applying proper boundary conditions, one can calculate the reflected intensity from a multilayer structure using equation (3.7). The equation can then be solved for each value of k_{0z} (*i.e* for each incident angle) to calculate a full reflectivity curve.

So far, no assumption has been made regarding the nature of the incident radiation and its interaction with matter. The formalism is therefore valid for grazing incidence x-ray and neutron scattering. In the following section, the peculiarity of the scattering process involved in x-ray reflectivity, grazing incidence nuclear resonant scattering and polarized neutron reflectometry are discussed. All these particular effects will be described by the energy and polarization dependent coherent scattering length $\boldsymbol{M}$.

3.2 Electronic x-ray reflectivity

Conventional x-ray reflectivity relies on interactions of the incoming photon with the electrons of the material. The electronic scattering length $E(\omega)$ is given by:

$$[E(\omega)]_{\mu\nu} = (\vec{\epsilon_\mu} \cdot \vec{\epsilon_\nu}) \left[-Zr_0 + i\frac{k_0}{4\pi}\sigma_t(\omega) \right] \tag{3.11}$$

where $\vec{\epsilon_\mu}$ and $\vec{\epsilon_\nu}$ are the basis vector of the polarization basis used to describe the scattering process. Z is the atomic number of the material, r_0 the classical electron radius and $\sigma_t(\omega)$ the total absorption cross section.

Away from elemental absorption edges, the electronic scattering length $E(\omega)$ increases linearly with the atomic number of the scattering material. This leads to a material dependent propagation of the x-ray in matter. Near the absorption edge however, the scattering length is modified and corrections have to be made to the above formula (Höln corrections) [26]. For that reason, x-ray reflectivity experiments are usually carried out at energies which are far from any absorption edges of the element present in the investigated system. In a grazing incidence reflectivity experiment, the reflected intensity as a function of the incidence angle will depend on the thickness, density, and atomic number of the reflecting layers. The technique can therefore provide contrast between layers of different density or composition.

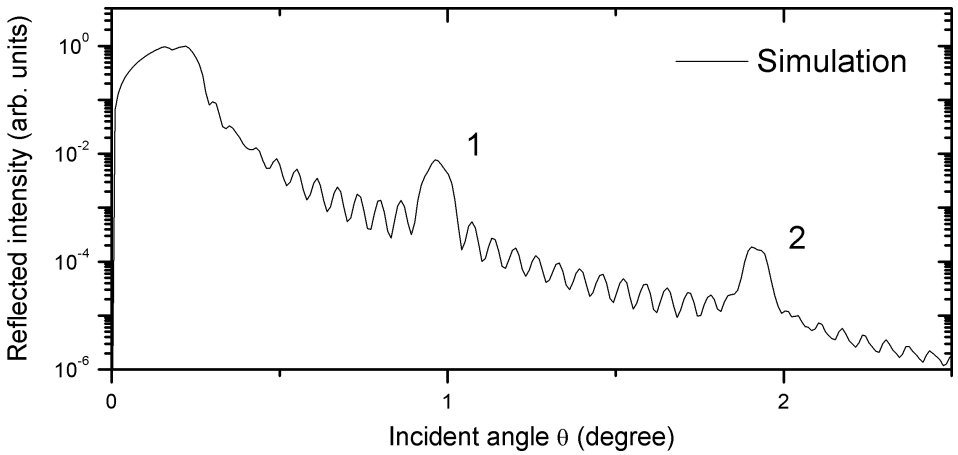

Figure 3.2: Simulated x-ray reflectivity curve of a Si/[Fe(2 nm)/FeO(1 nm)]$_{15}$/Al superlattice. Bragg peak appears at positions given by Bragg's law $n\lambda = 2d\sin\theta$, where d is the period of the superlattice. The incident x-ray has a wavelength of 1Å which is equivalent to an energy of 12.4 keV.

In a x-ray reflectivity experiment, the intensity of the specularly reflected x-ray beam is measured as a function of the incident angle. In the case of a periodic multilayer structure (superlattice), this leads to the appearance of Bragg peaks at angles defined by Bragg's law:

$$2d\sin\theta = n\lambda \tag{3.12}$$

where d is the period of the multilayer structure normal to the surface plane. For example, in the case of $d = 3$ nm and $\lambda = 1$ Å, the position of the first order Bragg reflection would be at $\theta = 0.95°$, which is in the grazing incidence reflection regime. The simulated reflectivity curve of a Si/[Fe(2 nm)/FeO(1 nm)]$_{15}$/Al is displayed on Fig. 3.2. The first Bragg peak appears at the position calculated above. The fast oscillating wiggles are the Kiessig fringes that result from interference between amplitudes reflected at the surface and the substrate. Their period decreases with an increasing total thickness of the multilayer.

As mentioned earlier, the reflectivity curve can be calculated using equation (3.7). The main parameters being the layer thicknesses, density of each materials and roughnesses. The influence of the later parameter is not discussed in this work but the reader is referred to textbooks on the subject [26, 27]. If one use a fitting procedure to match the calculated reflectivity to measured data, very precise determination (<0.1 nm) of layer thickness, density and roughness of thin films is possible. The reflectivity curve presented in this work were fitted using the LSFIT program coded by O. Seeck (DESY, Hamburg).

3.3 Nuclear resonant scattering

In this section the focus will be on *nuclear* dipole transitions and in particular on the resonant scattering from the 14.4 keV resonance of ^{57}Fe, which will be used in the present work. Because it is a resonant process, the scattering cross section is highly energy dependent. As will be described later, the resonance width of such interaction is extremely narrow and requires a very high spectral flux of incident radiation to obtain a sufficiently high signal.

The 4.7 neV energy width of the nuclear level corresponds to a comparatively long lifetime of 141 ns for the excited state, which is indeed very long compared to normal charge scattering (in the fs regime). When the resonance is excited by a flash-like synchrotron pulse, proper time gating of the signal using avalanche photodiode detectors [29] and fast electronics allows one to discriminate the nuclear resonant signal from the non-resonant charge scattering. This provides then a virtually background free signal. As will be described later, the long lifetime of the nuclear level allows to carry out time resolved studies of the nuclear de-excitation, giving access to the hyperfine interaction parameters of the atom.

One of the particularities of NRS comes from its unique isotope sensitivity, which renders possible the use of isotopic tracer layers to selectively probe parts of the sample. The method itself is sensitive to the hyperfine structure of the nuclear levels, giving access not only to the magnetic configuration but also to the electronic environment of the atom. In the past decades , the technique developed and is nowadays widely used for investigations in various fields of science such as magnetic structure of thin films [27, 28], diffusion processes [30], relaxation dynamics in liquids [31] and vibrational dynamics [32]. In the following section, the discussion is restricted to coherent elastic scattering on magnetic thin films in grazing incidence geometry. An extensive overview of the possibilities of the technique is available in [27].

The nuclear scattering amplitude

The ^{57}Fe nuclear resonance is a magnetic dipole transition with spins $I_g = 1/2$, $I_e = 3/2$, magnetic moments $\mu_g = 0.091\mu_N$, $\mu_e = -0.153\mu_N$ of the ground and excited state respectively, and a natural lifetime $\tau_0 = 141\,\text{ns}$. μ_N is the nuclear magneton and is defined as $\mu_N = \frac{e\hbar}{2m_P}$, where m_P is the proton mass. In the case that the material is magnetic (*e.g.* the $3d$ band is polarized, and hence polarizes the $4s$ electrons), a magnetic field appears at the position of the nucleus that leads to hyperfine interactions between the s electrons and the nucleus. The generated magnetic field is often very large and is referred to as the magnetic hyperfine field B_{hf}, which amounts to 33.3 T for bulk α-Fe. In this magnetic field, the degeneracy is lifted, resulting in a Zeeman splitting of the nuclear levels. The dipole selection rule $\Delta M = m_e - m_g = 0, \pm 1$ leads to six energetically separated resonances, as shown in Fig. 3.3. In the case of a pure magnetic hyperfine interaction, the energetic

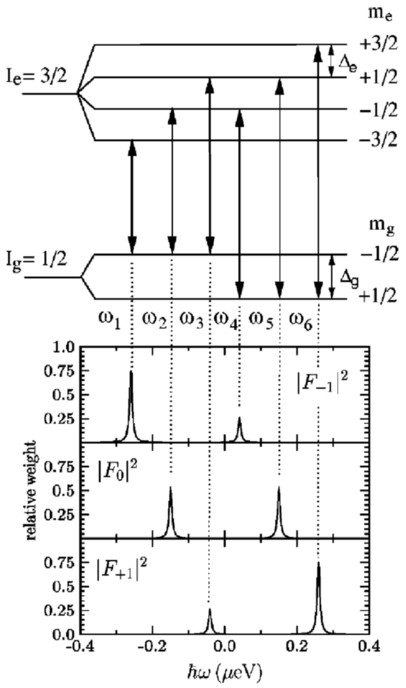

Figure 3.3: Nuclear level of the 14.4 keV resonance of ^{57}Fe under the influence of a 33.3 T hyperfine field. The splitting of the nuclear level leads to 6 allowed transitions, each separated by a few hundreds of neV. The bottom panel show the corresponding energy dependence of the resonant strength F_M with a change of M in the magnetic quantum number.

positions of the resonance lines are given by:

$$E = E_0 - \left(\mu_e \frac{m_e}{I_e} - \mu_g \frac{m_g}{I_g}\right) B \tag{3.13}$$

where m_g and m_e are the magnetic quantum numbers of the ground and excited states, respectively.

The coherent scattering length $\boldsymbol{M}$ for the case of an electric dipole transition can be written as:

$$\begin{aligned}[\boldsymbol{M}(\omega)]_{\mu\nu} = \frac{3}{16\pi}\{&(\vec{\epsilon_\mu}\cdot\vec{\epsilon_\nu})[F_{+1}+F_{-1}] \\ &- i(\vec{\epsilon_\mu}\times\vec{\epsilon_\nu}).\vec{m}[F_{+1}-F_{-1}] \\ &+ (\vec{\epsilon_\mu}\cdot\vec{m})((\vec{\epsilon_\nu}\cdot\vec{m})[2F_0-F_{+1}-F_{-1}]\}\end{aligned} \tag{3.14}$$

where the F_M are the energy dependent resonant strengths for transitions with a change of ΔM in the magnetic quantum number. They are plotted in Fig. 3.3 for the case of bulk α-^{57}Fe. In the case of a magnetic dipole transition (like the ^{57}Fe resonance), the role of the electric and magnetic fields are interchanged compared to an electric dipole resonance. The polarization vectors are then changed from $\vec{\epsilon}$ to $\vec{\epsilon}\times\vec{k_0}$, where $\vec{k_0}$ is a unit vector along the photon wavevector.

The three terms of equation (3.14) essentially contain all the polarization dependence of the scattering process. The first term is not sensitive to the sample magnetization and has the same polarization dependence as normal charge scattering. The second term describes circular dichroism and involves an orthogonal

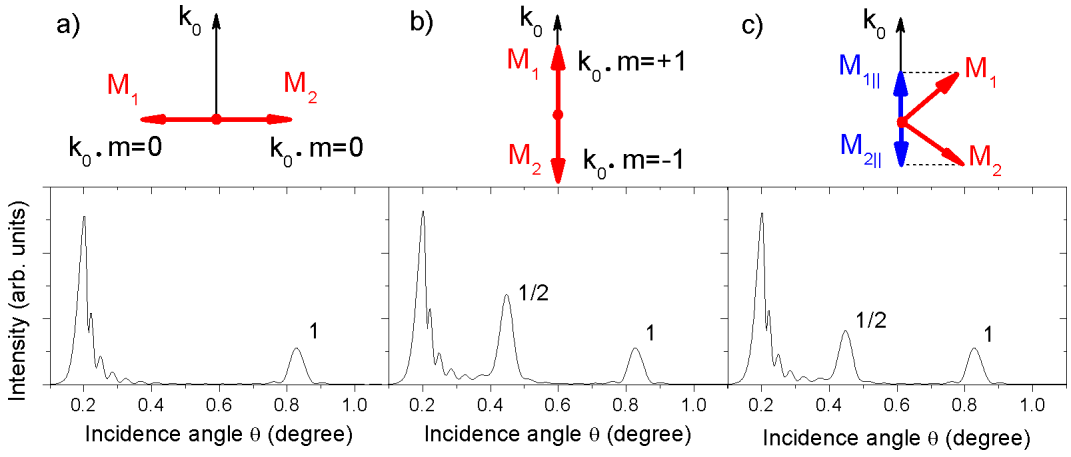

Figure 3.4: Simulated nuclear reflectivity curve of a magnetically coupled Si/[Fe(2 nm)/FeO(1.1 nm)]$_{15}$/Al superlattice. The intensity of the magnetic half-order Bragg peak depends on the relative orientation of the magnetizations M_1 and M_2 relative to $\vec{k_0}$.

changes of the photon polarization ($\sigma \rightarrow \pi$ and $\pi \rightarrow \sigma$). The third term describes linear dichroism and allows for all scattering processes within the given polarization basis. As can be seen, the second and third term of equation (3.14) are dependent on the orientation of the magnetization $\vec{m}$. This strong intermixing between light polarization and magnetization orientation leads to a dependence of the nuclear scattering amplitude on the orientation of the magnetic moment relative to the incoming photon wavevector.

In the case of a superlattice (a multilayer where a structural unit cell is repeated many times), this can lead to the appearance of purely magnetic reflections. For example, if adjacent ferromagnetic layers (separated by an arbitrary spacer) have magnetic moments aligned antiparallel, the magnetic unit cell is twice as large as the chemical unit cell. Following equation (3.12), this leads to the appearance of superstructure (half order) Bragg peaks which are due to the fact that the period of the nuclear scattering length in the depth of the sample follows the magnetic period. Therefore, the presence of half-order Bragg peaks in a nuclear reflectivity curve are direct signs of a magnetic superstructure within a superlattice.

Practically, the orientation of the magnetic moment relative to the photon wavevector can always be decomposed into two projections parallel ($\vec{k_0} \cdot \vec{m} = \pm 1$) or perpendicular ($\vec{k_0} \cdot \vec{m} = 0$) to $\vec{k_0}$. In the case of perpendicular alignment the nuclear scattering length does not change if the magnetic moments are rotated by 180°. This means the appearance of half order Bragg peaks in the nuclear reflectivity accounts only for the difference in the projection of the two magnetic moment along $\vec{k_0}$. The height of this peak is a quantitative measure of the difference in the projections along $\vec{k_0}$. Different situations are illustrated in Fig. 3.4 with three different orientation of the magnetic sublattices. To obtain a complete information on the magnetic moment orientation, it is usually necessary to record nuclear re-

flectivity curves at different azimuthal rotation of the sample with respect to the x-ray beam.

Time resolved nuclear resonant scattering

The previous section dealt with the polarization dependent nuclear scattering length amplitude, which is measured by time-integration of the delayed signal in a specific time window after pulsed excitation by synchrotron radiation. As mentioned earlier, this can be achieved by using APD detectors and fast electronics for prompt discrimination. However, NRS can also be used in a time resolved manner to study the time dependent de-excitation of the nucleus. In the case of a magnetic hyperfine interaction, the six allowed transitions possess all a slightly different energy and will all be excited at the same time. The coherent de-excitation of these transitions will lead to a beating of the nuclear intensity in time. The shape and frequency of this beating is a direct fingerprint of the configuration of the nuclear levels. Analysis of these so called *timespectra* enables to access the hyperfine parameters of the atom. This method can therefore be applied to probe the magnetic structure and chemical environment of thin layered films.

In the case of a thin layer of thickness d deposited on a semi-infinite substrate, the frequency dependent reflected intensity is given by [27]:

$$R(\omega) \approx r_{02} e^{i f_1(\omega) |t_{02}|^2 d} \tag{3.15}$$

The time response of the system is then obtained by Fourier transformation of $R(\omega)$:

$$R(t) \approx \delta(t) - \tilde{f}(t) \chi e^{-\chi t/2\tau_0} \tag{3.16}$$

with

$$\chi = \frac{1}{4} \rho \sigma_0 f_{LM} \mid t_{02} \mid^2 \frac{d}{\phi} \tag{3.17}$$

where $\tilde{f}(t)$ is the Fourier transform of $f(\omega)$. The δ function describes the instantaneous excitation pulse which passed through the sample. The envelope of the beating pattern is exponentially decaying in time due to the de-excitation of the nuclear level. $\tilde{f}(t)$ intrinsically contains the dependence of the temporal beat pattern on the transition involved. As described in the previous section, the transition probability of the nuclear levels depends on the orientation of the magnetization relative to the incoming photon wavevector. Different magnetic moment orientations lead to different shapes of the timespectra. Therefore, the shape of the timespectra can also be used to resolve magnetic moment orientations in the probed layer. This is exemplified in Fig. 3.5 for magnetizations parallel and perpendicular to $\vec{k_0}$. It should be noted that some spin configurations are degenerate in the timespectra. For that reason, it is necessary to record timespectra at different azimuthal angles (sample rotation). The sign of the magnetic moment can however not be distinguished in conventional experiments. To eventually tackle this problem, L'abbé *et al.* [35] have shown that it is possible to retrieve the sign of the moment by using

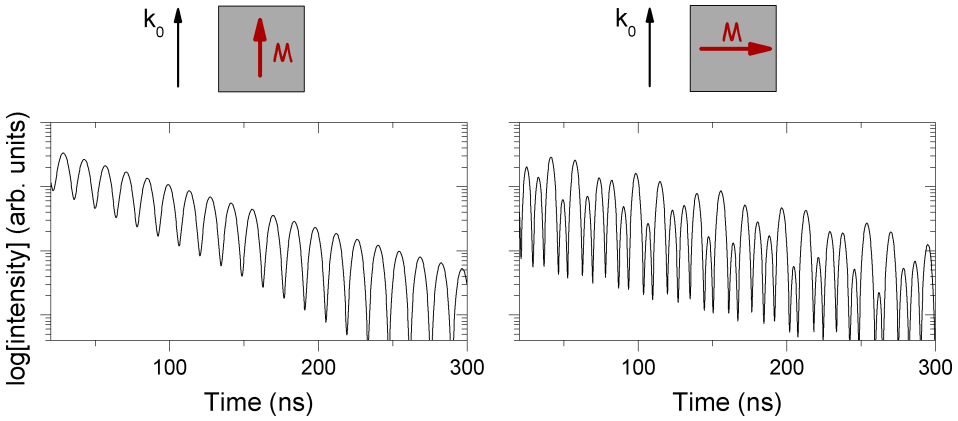

Figure 3.5: Simulated nuclear timespectra of a 50 nm Fe layer on Si. The shape of the timespectra highly depends on the orientation of the magnetization relative to $\vec{k_0}$.

circularly polarized light and a reference sample placed on a mossbauer drive.

The analysis of timespectra can be applied to study the magnetic structure of multilayers containing multiple ^{57}Fe layers. The signal is then a coherent sum of the signals produced by each layer, scaled by the field intensity at the position of the probe. For that reason, it is possible to obtain accurate depth resolved information from the time spectra by recording spectra at different incident angles, where the contributions of the different probe layers to the total signal is different. In particular, extreme surface sensitivity can be achieved by recording timespectra below the critical angle of the sample.

The timespectra and nuclear reflectivity curves simulated in this work were all calculated using the CONUSS program package [36], which performs simulations using the full dynamical theory of coherent nuclear resonant scattering.

Experimental setup

All the nuclear resonant scattering experiments presented in this work were carried out at the nuclear resonance beamline ID18 [37] of the European Synchrotron Radiation Facility (ESRF). The schematic layout of the beamline is sketched in Fig.3.6. Because NRS is a time resolved method requiring temporal spacing between the excitation pulses, the experiments were performed in special timing mode of the storage ring, namely the 16 bunch mode (176 ns bunch spacing, 90 mA beam current) and the 4 bunch mode (708 ns bunch spacing, 45 mA beam current). At ID18, the x-rays are produced by a set of three 1.6 m long undulators (two of them are undulators that have their first harmonic at 14.4 keV and are therefore optimized to deliver maximum flux at the ^{57}Fe resonance energy). A high heat load monochromator provides a first stage of monochromatization to 2 eV bandwidth using the Si(111) reflection. The bandwidth is then further reduced to ∼1 meV using a high resolution monochromator (HRM). Compound refractive lenses (CRLs) [39]

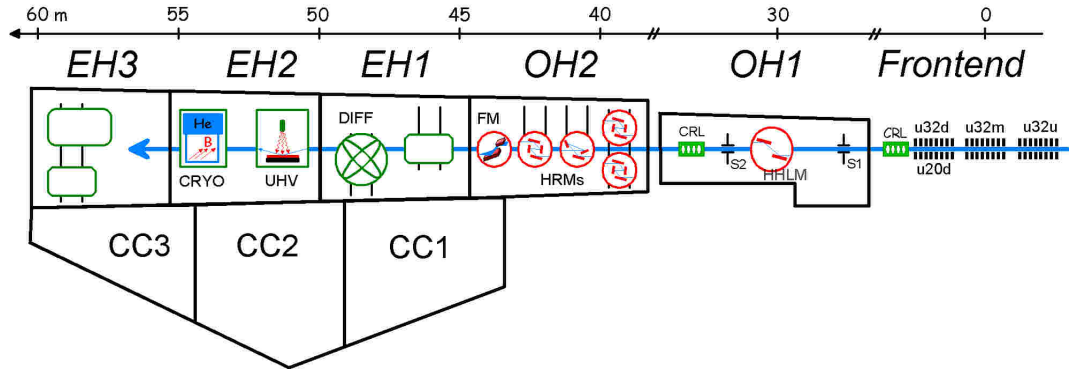

Figure 3.6: Schematic drawing of the ID18 beamline: From right to left: FE - Front End; U32u, U32m, and U32d/U20d - undulators; OH1, OH2 - optics hutches, EH1, EH2, and EH3 - experimental hutches, CC1, CC2, and CC3 - control cabins, CRL - focusing and collimating compound refractive lenses, S1 and S2 - slit systems, HHLM - high heat-load monochromator, HRMs - high-resolution monochromators, FM - focusing monochromator, DIFF - diffractometer, UHV - set-up for in-situ preparation, characterization and NRS measurements of surfaces and interfaces, CRYO - cryomagnetic system. Figure taken from [38].

are placed between the two monochromators to match the divergence of the incoming x-ray beam to the angular acceptances of the HRM. A second set of CRLs is placed after the HRM to focus the beam (in the vertical direction) down to 30 μm. This option is usually used to match the beam cross section to the apparent sample size in grazing incidence geometry. Three experimental hutches are available. EH1 is equipped with a 6-circle diffractometer. EH2 is equipped with a cryomagnet (temperature range 4 K<T<300 K and up to magnetic fields of 7 T) and an UHV system for surface science studies [40]. The last hutch EH3 is usually free and can be used to mount large user experimental setups, as it was the case for the *in-situ* experiments described in **Papers I** and **II**.

3.4 Polarized neutron reflectometry

The scattering formalism developed in section 3.1 can be applied to the case of grazing incidence neutron scattering as well. The main difference compared to x-rays is that neutrons interact with the nucleus and the magnetic moments of atoms. Because of the nuclear interaction involved, the technique is isotope sensitive. The corresponding nuclear scattering length can differ greatly for isotopes of the same element. The neutron has also a spin which interacts with the magnetic moment of the atoms in the case of a magnetically ordered medium. The magnetic scattering length is here proportional to the magnetic moment of the atoms. A neutron reflectivity curve is sensitive to the variation of the sum of the nuclear and magnetic scattering length along the depth of the sample.

One of the advantages of polarized neutron reflectometry lies in the possibility to easily control the polarization state of the neutron. This renders polarization analysis of the scattering process a decisive tool for the determination of the magnetic moments orientation in thin films and multilayers.

Nuclear and magnetic scattering length

Grazing incidence neutron scattering by a multilayered sample is usually described by a depth dependent scattering potential:

$$V(z) = V_n(z) + V_m(z) = V_n(z) \pm \underline{\vec{\mu}} \cdot \vec{B}(z) \tag{3.18}$$

which is the sum of the nuclear and magnetic scattering potential. $\underline{\vec{\mu}}$ is the neutron spin and $\vec{B}$ is the magnetic flux density. The scalar product already indicates that V_m will depend on the orientation of the magnetic moment relative to the neutron spin. The polarization dependence of the total neutron scattering length will be entirely due to the magnetic part of the interaction.

V_n can be expressed in terms of the nuclear scattering length density (SLD) $\rho_n(z)$:

$$V_n = \frac{2\pi\hbar}{m_n}\rho_n(z) \tag{3.19}$$

where m_n is the neutron mass. In the case of grazing incidence reflection from a homogeneous medium, ρ_n is defined by:

$$\rho_n = \sum_i^J N_i b_i \tag{3.20}$$

where J is the number of distinct isotopes in the material and N_i and b_i are the number density and the coherent neutron scattering length for the ith species. The expression for V_n is similar to what would be obtained from conventional x-ray reflectometry, apart of the isotope sensitivity of the neutron SLD. The magnetic SLD ρ_m is of similar amplitude to the nuclear one, and is proportional to the magnetic moment of the atom:

$$V_m = \frac{2\pi\hbar}{m_n}\rho_m(z) \qquad \text{with} \qquad \rho_m = C\sum_i^J N_i\mu_i \tag{3.21}$$

where C=2.645×10^{-5}Å/μ_B is a constant and μ_i the magnetic moment per formula unit. The scattering potential difference in the sample relative to the surrounding medium can then be written in matrix notation, taking into account the polarization convention of Fig. 3.7:

$$\delta\boldsymbol{V}(z) = \frac{2\pi\hbar^2}{m_n}\begin{pmatrix} \rho_n + \rho_{mz} & \rho_{mx} - i\rho_{my} \\ \rho_{mx} + i\rho_{my} & \rho_n - \rho_{mz} \end{pmatrix} \tag{3.22}$$

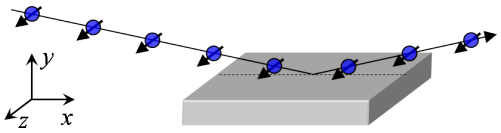

Figure 3.7: Scattering geometry for polarized neutron reflectometry (in the case of non-spin-flip reflection). The neutron spin is parallel to z.

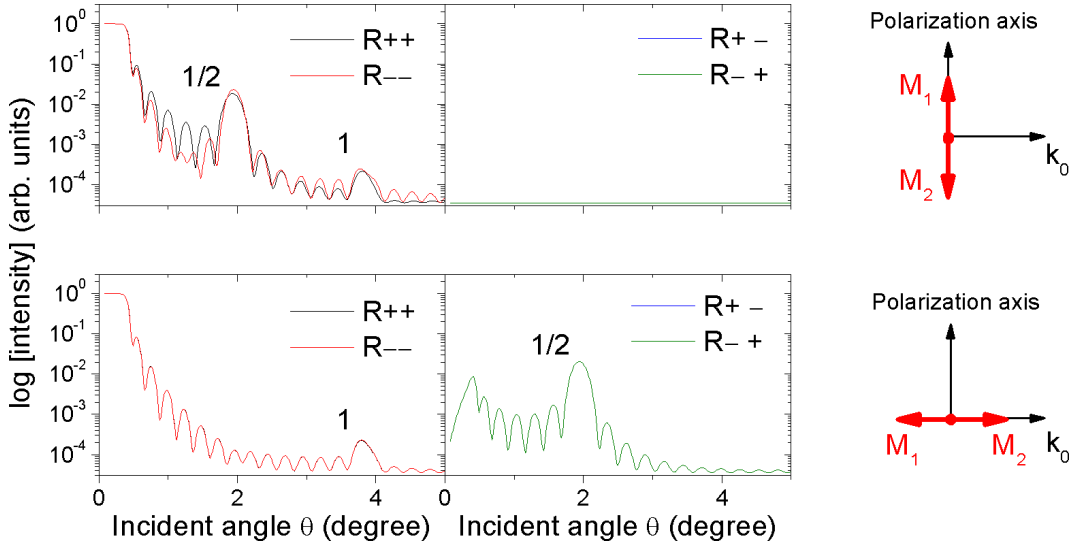

Figure 3.8: Simulated polarized neutron reflectivity curves of a magnetically coupled Si/[Fe(1.8nm)/FeO(1.6nm)]$_{15}$/Al multilayer. The neutron wavelength is 0.441 nm (the same as at the ADAM reflectometer). This illustrates the different magnetic sensitivity of the different scattering channels. The non spin-flip-channels (R++ and R−−) are sensitive to the nuclear SLD depth profile and the magnetic moment projection along the neutron polarization axis. The spin-flip channels (R−+ and R+−) are only sensitive to the projection of the magnetic moments on the propagation axis $\vec{k_0}$.

This leads to four different SLD for the four different scattering channels:

$$\begin{aligned} \rho_{++} &= \rho_n + \rho_{mz} \\ \rho_{--} &= \rho_n - \rho_{mz} \\ \rho_{+-} &= \rho_{mx} - i\rho_{my} \\ \rho_{-+} &= \rho_{mx} + i\rho_{my} \end{aligned} \tag{3.23}$$

The first two terms are called the non-spin-flip channels, and the spin polarization is unchanged during the scattering process. These channels are sensitive both to the nuclear scattering length depth profile and the magnetic moment depth profile along the polarization direction. The last two terms are the spin-flip channels and involve a 180° rotation of the neutron spin in the scattering process. These

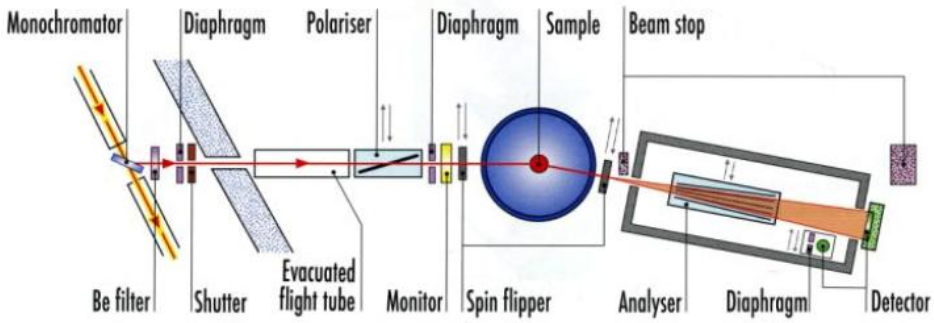

Figure 3.9: Schematic drawing of the ADAM reflectometer. Picture taken from [41].

channels are uniquely sensitive to the magnetic moments that are perpendicular to the spin polarization and in the plane of the sample. Because there is no contribution from the nuclear scattering length in the spin-flip channels, they are highly sensitive to any magnetic moment orientation on that axis. The difference between spin-flip and non-spin-flip channels is illustrated in Fig. 3.8 for the case of an antiferromagnetically coupled multilayer. If the magnetic moments are parallel to the polarization axis, the depth variation of the total SLD leads to half-order Bragg peaks in the non-spin-flip reflectivities. As there are no moments pointing perpendicular to the polarization axis, no signal appears in the spin-flip reflectivities. If the moments are perpendicular to the polarization axis, the magnetic superstructure disappears in the non-spin-flip reflectivities and re-appears in the spin-flip reflectivities.

The fact that the magnetic scattering length is directly proportional to the magnetic moment of atoms can be used to determine the absolute magnetic moment in each layer of a multilayered film. The polarization analysis allows to fully determine the moment orientation.

Experimental setup at ADAM

The polarized neutron reflectometry experiments were performed at the ADAM reflectometer at the Institute Laue Langevin (ILL) [42]. The layout of the instrument is shown in Fig. 3.9. Neutrons with a wavelength of 0.441 nm are selected by a HOPG(002) monochromator and reflected towards the experimental station. A first polarizer is used to define the polarization of the neutron beam. The sample itself is placed in the center of a dipole magnet (maximum field $\approx 500\,\mathrm{mT}$). The analyzer is a supermirror used to filter neutrons with defined spin orientations before the neutron reaches the detector. The supermirror is magnetized and neutron impinges on the mirror at the critical angle of the R++ reflection. This way only + oriented neutron are reflected by the analyzer. The polarization analysis is carried out using two spin flipper placed before and after the sample. By activating the front spin flipper one can decide which polarization (+ or −) the neutron will have

when reaching the sample. The back spin flipper is used to determine which neutron spin orientation should pass through the analyzer. This way one can record the four channels of the neutron reflectivity.

3.5 Comparison between GI-NFS and PNR

Having discussed the particularities of NFS and PNR for the study of thin magnetic films, it is worth to summarize what information the two techniques can provide:

Nuclear forward scattering

- (Almost) background free nuclear signal
- Magnetic moment orientation - no determination of the absolute direction in which the moment is pointing
- Magnetic depth profile
- Hyperfine parameters - magnetic and electronic configuration of the atom
- Tracer layer technique to selectively probe the magnetic structure

Polarized neutron reflectometry

- Isotopic depth profile
- Magnetic depth profile
- Polarization analysis - complete magnetic moment orientation (in-plane)
- Absolute measure of the atomic magnetic moment
- Possibility to vary the contrast by use of isotopic layers

As can be seen, magnetic information can be retrieved by both techniques. However, they do complement quite well in the case of systems where Fe is present in every part of the multilayer, as it is the case for Fe/Fe-oxide multilayers. The use of isotopic probe layers placed either in the metal or in the oxide part allow one to isolate the magnetic contributions of each part independently by NFS while the contrast between adjacent metal/oxide layers is highlighted using PNR.

It should be noted that the development of high brilliance third generation synchrotron sources has brought the NRS technique to a stage where studies with sub-monolayer sensitivity can be carried out routinely. These advances render possible *in-situ* studies of ultrathin layer magnetism in an ultra-high vacuum environment, as it is demonstrated in **Paper I** and **Paper II**. Compared to PNR, the high degree of collimation of the x-ray beam enables one to study relatively

small samples in grazing incidence. This is important in cases of thickness inhomogeneities one encounters when growing large samples. The relatively low intensity delivered by present neutron sources prevents large systematic studies of magnetic thin films. As an example, a typical nuclear resonant reflectivity curve on a Fe/Fe-oxide multilayer is acquired within 30 minutes whereas a PNR curve needs more than 12 hours acquisition to cover the same q range.

3.6 X-ray absorption spectroscopy

X-ray absorption spectroscopy (XAFS) at the K-edges of elements is a powerful tool to probe the local environment of atoms in an element specific manner. As can be seen on Fig. 3.10a, spectroscopy at the absorption edge is divided into two parts: While the near edge structure (XANES) provides information regarding the chemical environment, the study of the x-ray absorption extended fine structure (EXAFS) can yield quantitative information concerning the local order around the absorbing atom (*i.e.* first nearest neighbor distance, coordination number), even for disordered or amorphous materials. This technique was applied in this work to perform an *in-situ* study of the oxide formation, which is detailed in **Paper III**. This gives a direct quantitative insight into the chemical and structural configuration of the buried oxide present in Fe/Fe-oxide multilayers. The present section aims at presenting the basic features of the technique, together with some discussion on the experimental procedure required to perform the experiment on ultra thin films in an ultra-high vacuum environment.

Origin of the absorption edge

A traditional XAFS experiment measures the absorption coefficient $\mu(\omega)$ of the sample as a function of the incoming photon energy. $\mu(\omega)$ increases dramatically at the absorption edges, when the incident photon energy matches a transition energy of the absorbing element. Because the position of the energy level varies with the valence state of the atom, the XANES is highly sensitive to the effective valence of the probed element. In a simple picture, the absorption edge should lead to a sharp increase of the absorption coefficient at a given energy. However, the situation is more complicated and a XANES spectrum usually shows pre-edge and post-edge features that cannot be explained by a simple one electron excitation model. These features are usually due to multiple scattering of the excited electron with the surrounding atoms and are difficult to analyze quantitatively (detailed discussion of these effects can be found in [43]). For that reason, the XANES part of the absorption signal is not only sensitive to the valence state of the atom but also to its local surrounding.

Calculation of exact XANES spectra has remained a difficult task for a long time. This is because the low energy electrons ejected from the atoms are multiply scattered by the surrounding elements, which perturbs the absorption spectrum. However, simulation packages like FEFF 8 [44] have been developed to take into

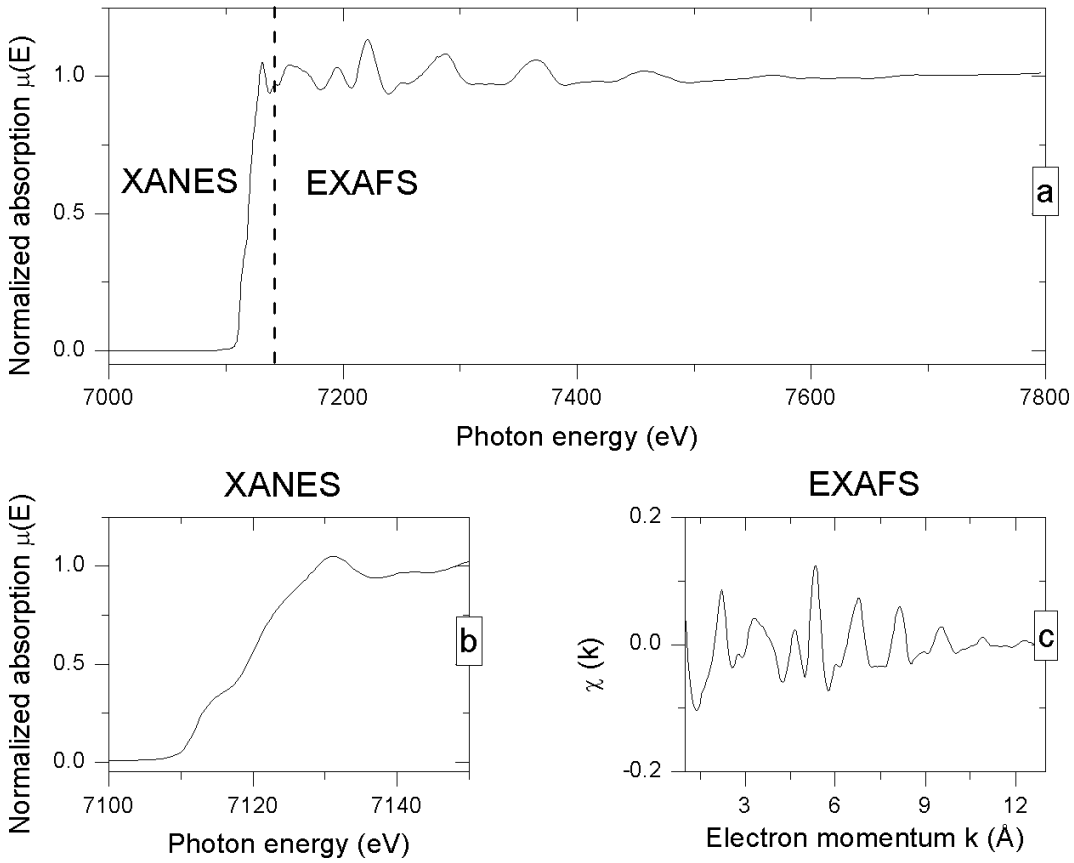

Figure 3.10: a) Fe K-edge XAFS spectrum of bulk metallic Fe. Two parts of the spectrum are usually distinguished. b) The near edge region (XANES) study the shape and position of the absorption edge. c) The extended fine structure spectroscopy (EXAFS) of the edge study the subsequent oscillations of the absorption coefficient at higher energy.

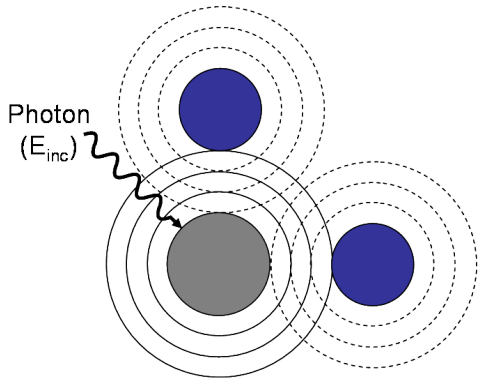

Figure 3.11: Schematic view of the electronic interference effects in EXAFS. The surrounding atoms act as point scatterers for the emitted electron wave. Interaction of the emitted and backscattered electron wave results in interference effects which leads to a modulation of the absorption coefficient as a function of the electron momentum.

account multiple scattering effects. An exact match between the calculated and experimental data is however achieved only in a limited number of cases.

Because the shape of the absorption edge (position + fine structure) is characteristic for a given valence state and environment, the analysis of the XANES can on the other hand be used as a fingerprint of the presence of a known element. In the case of a multicomponent material where different phases are present, the resulting XANES spectra can be described as a linear combination of the spectrum of the individual species. The relative concentration of each species corresponds to the weight of the corresponding sub spectrum in the linear combination. This analysis scheme was used in **Paper III** to resolve the different oxide phases present in a native oxide layer using spectra of known reference oxide phases.

Extended fine structure

The analysis of the extended fine structure (EXAFS) has an important advantage compared to XANES. The much higher kinetic energy of the ejected electrons (between 100-1000 eV) renders the signal much less sensitive to multiple scattering, which can usually be neglected or calculated in an easier way.

The origin of the EXAFS oscillations can be understood if one looks at the wave nature of the electron. The ejected electron wave has a certain wavelength and the surrounding atoms can be seen as point scatterers from which the electron can be scattered back towards the absorbing atom. As can be seen on Fig. 3.11, the overlap of the forward and backscattered waves leads to interference phenomena which modify the absorption coefficient and hence show up as oscillation in the EXAFS signal, as shown in Fig. 3.10c for bulk metallic Fe. Because the energy of the electron (and hence its wavelength) is continuously varying in an EXAFS experiment, the EXAFS oscillations are characteristic for the distance between the absorbing and surrounding atoms as well as their type and spatial arrangement. Information like radial distribution and number of nearest neighbors can therefore be retrieved by fitting the EXAFS oscillation pattern.

It should be noted that the basic principle of the technique does not rely on

any long range crystalline order of the absorbing atoms. This technique is therefore well suited to investigate local order in systems which do not present long range ordering, like glasses and amorphous materials.

The typical strategy to fit the EXAFS signal is to first perform a Fourier transform from the k space (electron momentum) to the r space. This way one obtains the radial distribution of atoms around the scatterer. High frequency oscillations are then filtered by back Fourier transform of the radial distribution constrained to the first (or second) subshells. The filtered EXAFS signal can be fitted using model calculation of the local arrangement around the atom.

Detection of the XAFS signal

In a normal hard x-ray XAFS experiment, the absorption coefficient of x-rays in the material is measured in transmission geometry by monitoring the intensity of the x-ray beam before and after the sample as a function of the incident photon energy. However, two other channels can be used to record the absorption signal. As can be seen on Fig. 3.12a, the absorption of x-ray by the atom is accompanied by the emission of a photoelectron with kinetic energy $E_k = E_{inc} - E_B$, where E_{inc} is the energy of the incident photon and E_B the energy of the electronic level involved. The atom is now in an excited state with a hole in one of its core shells. This hole can be filled by an electron from a higher energy level. When falling to the core level, the excess energy of the electron is dissipated either by fluorescent emission of a photon (Fig. 3.12b) or by energy transfer (Auger process) to an electron from a neighboring energy level (Fig. 3.12c). This latter Auger electron has enough energy to escape the atom.

In the case where thin layers are deposited on thick absorbing substrates, the transmission geometry cannot be applied and other detection schemes have to be used. In fact, one can record the yield of fluorescent photons (FY) using an energy dispersive detector, or measure the drain current produced by the photoabsorption. Since both the photoelectrons and the Auger electrons will contribute to the total current, together with secondary electrons produced by scattering of higher energy electrons, the method is called total electron yield (TEY) detection. Because the technique will measure a current generated by the electrons that effectively escape the sample, it has a limited probing depth which is related to the mean free path of electrons in matter. For hard x-ray excitation, this mean free path is estimated to be around 50-100 nm [45].

The fluorescence yield is a single photon counting measurement where the photon energy is analyzed using an energy dispersive detector . However the method suffers from self absorption effects which can drastically reduce the amplitude of the EXAFS oscillation and the shape of the absorption edge. This is because the fluorescent photons have a large probability of being reabsorbed by matter, an effect which is predominant in the case of dense samples. This effect can be corrected [46] but requires good knowledge regarding the composition of the sample and the geometry of the experiment. Self absorption effects are almost not present

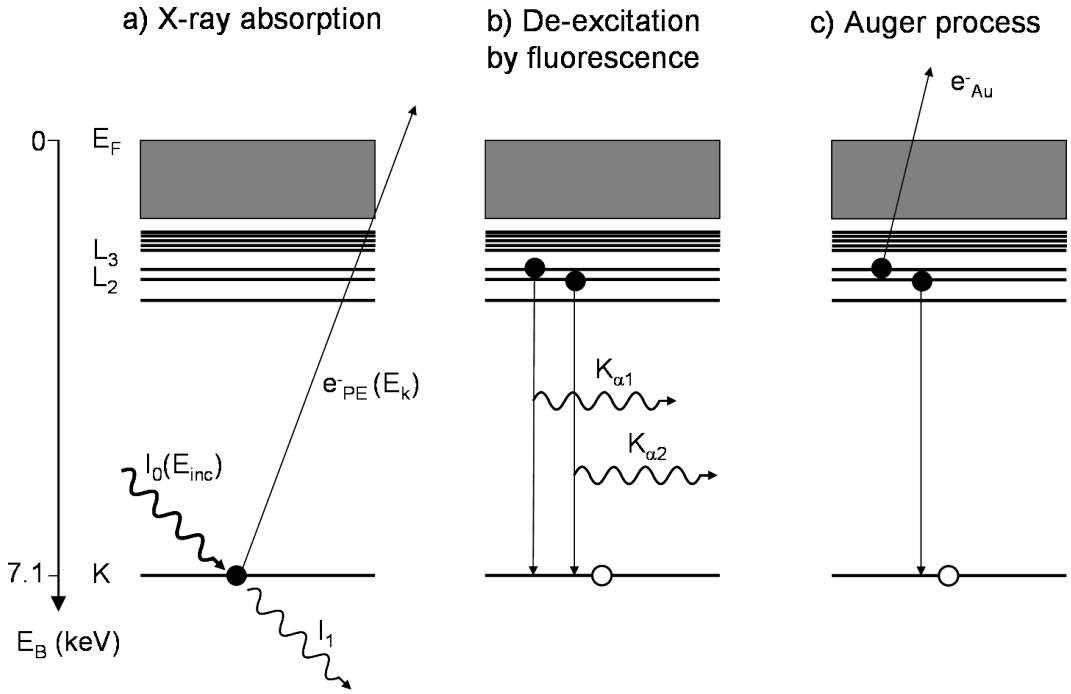

Figure 3.12: a) Description of the x-ray absorption process at the Fe K-edge. The absorption of the x-ray photon is accompanied by the ejection of a photoelectron. After the absorption, the atom is in an excited state with a hole in the core level. Two de-excitation paths are possible. b) De-excitation by fluorescent emission of a photon with defined energy. c) Auger process: the energy loss of the electron is transfered to an electron from an adjacent orbital, which is ejected from the atom with a characteristic energy.

in the TEY signal, which therefore resemble closer to the true absorption signal.

The XAFS experiment were performed at the A1 beamline of the DORIS III storage ring. As described in **Paper I**, the two detection schemes were implemented on the UHV deposition system used in this work. The extreme sensitivity achieved by the TEY detection allows one to carry out XAFS experiments on monolayer thick layers at second generation x-ray sources.

Chapter 4

Oxidation processes on Fe surfaces

Fe/native-oxide multilayers incorporate ultrathin oxide layers produced by controlled oxidation of Fe at room temperature. A detailed study of the structure of this oxide is mandatory to understand the electrical and magnetic properties of the system. Although the existing body of scientific knowledge on bulk iron oxide and oxidation processes is very large, there is still a lively debate in the literature concerning the structural and magnetic properties of thin oxide layers produced by controlled exposure to oxygen. This is in part due to the fact that Fe exhibits two coexisting valence states leading to several stable iron oxide phases, which are more or less likely to form depending on the growth conditions.

Understanding the properties of the buried native oxide will be a central part of this work. In this chapter, a short review of the state-of-the-art knowledge of iron oxidation is given. First, a brief description of the properties of the different bulk iron oxides is presented. The second part deals with the oxidation kinetics, both from a theoretical and experimental point of view. A short review of the observed structural and magnetic properties of oxidized iron surfaces is presented. The last part deals with the reported particular properties of buried native oxide, which triggered this study.

4.1 Bulk iron oxides

The complexity of oxidation processes on Fe surfaces comes from the fact that there exist several stable iron oxide phases. While hydroxides play an important role in natural oxidation processes, this section describes the pure bulk iron oxide (composed only of Fe and O atoms), as they are relevant for the case of iron oxidation in a controlled ultra-high vacuum environment. One can list four oxide phases of increasing thermodynamic stability: Wüstite ($Fe_{1-x}O$), magnetite (Fe_3O_4), maghemite (γ-Fe_2O_3) and hematite (α-Fe_2O_3). In nature, the formation of these oxides is driven by the external conditions like availability of chemical species, pressure and temperature.

From a structural point of view, these four iron oxides can be described as Fe atoms distributed at interstitial positions in a close packed oxygen lattice [47]. The

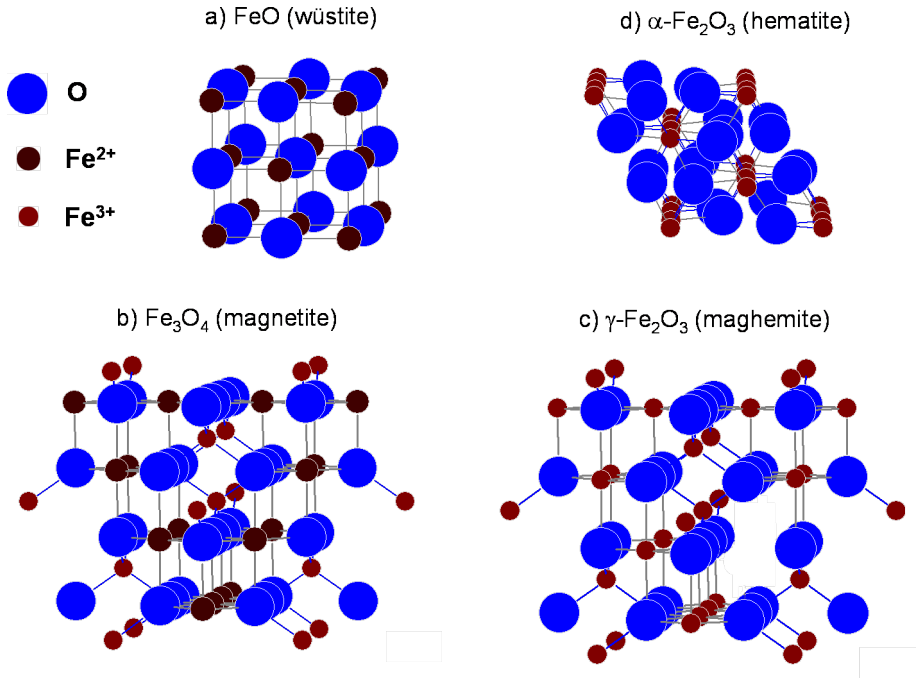

Figure 4.1: Representation of the unit cell for the 4 different bulk iron oxide phases.

oxygen anions have a much larger radius (0.14 nm) compared to the Fe cations (0.065 nm and 0.082 nm respectively for Fe^{3+} and Fe^{2+}). The arrangement of the close packed anions governs the crystal structure and determines the ease of change from one phase to the other. One can distinguish two types of crystallographic sites for the Fe atom, either in tetrahedral (4 surrounding oxygen atoms) or octahedral (6 surrounding oxygen atoms) environment. In the following section, a summary of the crystallographic and magnetic properties of the four iron oxide phases is given.

$Fe_{1-x}O$ - Wüstite

Wüstite exhibits a rocksalt crystal structure composed of two interconnected face centered cubic (FCC) structures of Fe^{2+} and O^{2-} with a lattice spacing of 0.43 nm, as depicted in Fig. 4.1a. Practically, a 1/1 stoichiometry is never obtained and a deficiency of Fe cations is observed. The crystal structure incorporates defects like cation vacancies in a octahedral position or Fe^{3+} ions in tetrahedral positions.

Defect free FeO is superparamagnetic at room temperature but undergoes a transition to an antiferromagnetic state at its Néel temperature of 198 K (a value which depends on the stoichiometry). However, it has been demonstrated [47] that the intrinsic defect clusters present in $Fe_{1-x}O$ adopt the inverse spinel structure of magnetite, thus inducing some parasitic net magnetic moment in $Fe_{1-x}O$ films. In fact, Fe_3O_4 magnetite can be seen as a giant defect cluster of $Fe_{1-x}O$ with $x = 1/4$.

Wüstite is usually considered as a p type semiconductor with a bandgap of 2.3 eV [48].

Fe_3O_4 - Magnetite

Magnetite is one of the most well known oxide because of its high stability and its intrinsic magnetic moment. It has an inverse spinel structure with a lattice parameter of 0.83 nm (along the c axis), shown on Fig. 4.1b. 64 tetrahedral sites in the unit cell are occupied by 8 trivalent Fe ions. 16 Fe^{2+} and 16 Fe^{3+} cations are distributed in octahedral sites. At room temperature, a fast electron hopping between the divalent and trivalent ions in octahedral positions renders these sites equivalent. This fast electron hopping is frozen in at the Verwey transition [49] which occurs at 125 K, where magnetite undergoes a metal to insulator transition.

Magnetite is ferrimagnetic at room temperature. In fact, superexchange through the oxygen ions leads to an antiparallel arrangement of the moments of the trivalent ions in tetrahedral and octahedral sites. The magnetic moment of divalent ions is not compensated and accounts for the net magnetic moment of magnetite.

Magnetite has the smallest resistance of all iron oxides and behaves as a semi-metal.

γ-Fe_2O_3 - Maghemite

Maghemite adopts a defect spinel structure similar to magnetite, apart that all Fe ions are in a trivalent state and that periodic defects are present, as depicted in Fig. 4.1c. Maghemite is a ferrimagnet at room temperature. The origin of the uncompensated magnetic moments is the same as for magnetite.

α-Fe_2O_3 - Hematite

Hematite is the thermodynamically most stable iron oxide. It crystallizes in a rhomboedral structure similar to corundum. Hematite usually forms at elevated temperatures (above 500 K) and is therefore not likely to form in oxidation processes at room temperature. As can be seen on Fig. 4.1d, the presence of adjacent oxygen ions on the same atomic plane leads to an ordered displacement of the anions. At room temperature, hematite is an antiferromagnet with some parasitic magnetic moment (that vanishes below the Morin transition at 260 K).

4.2 Controlled oxidation of iron

Iron is one of the elements with the highest tendency to oxidize in contact to oxygen, water and hydroxides. Because of its wide use in metallic alloys, the study of the oxidation properties of Fe has generated a large amount of research over the decades. A complete review of all the physics related to iron oxidation in general is well beyond the scope of this work. This section therefore focuses on the mechanism relevant for this study, namely the controlled oxidation of Fe by exposure to molecular oxygen only. The first part deals with the oxidation kinetics of Fe surfaces, reviewing the theoretical description together with some

experimental findings. The second part reviews the observed properties (structural and magnetic) of thin oxide films grown at room and elevated temperature.

Oxidation kinetics

Most of the theoretical work regarding the oxidation kinetics of metal were performed between 1930 and 1970. The basic concept is that oxidation of a metal takes place at the oxide/oxygen interface and that charged ions have to be transported from the bulk to the surface. The original theory of Mott [50] postulated that the oxidation kinetics is driven by the possibility for Fe ions to diffuse from the metal to the oxide/oxygen interface. Fromhold and Cook [51] later generalized this model by introducing the concept of a coupled current mechanism where both Fe ions and electrons are transported to the boundaries of the growing oxide layer. A synopsis of this theory is presented hereafter.

The Fromhold and Cook (FC) theory considers both ionic and electron transport through the oxide film during the growth. This transport is constrained by the condition that no net electric charge transport across the oxide should occur:

$$\sum_j q_j J_j = 0 \tag{4.1}$$

where q_j and J_j are the net charge and the flux of each species, respectively. Respecting this condition at all times ensures charge balance and will lead to different oxidation regimes whether the electron flux or the cation flux is the rate limiting factor for oxidation. The driving force for the cation or electron transport is best understood by looking at the electron energy diagram for the metal/oxide/oxygen system. In the steady state shown in Fig. 4.2a, there is no electric field in the oxide. The height of the energy barrier for electron tunneling depends on the value of χ_0 and χ_L which are the metal/oxide and oxide/oxygen workfunctions respectively. The diffusion of ions through the oxide is limited by the possibility for the ions to hop from site to site, which are represented by energy minima in the right panel of Fig. 4.2a. The energy barrier is defined by its width being the ionic jump distance $2a$ and its height, the effective energy barrier W. A good part of the FC theory deals with the identification of the expression for ion and electron flux, which are related to the energy diagram represented in Fig. 4.2a.

Ion flux

In the steady state approximation, which implies that the flux is independent of the position in the oxide, the flux of ionic species is influenced only by a concentration gradient and a homogeneous electric field E_L (the origin of which will be described later). The ion flux J_i is given by [54]:

$$J_i = 4a\nu \exp(-\frac{W}{kT}) \sinh(\frac{Z_i e E_L a}{kT}) \times \left[\frac{C_L - C_0 \exp(\frac{Z_i e E_L L}{kT})}{1 - \exp(\frac{Z_i e E_L L}{kT})}\right] \tag{4.2}$$

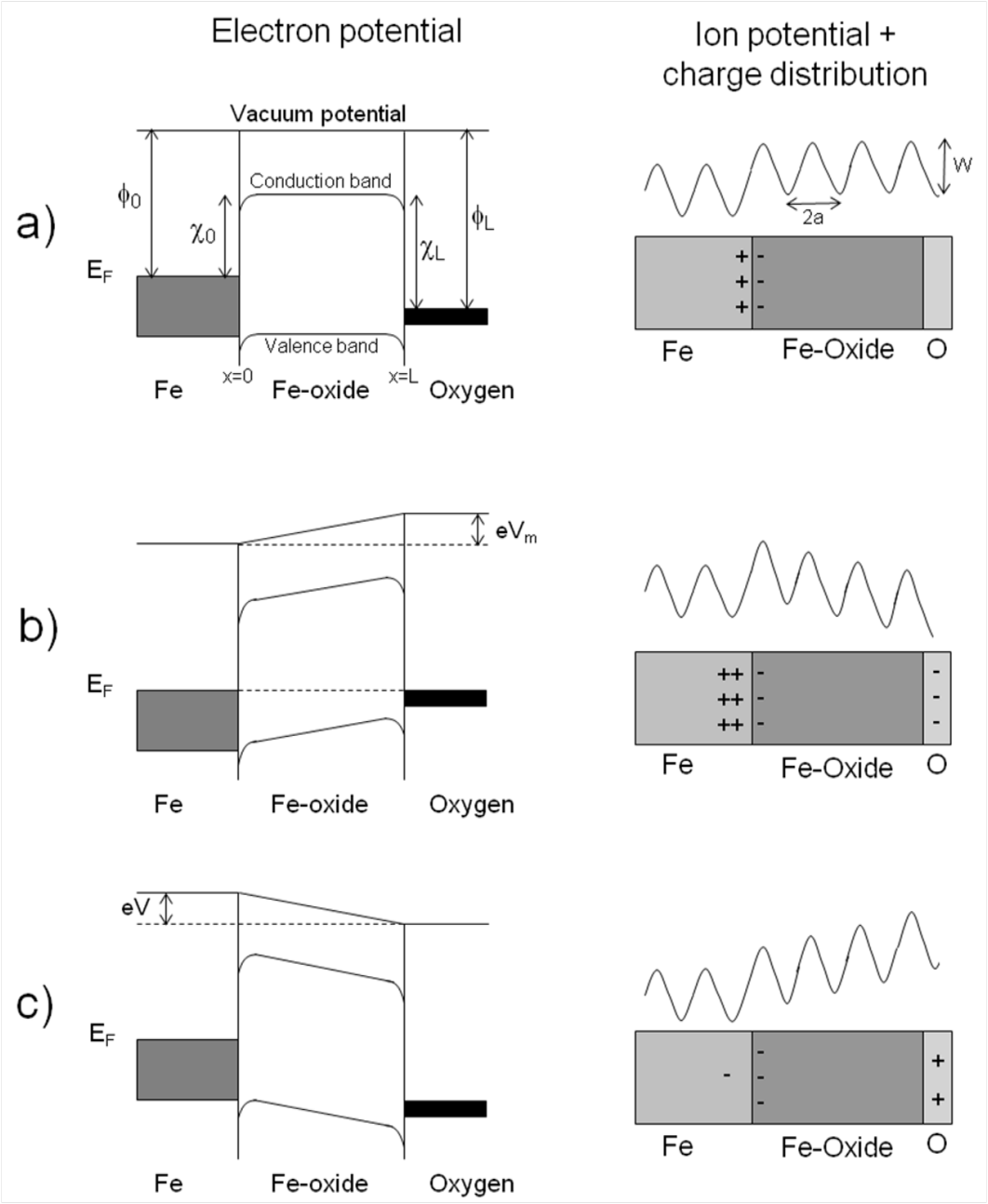

Figure 4.2: Energy diagram for electrons (left panel) and ions (right panel) for the metal/oxide/oxygen layer system. a) Equilibrium state without charge transfer from the metal to the oxygen. ϕ_0 and ϕ_L are the metal and oxygen workfunctions respectively. χ_0 and χ_L are the metal/oxide and oxide/oxygen workfunctions respectively. E_F is the Fermi level. b) Cation supply limited growth. The Mott potential $V_m = \chi_0 - \chi_L$ appears across the oxide which lowers the barrier for ionic diffusion and promotes transport of cation to the oxide/oxygen interface. c) Electron tunneling limited growth. A potential appears across the oxide which decreases the tunnel barrier and promotes electron transfer.

where $2a$ is the ionic jump distance, ν the ionic jump frequency, W is the energy barrier for ionic motion, k the Boltzmann constant, T the temperature, Z_i the effective charge of the diffusing ion in unit of the elementary charge e, L the instantaneous film thickness and C_0 and C_L are the concentrations of the diffusing species at the metal-oxide ($z = 0$) and oxide-oxygen ($z = L$) interface, respectively. The first exponential describes the influence of the energy barrier while the hyperbola sinus accounts for the presence of an electric field. The last term represents the influence of the concentration gradient.

Electron flux due to tunneling

There are two possibilities for electrons to cross the oxide's energy barrier: Either by quantum tunneling or thermionic emission. Tunneling is the main electron transport mechanism at room temperature while thermionic emission is determining at elevated temperature and large film thickness. Leibbrandt et al. [52] have confirmed that electron tunneling is virtually the only electron transport mechanism at room temperature. Thermionic emission will therefore be neglected in this section.

At $T = 0\,\mathrm{K}$ the electron flux for tunneling through the oxide energy barrier is:

$$J_{e,tn} = \frac{1}{8\pi^2\hbar L^2}\left[(2\chi_0 + eE_L L) \times \exp\left(-\frac{2\sqrt{m}L}{\hbar}\sqrt{(2\chi_0 + eE_L L}\right)\right.$$
$$\left. - (2\chi_L - eE_L L) \times \exp\left(-\frac{2\sqrt{m}L}{\hbar}\sqrt{(2\chi_L - eE_L L)}\right)\right] \quad (4.3)$$

where m is the electron mass, χ_0 is the energy difference between the bottom of the conduction band in the oxide and the Fermi level of the metal and χ_L is the energy difference between the bottom of the conduction band in the oxide and the O^- level of the adsorbed oxygen. χ_0 and χ_L are referenced as the metal/oxide and oxide/oxygen workfunctions respectively. A first order approximation for the temperature dependence of $J_{e,tn}$ is [54]:

$$\frac{J_{e,tn}(T)}{J_{e,tn}(0)} = \pi\frac{\sqrt{2m}L}{\sqrt{\chi_0}\hbar}kT \Big/ \sin\left(\pi\frac{\sqrt{2m}L}{\sqrt{\chi_0}\hbar}kT\right) \quad (4.4)$$

Experimental confirmation

The application of the coupled current mechanism summarized above has several implications concerning the oxidation rate of a transition metal. Three main oxidation regimes can be derived, depending on whether the reaction is limited by supply of oxygen, Fe cations or electrons.

At the early stage of the oxidation, Fe cations and electrons are readily available at the surface and oxidation is limited only by the oxygen supply. This process ends rapidly when a continuous oxide layer is formed.

The second stage of oxidation is usually characterized by a cation supply limited growth. The oxide layer is so thin that electrons can still easily tunnel through the layer. This leads to an equilibrium between the Fermi level of the metal and the O^- level of the adsorbed oxygen. The result is the appearance of the Mott potential $V_m = \chi_L - \chi_0$ across the oxide. This potential difference appears across a nanometer thick oxide layer and therefore results in very large electric fields (larger than 10^6 V/m), sufficient to reduce the energy barrier for cation diffusion, as shown in Fig. 4.2b. At this stage, the oxide thickness growth rate can be described by a parabolic law $\sqrt{t}$, where t is the oxidation time. Afterwards, the progressive increase of the oxide layer thickness leads to a reduction of the electron supply and the potential across the barrier deviates from the initial value V_m. The growth rate does not follow a parabolic law anymore but follows a more complicated time dependence, governed by the coupled currents condition.

At larger oxide thicknesses, the electron current due to tunneling decreases drastically and a fast decrease of the oxidation rate is observed. At that stage, the oxide growth stops.

Several studies on polycrystalline [53, 54] as well as on single crystalline [55, 56, 57] surfaces have successfully applied the coupled current mechanism to describe the oxidation kinetics of Fe at room and elevated temperatures. They confirmed that the FC model efficiently describes the oxidation of iron surfaces, the consequence being that oxidation is limited either by the cation supply or the electron supply, depending on the thickness of the oxide layer.

Additionally to these general considerations, a study of the oxidation kinetics on Fe single crystals [55] showed that the oxidation rate can be up to five times higher on Fe(100) than on Fe(110) surfaces. This proved that surface orientation, and therefore the cation density at the surface, plays an important role in the oxidation kinetics. The oxygen pressure (in the range 10^{-8}-10^{-6} mbar) seems to have little influence on the oxidation kinetics [56]. More recently, Roosendaal *et al.* [57] showed that the cation diffusion through the oxide is hindered once an oxygen rich oxide (consisting mainly of Fe^{3+} ions) has formed. In that case, the oxidation at room temperature is effectively limited by the cation diffusion and not by electron tunneling.

The finding that an Fe^{3+} rich layer acts as an effective barrier for cation diffusion is a proven example that oxidation processes on Fe surfaces are more complex than what can be derived from the original FC theory. The composition and the type of oxide grown will play an important role for the kinetics and, in turn, for the chemistry of the layer. Finally, the FC model does not describe the type of oxide that forms. For that reason, a dedicated study of the composition and structure of native oxides is of utmost importance to understand their electrical and magnetic properties.

Composition and magnetism of oxidized Fe layer

Besides the kinetic aspects that are important for controlled oxide growth by oxygen exposure, the composition of the oxide formed is crucial, as it is closely related to its magnetic properties. The exact structure of the grown oxide is still a matter of debate but several tendencies can be derived from the literature [56, 57, 58, 59]:

At the early stage of the oxidation, the large availability of Fe metal promotes the growth of oxides with predominantly Fe^{2+} type of sites. With increasing exposure, the creation of Fe^{3+} is promoted and the ratio Fe^{2+}/Fe^{3+} decreases. Roosendaal *et al.* [57] proposed a two layer model for the oxide growth were first an Fe^{2+} containing layer is formed. With increasing exposure, an Fe^{3+} overlayer is created, keeping the Fe^{2+} layer in the lower part of the oxide.

Some studies reported the eventual presence of Fe^0 metal in the grown oxide [56, 57]. This puzzling result is up to now not settled because of the influence of the underlying metallic substrate, which can possibly disturb the detection of a weak Fe^0 signal originating from the oxide layer.

There are a few studies related to the crystalline ordering of oxide grown by exposure to oxygen at room temperature, but it is usually expected that such a layer does not exhibit long range crystalline order. This is mainly due to the low mobility of ions, which prevents crystalline reconstruction. In the same sense, these oxides typically form a magnetically dead layer.

At elevated temperatures on the other hand, many studies reported crystalline and magnetic ordering [58, 59, 60, 61]. In the case of low pressure oxidation and temperatures of 450-500 K, the formation of an FeO layer is often reported. There was an intense debate regarding the oxidation of Fe(110) at elevated temperature. Koike *et al.* [62] reported the formation of an Fe_3O_4 layer which was ferrimagnetically ordered above a magnetically dead FeO layer, and magnetically coupled antiparallel to the underlying Fe substrate. This finding would have suggested a new type of magnetic coupling through a non-magnetic spacer. However, Kim *et al.* [61] have shown that in fact the complete layer was Fe_3O_4, and the magnetic coupling is uniquely due to direct exchange at the interface.

While these systems differ largely from the one studied in this work (single crystalline oxide grown at elevated temperature compared to polycrystalline substrates oxidized at RT), these studies show how complicated the oxidation of Fe surfaces can be when discussing the structural and magnetic properties of the formed oxide. In particular, quantitative determination of the composition of the oxide is still a critical issue.

If one wants to study the properties of the buried oxide in a Fe/native-oxide multilayer, it is mandatory to understand the properties of the free oxide layer which is formed and follow the transition to the case of the buried oxide, when the oxide is covered with Fe metal. These considerations triggered the study presented in **PAPER III**, where the oxidation of Fe and the subsequent deposition of Fe is studied *in-situ* using x-ray absorption spectroscopy.

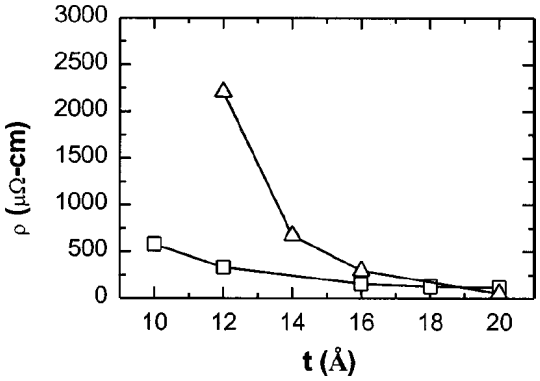

Figure 4.3: Room-temperature resistivity of $(Co_{50}Fe_{50}(t)/oxide)_N$ (square) and $(Fe(t)/oxide)_N$ (triangle) multilayers where t is varied while N is adjusted to keep the total nominal metal thickness at 20 nm. As indicative value, Fe has a bulk resistivity of $10^{-3}\mu\Omega$/cm. Reproduced from [1].

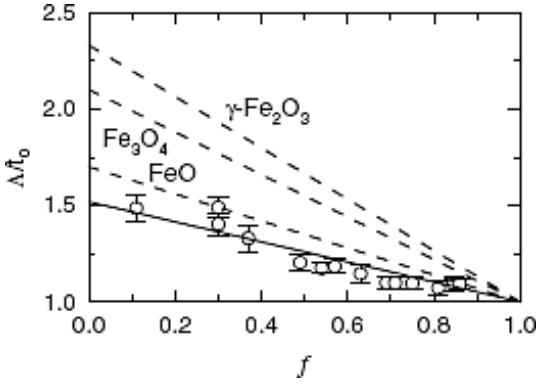

Figure 4.4: Evolution of the expansion of an Fe/native-oxide multilayer (due to the oxidation) as a function of the metal fraction f in the layer system. The solid line is the native oxide multilayers. The expansion is smaller than it would be for any bulk iron oxide phase. Reproduced from [3].

4.3 The unusual properties of buried oxides

A pioneering work on buried native iron oxide layers has been carried out by Beach *et al.*. Most of the findings are summarized in two publications [1, 2] which dealt with the static and dynamic magnetic properties of Co-Fe/native-oxide multilayers. The original idea was to incorporate a nanometer thick oxide layer in its metal parent to form a metal/native-oxide multilayer (MNOM) which combines a high net magnetization with soft magnetic properties and a low conductivity. Beach *et al.* showed that such structure could efficiently prevent the formation of eddy currents while exposed to high frequency magnetic fields in the gigahertz regime. The use of magnetically ordered oxide as insulating layer significantly increases the resistivity compared to the pure metal layer, as shown in Fig. 4.3. They showed that this increased resistivity do not compromise the net magnetization, and therefore the signal to noise ratio.

In the course of their study, it turned out that most of the particular properties of MNOM structures are due to the magnetic and electrical properties of the thin buried oxide. In particular, a detailed study of a buried Fe-oxide layer [3] showed that the structural and magnetic properties of the oxide formed drastically differs from any bulk iron oxide:

The buried oxide has a higher density than any bulk iron oxide. Fig. 4.4 shows the total expansion of an Fe/native oxide multilayers due to the oxidation of the

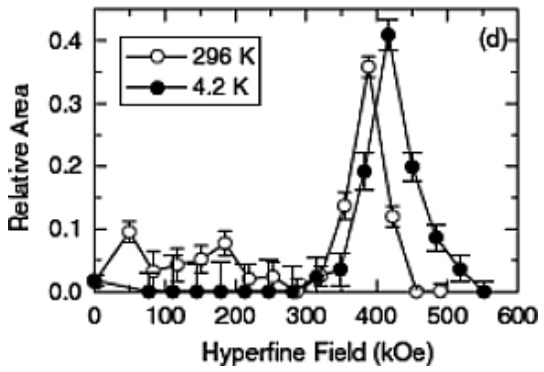

Figure 4.5: Hyperfine field distribution of the native oxide at 4.2 K and 296 K, as derived from CEMS measurement by Beach *et al.*. Figure reproduced from [3].

metal, as a function of the metal fraction. One can see that the expansion is smaller than it would be for any bulk iron oxide phases. This therefore indicates that the density of the buried native oxide layer is higher than any other bulk oxide.

In addition, conversion electron Mössbauer (CEMS) and SQUID measurements indicated that the buried oxide is indeed magnetically ordered and possess a larger magnetic moment per atom than any bulk iron oxide phase. As shown on Fig. 4.5, analysis of the CEMS spectra showed that the oxide was composed of a minor (30%) component with small hyperfine field B_{hf} and a major (70%) component with B_{hf} around 40 T. This latter part carries entirely the magnetic moment.

These puzzling findings triggered the present work. Because all the work of Beach *et al.* where *ex-situ* studies, they were not able to relate the composition of the free native oxide to the buried case. While they unraveled a particular magnetic order of the buried oxide surrounded by its metal parent, they did not consider possible magnetic coupling phenomena between adjacent layers. The present study was devoted to resolve these questions.

Chapter 5

Structural properties of the sample

Prior to the investigation of the magnetic structure of Fe/native-oxide multilayers, it is necessary to have a good understanding of the overall structure of the sample. In particular, it is important to see how the oxidation processes described in chapter 4 will influence the structure of the multilayer.

In this chapter, the sample preparation method is described. Details are given on the resulting structural depth profile of the multilayers.

5.1 Preparation of Fe/native-oxide multilayers

There exist several ways to prepare metal/oxide multilayers. One can cite for example the reactive deposition technique. In the case of sputter deposition, it is based on the sputtering of a pure metal target using a gas mixture (in this case Ar/O). By changing the mixing ratio of the gas, one can deposit oxide layers having different stoichiometry [63]. However this technique presents several drawbacks. Because of the reactive sputtering, the target itself oxidizes, resulting in changing sputtering parameters. For the case of the growth of a metal/oxide multilayer, the introduction of gas mixture incorporating oxygen will result in a partial oxidation of the metal surface prior to the oxide deposition. These effects render the precise control of the growth process difficult, particularly for the growth of ultrathin oxide layers.

The growth of native oxides on the other hand, renders the preparation procedure fairly easy. One can precisely control the amount of metal oxidized by calculating the total exposure to oxygen. This technique has the advantage of being highly reproducible as well as being easy to perform. As discussed in the previous chapter, the main problem resides in the disordered oxide growth, in the sense that the stoichiometry of the oxide cannot be easily controlled *a priori*.

The deposition setup used for the sample preparation is described in **PAPER I**. In the course of this thesis, the deposition has been made completely computer controlled (see Appendix A for details). This allows to perform *in-situ* experiments

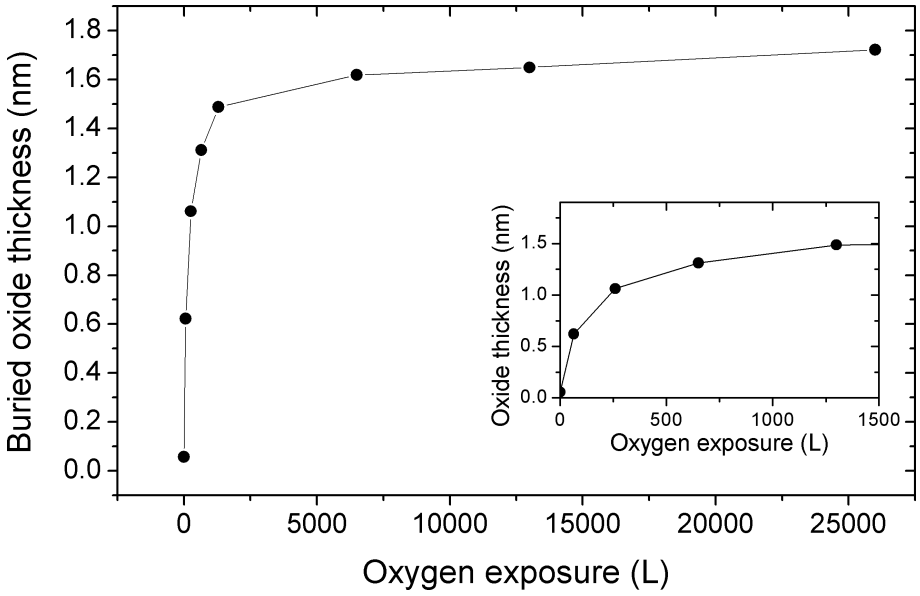

Figure 5.1: Evolution of the buried oxide thickness as a function of the original oxygen exposure. These values are extrapolated from the total oxygen uptake of the layer (determined by *in-situ* XAS) and assuming the FeO density. The inset shows the early oxidation stage in more detail. The data were taken in the same experiment as described in **Paper III**.

with a very good control of the growth parameters.

The usual procedure for the sample preparation is first to deposit an Fe layer of defined thickness (usually 2 to 3 nm) on a superpolished Si(100) substrate. The layers are deposited by DC magnetron sputtering in an Ar gas (purity 99.9999%) with a partial pressure of 5×10^{-3} mbar. The Fe is then subsequently exposed to a defined amount of molecular oxygen. This is achieved by selecting an oxygen partial pressure of 5×10^{-5} mbar and integrating the measured pressure over time (= the exposure) in order to achieve the desired exposure. One can control the thickness of the oxide layer grown by choosing the correct exposure, as shown on Fig. 5.1. The values given in the figure are estimation based on the measure of the quantity of oxygen atoms present in the layer and assuming the bulk density of FeO. The total oxygen present in the layer was determined by *in-situ* x-ray absorption spectroscopy, in a similar experiment as described in **Paper III**. The number of incorporated oxygen atom is estimated from the proportion of oxide in the layer (of known initial thickness) at the given exposure. For the sample preparation, an exposure of 6500 L is generally chosen, which is well into the saturation regime. Being in saturation presents several advantages. It is the way to create the thickest native oxide layer at room temperature. Additionally, the thickness of the layer is much less dependent on the initial parameters of pressure and exposure, increasing the reproducibility and the thickness uniformity in the multilayer.

The next metal layer is deposited once the background pressure in the chamber

falls below a predefined value, which was usually set to 2×10^{-8} mbar. This sequence is then repeated several times to grow a superlattice.

Because the multilayers are produced by controlled oxidation of a relatively thin metal layer, it is important to check that creating a superlattice preserves the multilayer structure. In particular the quality of the interfaces can affect the magnetic properties of the system. These parameters are easily accessed by x-ray reflectivity measurements, which allow one to extract the density depth profile of the multilayer. These experiments were carried out at the W1 beamline of the DORIS III storage ring (Hamburg, Germany) were the energy of the incoming x-ray beam was set to 9.8 keV. The reflectivity curve of a sample with nominal structure Si/[Fe(2.5nm)/O(6500 L)]$_{15}$/Al(3nm) is displayed on Fig. 5.2. This sample contains oxide layers grown by exposure up to saturation, and is therefore representative of the samples studied in this work. The non-appearance of the second order Bragg peak is a sensitive signature that both metal and oxide layer have similar thickness, which is found to be 1.8 nm and 1.7 nm respectively. One can note the good agreement with the expected layer thickness based on density and oxygen uptake calculation presented in Fig. 5.1. The density depth profile indicates that the boundaries between the layers are sharp and well defined. However the root mean square (RMS) interface roughness increases from 0.4 nm at the bottom to 0.7 nm for the top layer. One can also see that the first Fe layer has a slightly smaller density, probably due to partial oxidation at the SiO_2/Fe interface.

5.2 Layer integrated magnetic properties

The preparation procedure described above was applied to the preparation of all the samples studied in this work. For nuclear resonant scattering experiment, ^{57}Fe probe layers were deposited at selected positions within the layer structure. As described in **Paper I**, these layers are deposited in oblique incidence with respect to the sample surface. This has several implications for the homogeneity and the magnetic properties of the sample, which are discussed here.

The thickness uniformity of such layer was determined by x-ray reflectivity along the wedge at different position on the sample. Over the 20 mm of the sample, the layer thickness is doubled. This means in the case of a superlattice where nominally 0.6 nm thick ^{57}Fe probe layers are embedded a thickness variation of $\pm$0.2 nm at the edges (compared to the center).

The oblique incidence has also some consequences regarding the magnetic properties of the layer system. In fact it is known that such deposition conditions result in the growth of elongated grains along the direction from where the particles are impinging, inducing a preferred magnetic orientation [64, 65]. This shape anisotropy of the grains leads to a strong uniaxial magnetic anisotropy of the films. Fig. 5.3 displays the low field hysteresis curve of a Si/[Fe(2.5nm)/O(6500 L)]$_{15}$/Al(3nm) multilayer, as recorded by Magneto-Optical Kerr Effect (MOKE) magnetometry. The presence of well defined *easy* and *hard* axis of magnetization relates to the

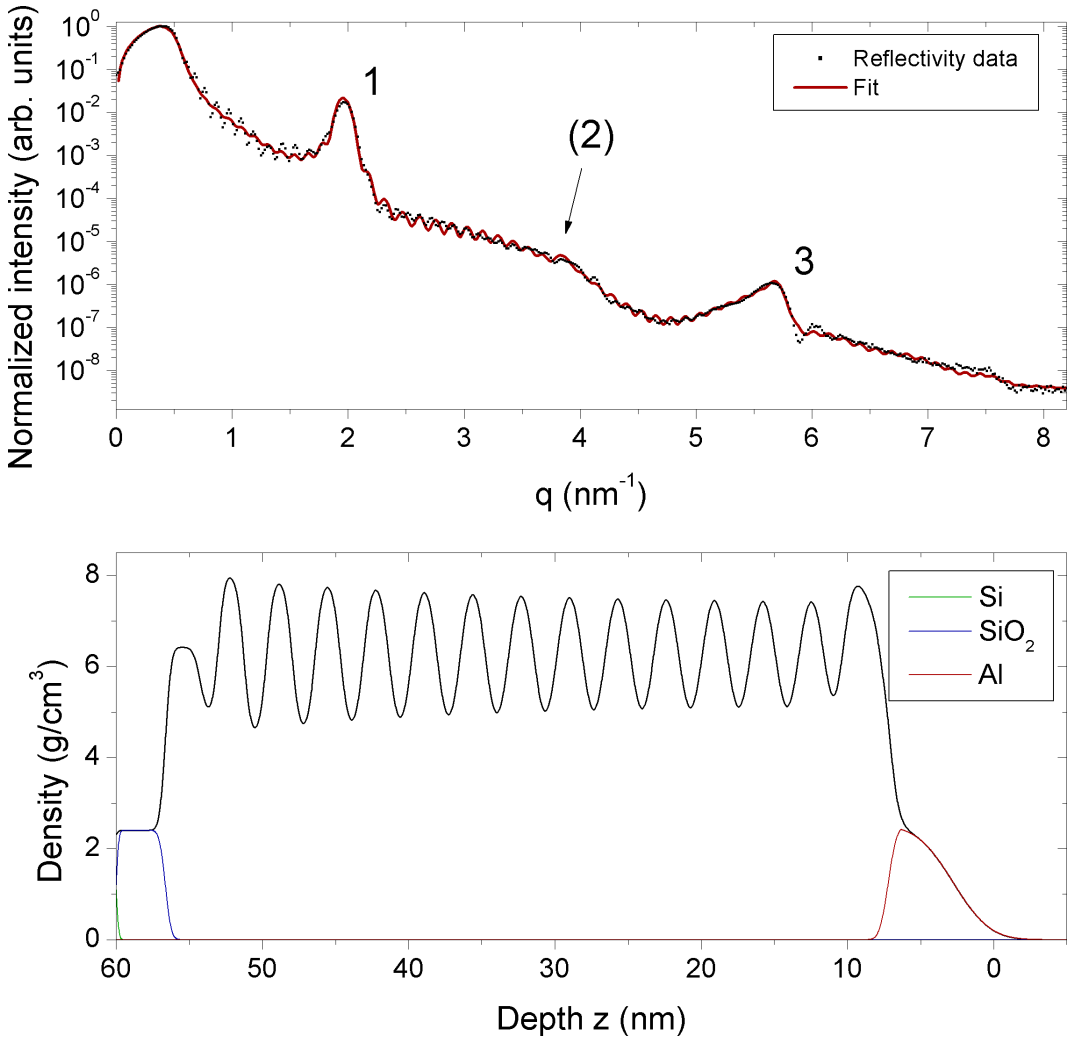

Figure 5.2: Upper panel: X-ray reflectivity curve of a Si/[Fe(2.5nm)/O(6500 L)]$_{15}$/Al(3nm) multilayer recorded at 9.8 keV. Only odd-order Bragg peaks are present, indicating that both metal and oxide layer have equal thickness. The arrow indicates the position where a second order peak would have appeared. Lower panel: Density depth profile, as derived from the simulation of the reflectivity curve.

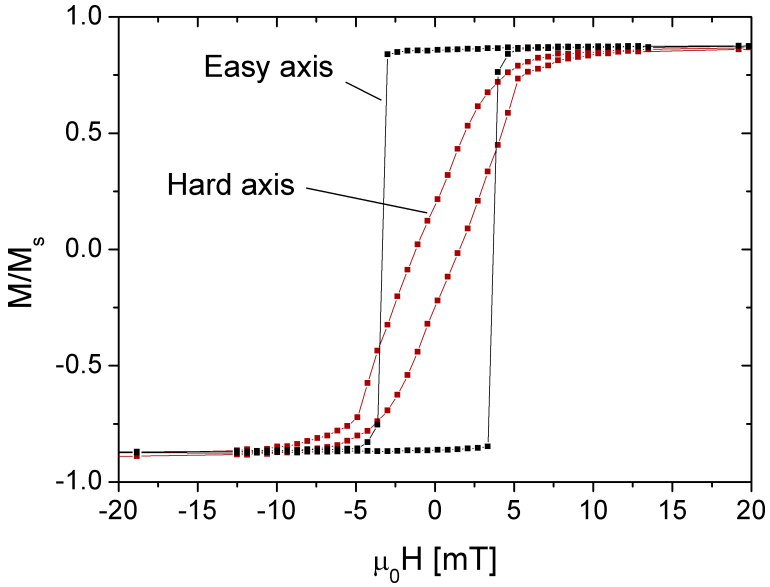

Figure 5.3: Hysteresis curve of a Si/[Fe(2.5nm)/O(6500 L)]$_{15}$/Al(3nm) multilayer which incorporates 0.6 nm thick ^{57}Fe probe layers, as recorded by MOKE magnetometry. A strong uniaxial anisotropy is observed, with the easy axis direction parallel to the deposition direction of the ^{57}Fe layers.

uniaxial anisotropy induced by the oblique deposition. The *easy* axis is parallel to the projection of the deposition direction onto the sample surface. It is interesting to note that even if the ^{57}Fe constitutes only a fraction (in this case 25%) of the total Fe content, its growth conditions lead to the uniaxial anisotropy of the complete system. This oblique deposition could therefore be used as a general method to introduce uniaxial anisotropy in magnetic thin films or multilayers. The hysteresis curve shown in Fig. 5.3 displays a coercive field H_c of 3 mT. This small value confirms the soft magnetic properties of the system.

Chapter 6

Magnetic coupling in Fe/Fe-oxide superlattices

As discussed in the last part of chapter 4, Beach *et al.* have reported that the buried oxide present in Fe/native-oxide multilayers is magnetically ordered. However, they did not consider the possible long range magnetic coupling that could form in such structure between the layers. To obtain a layer selective magnetic signal, *in-situ* and *ex-situ* nuclear resonant scattering experiments were carried out, where isotopic probe layers are used. The complete depth profile of the magnetic structure was resolved by a combination of NFS and PNR on multilayered samples. These results are presented in **Paper II** and **Paper IV**. In this chapter, the results are summarized, complemented with additional experimental findings and discussed in the framework of the model developed in the articles.

6.1 Appearance of interlayer magnetic coupling

This section summarizes the results concerning the appearance of interlayer magnetic coupling between the metal layers in Fe/native-oxide multilayers. These results were mainly obtained by *in-situ* nuclear resonant scattering.

Noncollinear coupling of iron layers through native iron oxide spacers[1]

The aim of the experiment was to study *in-situ* the evolution of the magnetic structure of the metal part of an Fe/native-oxide multilayer during growth using nuclear resonant scattering from ^{57}Fe probe layers. The experiment was carried out in the UHV deposition setup described in **Paper I** at the ID18 beamline of the ESRF. To probe selectively the metal part of the sample, a 0.6 nm thick ^{57}Fe probe layer was embedded in the middle of ^{56}Fe layers (depleted in ^{57}Fe). The use

[1]Summary of **Paper II**: Th. Diederich, S. Couet, R. Röhlsberger, Phys. Rev. B **76**, 054401 (2007)

of ^{56}Fe ensures that the signal will originate only from the ^{57}Fe probe, as natural Fe contains 2.1% of ^{57}Fe. A ^{56}Fe/^{57}Fe/^{56}Fe trilayer will further be referred to as a doped (^{dop}Fe) layer. The magnetization direction was defined by a permanent magnetic field of 70 mT applied in the plane of the sample and parallel to the incoming photon wavevector. What is observed is that upon deposition of the second Fe layer (to form a ^{dop}Fe/^{56}Fe-oxide/^{dop}Fe trilayer), the magnetization of the two metal layers is not collinear anymore but adopts a canting angle of 60°, keeping the net magnetization parallel to the external field.

In the article, it is shown that the magnetic structure is persistent upon deposition of many bilayers to create a superlattice. In this case, the non collinear arrangement manifests as superstructure (half-order) Bragg peak in the nuclear reflectivity curve. As discussed in section 3.3, the intensity of this half-order peak is determined by the difference in the projections of the magnetic moments in the two magnetic sublattices along $\vec{k_0}$. The intensity of this peak was monitored to measure the canting angle as a function of the external field. In high magnetic fields, only an asymptotic decrease of the angle is observed. This behavior could only be reproduced using the proximity magnetism interlayer coupling model of Slonzcewski described in chapter 2.

These results were the first proof of interlayer exchange coupling between metallic Fe layers separated by a native oxide spacer. According to the proximity magnetism model, this coupling should be mediated by an antiferromagnetic oxide spacer layer. This finding has important implications regarding the chemical and magnetic structure of the buried oxide, which will be discussed in chapter 7.

In the following section, the evolution of the magnetic coupling upon deposition of an increasing number of layers is explained in detail.

Evolution of the magnetic structure

In **Paper II**, the study concentrates on a trilayer system and to the discovery of the interlayer coupling. It is interesting to observe how the magnetic structure evolves when growing an increasing number of layers. This situation is summarized in Fig. 6.1. The two upper timespectra correspond to the results discussed in **Paper II**, the lower panels corresponds to the subsequent deposition of a third and fourth metal layer. Careful analysis of the timespectra shows that at the third step, the canting angle increases up to 90° while the net magnetization stays parallel to the external field. Upon deposition of the fourth layer, the system becomes symmetric around the external field with an effective canting angle of 60°.

It is quite surprising to see that the canting angle increased with deposition of the third layer. According to the proximity magnetism model, the coupling angle is only determined by the proportion of FM and AFM coupling between the two adjacent metal layers. This situation should not change once the layers are deposited. However one should take into account that this deposition step corresponds to the first appearance of a "buried" metal layer, *i.e.* the middle metal layer has exchange coupling boundary conditions on both of its interfaces. At this

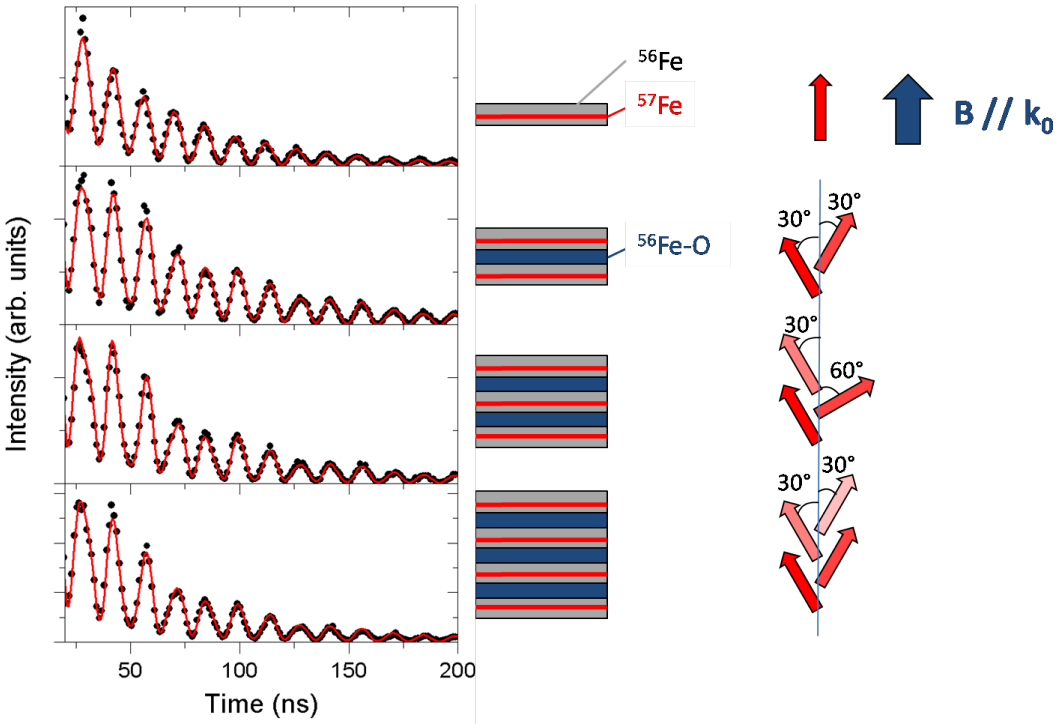

Figure 6.1: Time spectra of *in-situ* nuclear resonant scattering where metal/oxide bilayers are stepwise deposited to follow the evolution of the magnetic structure. The red lines in the timespectra are fits.

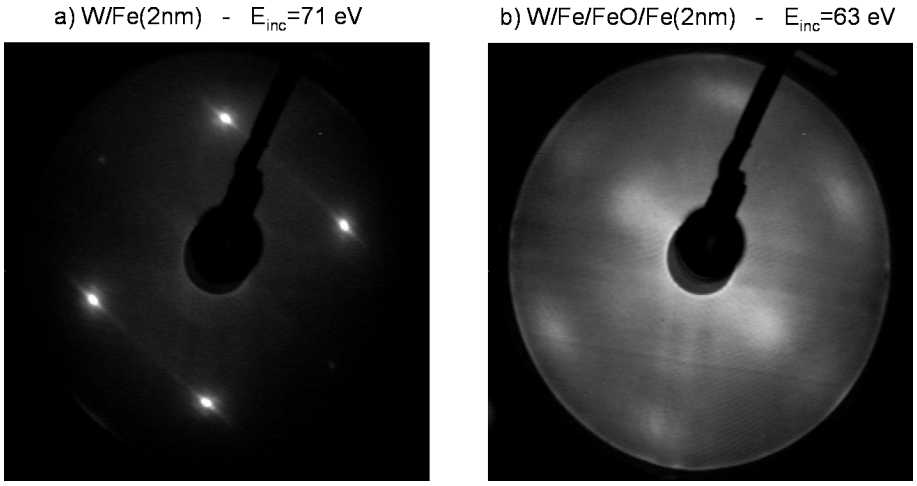

Figure 6.2: Low energy electron diffraction pattern recorded on (a) W/Fe(2nm) and (b) W/Fe/FeO/Fe(2nm). The disappearance of diffraction spot in the trilayers indicates a decrease of the cristallinity of the top layer.

stage, the magnetic structure of the system is not symmetric. This might lead to the adoption of a larger canting angle in order to counterbalance the magnetic moment created by the two outermost layers and align the net magnetization along with the external field. Upon deposition of the fourth layer, the system becomes symmetric again and the coupled spins arrange symmetrically around the net magnetization.

6.2 Magnetic coupling in an epitaxial system

A similar *in-situ* experiment was carried out on epitaxially grown layers, which present a magneto-crystalline uniaxial anisotropy (*cf.* section 2.3). The experiment was carried out in a dedicated UHV system permanently installed at the ID18 beamline [40]. The Fe layers were deposited from an electron beam evaporator. The substrate was a flat W(110) single crystal which was cleaned by numerous cycles of annealing to 1500 K in an oxygen partial pressure of 1×10^{-7} mbar and flash annealed to 2100 K. Such treatment results in a clean and well ordered surface [66]. A 0.8 nm thick ^{57}Fe probe layer was embedded in the middle of a 2 nm ^{56}Fe layer (resulting in a ^{dop}Fe layer). The crystallinity was checked by low energy electron diffraction (LEED), as shown on Fig. 6.2a. The four bright spots account for the cubic symmetry of the surface. The high signal to noise ratio documents a well ordered single crystalline surface. At this stage, the nuclear timespectrum (Fig. 6.3) shows that the magnetization is parallel to $\vec{k_0}$, and therefore parallel to the (110) orientation. This layer was subsequently oxidized to 6500 L, covered by 2 nm of ^{56}Fe and another 0.8 nm ^{57}Fe probe layer. The corresponding LEED pattern (Fig. 6.2b) shows very faint structures, indicating that the top Fe layer is either polycrystalline, or has at least a highly distorted crystal structure. The

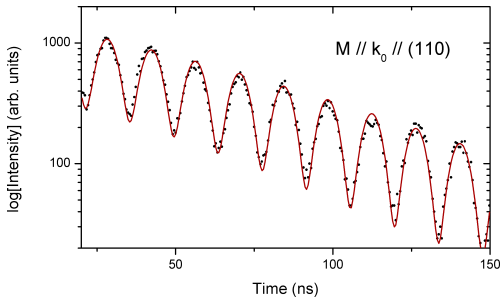

Figure 6.3: Nuclear resonant timespectrum of an epitaxial 2 nm thick doped Fe layer deposited on W(110) substrate. The simulation reveals an orientation of the magnetization parallel to $\vec{k_0}$, proving the uniaxial anisotropy of the deposited layer.

corresponding timespectrum is shown on Fig. 6.4c. The overall shape of the beating pattern changed, indicating that at least the magnetization of the top layer should have different orientation. Timespectra were recorded at three different incident angles on two different orientations of the sample with respect to $\vec{k_0}$. Variation of the incident angle allows one to vary the probing depth, and hence increase the signal originating from one or the other probe layer. This is illustrated in panels i-j of Fig. 6.4. The wavefield intensity at the position of the two probe layers varies drastically for the different incidence angles. Performing these measurements along two different orientations of the sample allows one to unambiguously determine the magnetization orientation of each layer. A consistent fitting of the six timespectra is shown on Fig. 6.4. The fit results indicate that the magnetic moments in both Fe layers are canted by an angle of 45 degree with the bottom layer still aligned along the (110) direction.

This is an interesting result in contrast to the one obtained on polycrystalline films. In that case a magnetic field was applied during the growth. The result is a canting of the magnetic moments symmetrically around the external magnetic field. For the epitaxial layer, there is no magnetic field applied but an uniaxial anisotropy in the bottom layer. Because of the subsequent oxidation, it is expected that the top layer is not single crystalline (see the degradation of the LEED pattern in Fig. 6.2b), and should therefore yield no or smaller uniaxial anisotropy. In this case, the orientation of the bottom layer is fixed by the uniaxial anisotropy and the top layer's magnetization is only determined by the coupling to the bottom layer.

The reduced canting angle could be due to two effects, which could not be verified. One possibility would be that the oxide's structure is much different compared to the polycrystalline case. As described in **Paper IV**, the possible presence of ferromagnetic pinholes could lead to a departure from the 90 degree coupling angle. On the other hand, the second ^{57}Fe probe layer was here placed on top of a 2 nm ^{56}Fe layer. The reduced coupling angle could also be due to the fact that the probe is at the extreme surface of the layer. Because the distance to the oxide/Fe interface is rather large, the sensitivity to the interfacial coupling might be reduced.

The fact that a reference pinning layer can be used to set the magnetization of the whole system, together with the robustness of the coupling against the external

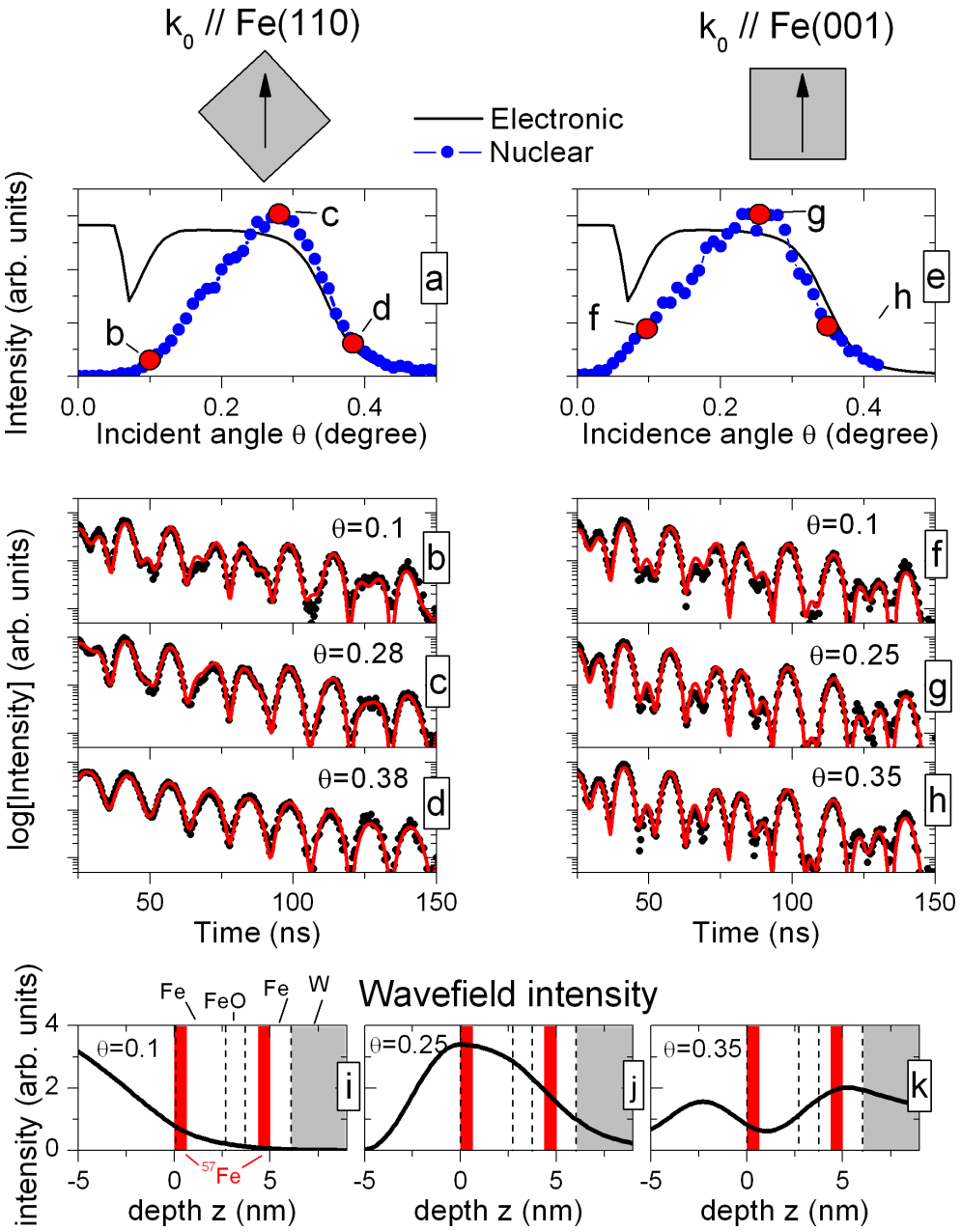

Figure 6.4: *in-situ* nuclear resonant scattering experiment on a ^{dop}Fe/Fe-oxide/^{dop}Fe trilayer epitaxially grown on W(110). The top panels are electronic and nuclear reflectivities recorded around the critical edge for (a) $\vec{k_0}$//Fe(110) and (b) $\vec{k_0}$//Fe(001). Timespectra are recorded at different incident angles marked by a red dot. The consistent fitting of all the timespectra indicates in this case a 45° coupling angle. (i-k) displays the calculated wavefield intensity in the depth of the sample for the different incidence angles. From (i) to (k), the sensitivity is shifted from the top layer to the bottom layer, meaning that one can select from which part of the sample the main signal is originating from.

fields, could open interesting possibilities for application in magneto-engineering. This coupling mechanism could for example be used to induce a rotation of the magnetization in a given multilayer magnetic structure, giving more freedom for spin manipulation in devices.

6.3 Magnetic depth profile

Up to now, the study of the magnetic structure was restricted to the metal part of the sample, where a non-collinear magnetic coupling was observed. However, as pointed out by Beach *et al.* [3], the buried native oxide layers are also expected to be magnetically ordered. It is therefore important to be able to study in a layer resolved manner the magnetic structure of the oxide, as well as its interaction with the neighboring metal layers. This was the goal of the study presented in **Paper IV**, which is summarized hereafter.

The magnetic structure of coupled Fe/FeO multilayers revealed by nuclear resonant and neutron scattering methods[2]

This article presents a joint nuclear resonant scattering and polarized neutron reflectometry study carried out on two Fe/native-oxide superlattices where either the metal or the oxide layers were enriched in ^{57}Fe. NRS was used to study the magnetic coupling of the metal layers or the oxide layers independently while PNR was used to obtain the magnetic contrast between adjacent metal/oxide layers. Besides a confirmation by PNR of the above mentioned findings on the occurrence of magnetic coupling of the metal layer, PNR allowed to have a measure of the absolute magnetic moment per atom of each layer. The value for the metal is found to be equal to bulk Fe while the oxide part carries a small net magnetic moment of $0.5\,\mu_B$ per atom. The oxide's magnetization is pointing in the same direction as the net magnetization.

While the canting angle is found to be around 70 degree for the *metal doped* sample[3], a much smaller value is derived for the *oxide doped* sample which shows a reduced canting angle of 40 degree.

According to the proximity magnetism model, statistical variations of the roughness should lead to an equal proportion of ferromagnetic and antiferromagnetic coupling and stabilize a 90 degree coupling angle. However the previous findings show that the system does not behave like a perfect FM/AFM/FM multilayer. The reduced canting, together with the presence of a small magnetic moment in the oxide, indicates that the oxide is not perfectly antiferromagnetic but incorporates a ferromagnetic component.

[2]Summary of **Paper IV**: S. Couet, K. Schlage, Th. Diederich, R. Rüffer, K. Theis-Bröhl, K. Zhernenkov, B. Toperverg, H. Zabel, R. Röhlsberger, New Journal of physics, accepted (2008)

[3]A multilayer where the metal is composed of ^{56}Fe/^{57}Fe/^{56}Fe trilayers

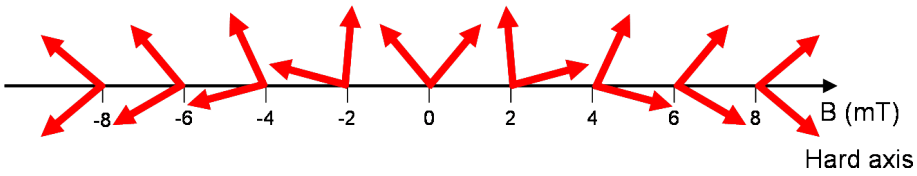

Figure 6.5: Schematic view of the magnetization reversal of a Fe/native-oxide multilayer along the hard axis. The coupled spin system rotates as a rigid unit.

Some oxide phases are ferrimagnetic (and therefore carry a net magnetic moment). Understanding the observed magnetic properties therefore requires a complete characterization of the oxide's structure. This consideration will be discussed in chapter 7.

6.4 Magnetization reversal on the hard axis

The magnetization reversal on the hard axis was studied with NRS and PNR methods (**Paper II** and **IV**), showing that the system does not decay into magnetic domains but rotates coherently as one unit upon magnetization reversal, as illustrated in Fig. 6.5. The absence of domains was confirmed by off specular neutron scattering measurements, which ruled out the presence of magnetic domains smaller than 30 μm. This observation of rigid rotation is quite different from what is observed in conventional metallic multilayer systems. Usually the magnetization reversal is accompanied by phenomena like bulk and surface spin-flop transitions [24], where the canting angle is strongly varying depending on the applied field. In the case of proximity magnetism, the coupling between the two sublattices is strong enough to maintain the spin structure throughout the reversal, as illustrated on Fig. 6.5.

6.5 Exchange bias at low temperature

According to the proximity magnetism model, the buried oxide should be antiferromagnetic at room temperature. This means that the Fe/native-oxide system is composed of a series of FM/AFM interfaces, which are the building blocks leading to exchange bias effects [67]. This phenomenon is usually characterized by an unidirectional magnetic anisotropy which leads to an increase of the coercivity and a shift of the hysteresis loop. Van der Zaag *et al.* [68] have shown that the Néel temperature and the blocking temperature (where the exchange bias transition takes place) are not the same in the case of ultrathin AFM layers. The observation of an exchange bias transition would therefore be an indirect proof of the AFM order of the buried oxide.

This question was investigated on a Si/$[$Fe(2.5 nm)/FeO(6500L)$]_{15}$/Al(3 nm) multilayer by means of low temperature SQUID magnetometry. As shown on Fig. 6.6, the coercivity increases below 60 K, corresponding to the exchange bias

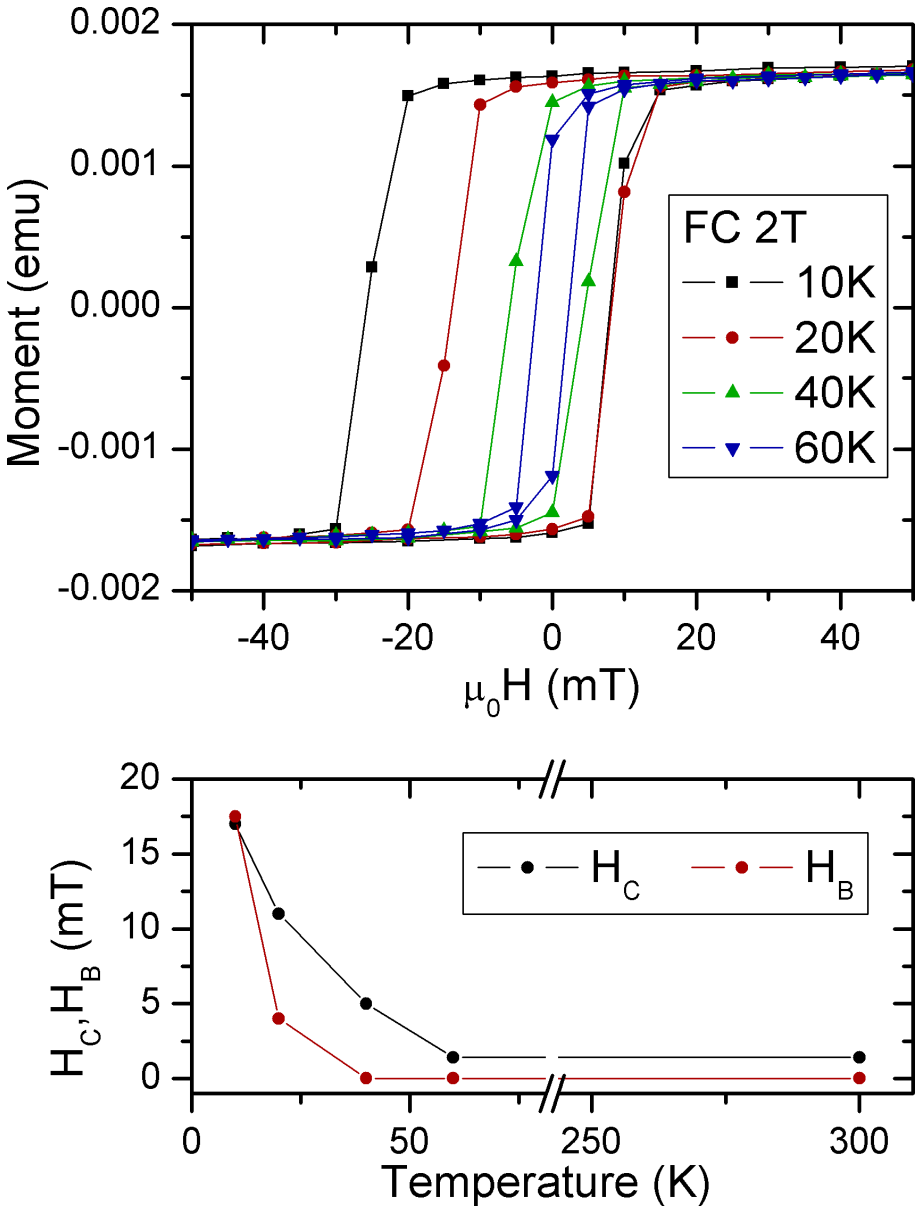

Figure 6.6: Upper panel: SQUID magnetometry curves recorded on a Si/[Fe(2.5 nm)/FeO(6500L)]$_{15}$/Al(3 nm) multilayer. The exchange bias transition occurs at a temperature of 60 K. Lower panel: evolution of the coercive field H_C and bias field H_B with the temperature.

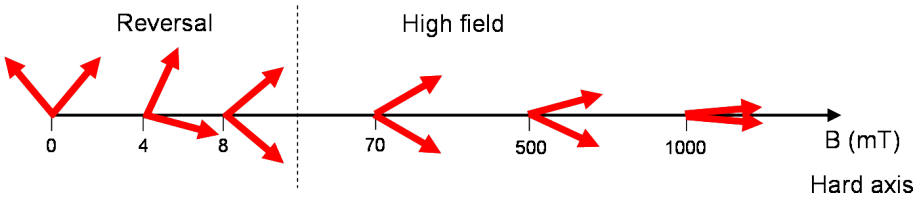

Figure 6.7: Schematic view of the evolution of the coupling from the magnetization reversal up to the saturation field. Note that the horizontal axis is not scaled.

transition. This low blocking temperature is a good support to the argument of AFM order in the buried oxide. According to van der Zaag *et al.*, this low blocking temperature should be accompanied by a larger Néel temperature compared to bulk FeO. This renders the hypothesis of room temperature AFM order possible.

6.6 Conclusions

The appearance of non-collinear magnetic coupling of Fe layers separated by native oxide spacer layers has been observed for the first time. The field dependent study of the canting angle showed that the interlayer coupling can be understood in the framework of the proximity magnetism model, which implies an antiferromagnetically ordered native oxide at room temperature. The evolution of the spin structure in high fields and the magnetization reversal on the hard axis has been studied. The systems stay coupled upon magnetization reversal along the hard axis and the coupling angle vanishes only in magnetic fields higher than one Tesla. The complete spin evolution derived from this investigation is displayed on Fig. 6.7. This emphasize the robustness of the coupling against the external field.

The magnetic depth profile of the multilayer was resolved by a combination of NRS and PNR methods, showing that the buried oxide carries a net magnetic moment. These findings indicate that the oxide does not behave like a perfect antiferromagnet. The occurrence of exchange bias transition at low temperature provides an indirect proof of AFM order. However, the fact that the layer is magnetically ordered at room temperature has still to be investigated. These questions will be discussed in the next chapter.

Chapter 7

In-situ study of the native oxide

The properties of the buried native oxide seem to be completely different from free native oxide layers, which are usually considered as non-magnetic. In this chapter, *in-situ* XAS and NRS studies are presented, which aimed at resolving the chemical and magnetic changes occurring upon transition from the free to the buried oxide.

7.1 How metallic Fe controls the composition of its native oxide[1]

The chemical structure of the native oxide was studied by *in-situ* x-ray absorption spectroscopy at the Fe K-edge (7.1 keV). The experiments were carried out at the A1 beamline of the DORIS III storage ring. The experimental setup is described in **Paper I** while the results of the experiment are given in **Paper III**.

The goal was to study in a quantitative manner the composition of an ultrathin metal layer stepwise exposed to molecular oxygen and to follow the eventual changes occurring upon deposition of Fe metal on top of the free native oxide. This is achieved by analyzing the near edge region (XANES) and comparing it to reference spectra of the different oxide phases, and further analysis of the EXAFS signal.

It is found that the oxidation follows a similar growth behavior as was predicted by the Fromhold-Cook model. However, the site sensitivity of the technique allows one to quantitatively resolve the composition of the oxide. What is seen is that the oxide's composition does never correspond to a stoichiometric bulk oxide. In saturation, a mixture of different Fe^{2+}/Fe^{3+} sites is formed, with apparently no long range order.

Upon deposition of Fe metal on top of the saturated native oxide, the oxide is reduced, leaving only Fe^{2+} sites in the buried oxide. Analysis of the EXAFS signal showed that the buried native oxide has essentially a disordered FeO structure. Additional to these important findings, it is observed that a 10 to 15 % fraction of Fe metal remains unoxidized in the oxide layer. The presence of Fe metal within the

[1]Summary of **Paper III**: S. Couet, K. Schlage, K. Saksl, R. Röhlsberger, Phys. Rev. Lett. **101**, 056101 (2008)

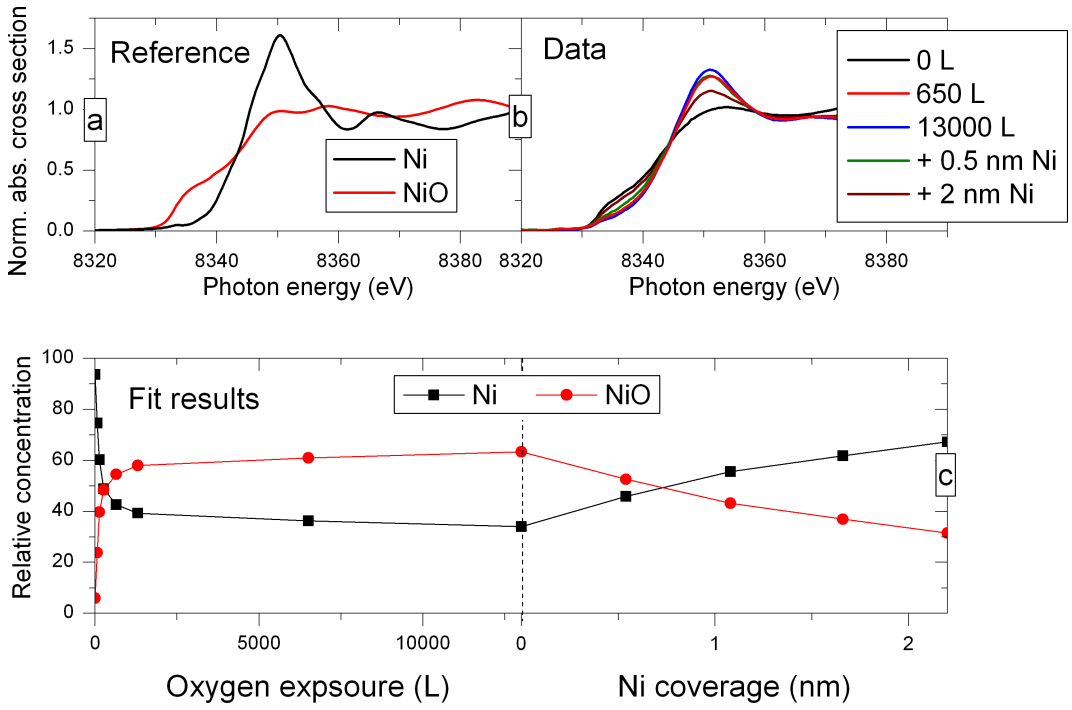

Figure 7.1: Oxidation and deposition experiment carried out on Ni surfaces. a) Reference spectra of Ni and NiO. b) XANES spectra recorded at selected oxidation/reduction steps. c) Results of the fitting procedure.

FeO matrix can eventually account for the small net magnetic moment measured by PNR.

The fact that the buried oxide layer adopts an FeO-like structure rules out the possibility that ferrimagnetic oxide phases are present in the layer. FeO is, however, an antiferromagnet with a Néel temperature T_N of 198 K. The presence of antiferromagnetically ordered FeO at room temperature means that T_N is much increased in the case of the buried oxide. This will be the subject of the *in-situ* NRS study which is presented in section 7.3.

The next section present a similar study as the one presented in **Paper III**, but performed on Ni surfaces. The aim was to test if the results can be generalized to the oxidation of other transition metals.

7.2 Oxidation of Nickel surfaces

The reduction mechanism developed in **Paper III** does not seem to be specific to the case of Fe. The formation of a reduced oxide upon deposition of metal on a native oxide could be a general property of metal/native-oxide systems. Similar XAS experiments were therefore carried out on Nickel surfaces at the Ni K-edge (8.3 keV).

A 1.4 nm thick Ni layer was deposited on a Pd capped Si wafer (the same

substrate as in **Paper III**), stepwise oxidized up to 13000 L and covered with Ni. To obtain quantitative information on the composition of the layer, the experimental XANES spectra were fitted using a linear combination of reference spectra of pure compounds. Two references were used: Ni metal (a thick Ni layer deposited *in-situ*) and NiO (a bulk single crystal). Their XANES spectra are displayed on Fig. 7.1a.

The XANES spectra corresponding to the oxidation of a thin Ni layer and subsequent deposition of Ni are displayed in Fig. 7.1b. The results of the fitting procedure (which gives the relative concentration of the species) are plotted in Fig. 7.1c. One can see that the oxidation proceeds in a similar fashion as for Fe oxidation. First, a fast oxidation rate is observed which quickly saturates above 1300 L. It should be noted that the remaining Ni metal is due to the fact that the initial Ni layer was thicker than what was used in **Paper III** for Fe. One can therefore not conclude here on the eventual presence of Ni metal within the oxide layer. To resolve this effect, additional study with varying initial Ni metal layer thickness are necessary.

It was possible to fit all the experimental data with only the Ni and NiO references, indicating that no higher oxidation state oxide is formed during oxidation. This is confirmed by deposition of Ni on top of the saturated oxide: No drastic changes of the spectra occurs, indicating that only the relative ratio of Ni to NiO is changing. To some extent, the result is not surprising. In contrast to the case of FeO, the NiO phase is very stable at room temperature. In general, the Ni^{3+} state is only rarely observed in compounds or in oxide growth under particular conditions. A Ni^{2+} state is therefore more likely to form also in such oxidation experiment.

Figure 7.2 shows an X-ray reflectivity curve recorded at 9.8 keV on a superlattice with nominal structure $Si/[Ni(3.1\,nm)/O(6500\,L)]_{13}/Pd(6\,nm)$. From the fit of the reflectivity curve, thicknesses of 2.5 nm and 1.5 nm are found for the metal and oxide layers respectively. The thickness of the oxide layer is similar to what forms on Fe. The density depth profile shows an asymmetry between the Ni/NiO and the NiO/Ni interfaces where root mean square roughnesses of 1.2 nm and 0.5 nm are determined. The lower roughness at the NiO/Ni interface might be in direct relation with the fact that no interdiffusion happens upon deposition of Ni on top of the native Ni-oxide. From that perspective, one can imagine that the symmetric interfaces present in Fe/native-oxide multilayers are due to the reduction process that occur when the metal is deposited. One can see the oxide as the oxygen source, which oxidizes the deposited metal. This process would then be to some extent similar to a normal oxidation process, and would lead to similar structural properties for the Fe/FeO and FeO/Fe interfaces.

These findings have important consequences for the appearance of interlayer coupling mediated by proximity magnetism. NiO is an antiferromagnet at room temperature, and proximity magnetism can potentially appear in a Ni/NiO multilayer structure. However, the asymmetry of the interfaces renders the appearance of correlated interlayer coupling over many bilayer less likely (this process partly relies on the assumption that interfaces are of similar kind). Further studies should

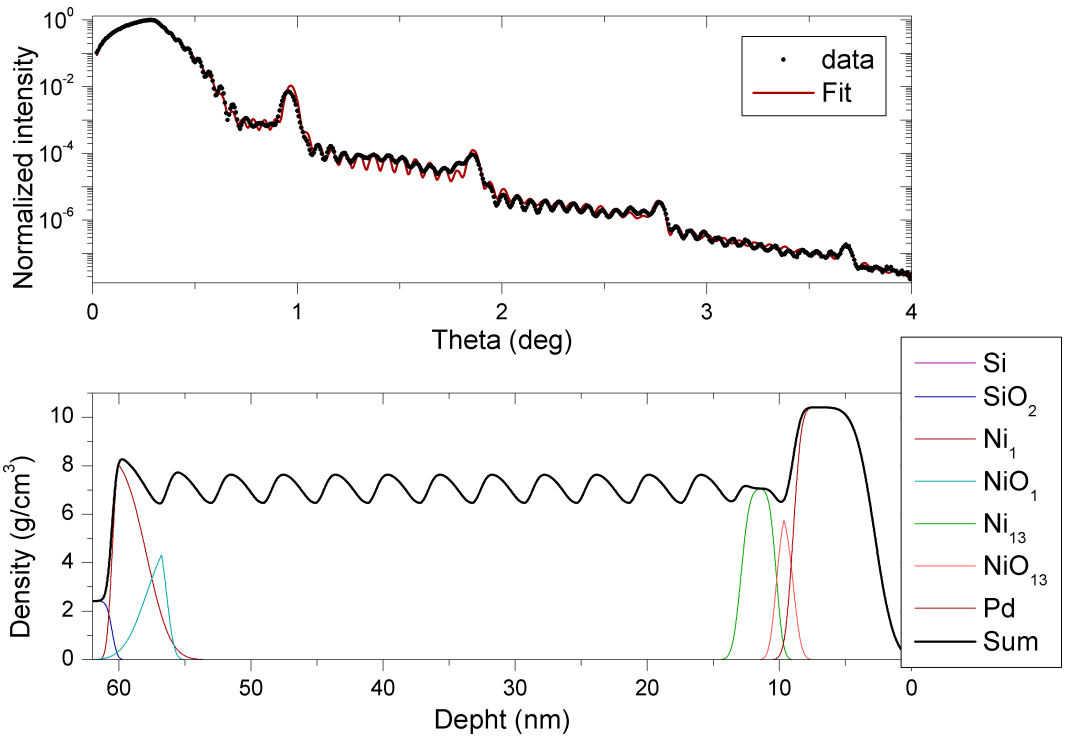

Figure 7.2: X-ray reflectivity curve of a Ni/NiO superlattice (13 bilayers) recorded at 9.8 keV. The density profile extracted from the fit shows an asymmetry between the Ni/NiO and the NiO/Ni interface.

be devoted to this question, as it could provide important answers concerning the occurrence of interlayer coupling in metal/native-oxide multilayers in general.

7.3 Origin of magnetic order

Up to know, the information gathered on the magnetic structure of the buried oxide shows that it should be antiferromagnetic at room temperature, that some net magnetic moment is present, presumably due to the presence of ferromagnetic metal in the AFM matrix. In **Paper III**, it was shown that the native oxide layer reduces to FeO upon deposition of Fe on its free surface. However, one of the main questions remains regarding the stabilization of magnetic order in the buried oxide.

Free native oxide layers are usually considered as non-magnetic. Bulk FeO is also paramagnetic at room temperature. Understanding how the magnetic order appears in the oxide is therefore of importance to understand the stabilization mechanisms that lead to nanometer thick magnetically ordered oxide layers at room temperature.

In that view, *in-situ* nuclear resonant scattering experiments were carried out, where ^{57}Fe probe layers were oxidized and subsequently covered with Fe. The experiment took place at the ID18 beamline of ESRF in the setup described in **Paper I**. In the first experiment (presented in **Paper I**), a 0.6 nm ^{57}Fe probe layer is deposited on top of a 2 nm ^{nat}Fe layer[2]. The corresponding timespectrum shows a beating pattern typical of ferromagnetic α-Fe. After oxidation to 6500 L, the high frequency beating disappears, indicative of a non-magnetic or superparamagnetic state. Upon coverage with Fe metal, magnetic order reappears, but only *progressively*. 2 nm of Fe is required to observe a high frequency beating pattern that indicates a magnetically ordered state. In section 7.1, it was shown that the oxide is completely reduced to FeO as soon as one monolayer of Fe is deposited. From the NRS experiment, one sees that the magnetic order is stabilized only when much more Fe is deposited. This means that the free FeO layer alone is not in itself magnetic at room temperature but requires a magnetic surrounding to stabilize its magnetic structure. It is remarkable that the transition to pure FeO proceeds already after deposition of one atomic layer of Fe, while it needs more than 2 nm to develop pronounced magnetic order.

These results can be put in relationship with the study of van der Zaag *et al.* [68] who showed that the Néel temperature of ultrathin CoO layers sandwiched between Fe_3O_4 layers was increasing compared to bulk CoO as the CoO layer thickness was decreased. For the smallest thickness, the Néel temperature is expected to match the Curie temperature of the surrounding ferro(ferri)magnet. This phenomenon is explained by a mean field model in which the two ordering temperatures (of the FM and AFM) approach each other as a function of the relative thickness of the FM and AFM layer. This implies that in the case that the AFM layer is ultrathin compared to the FM, the corresponding Néel temperature will converge towards

[2] ^{nat}Fe refers to Fe in natural isotopic composition, containing 2% of ^{57}Fe.

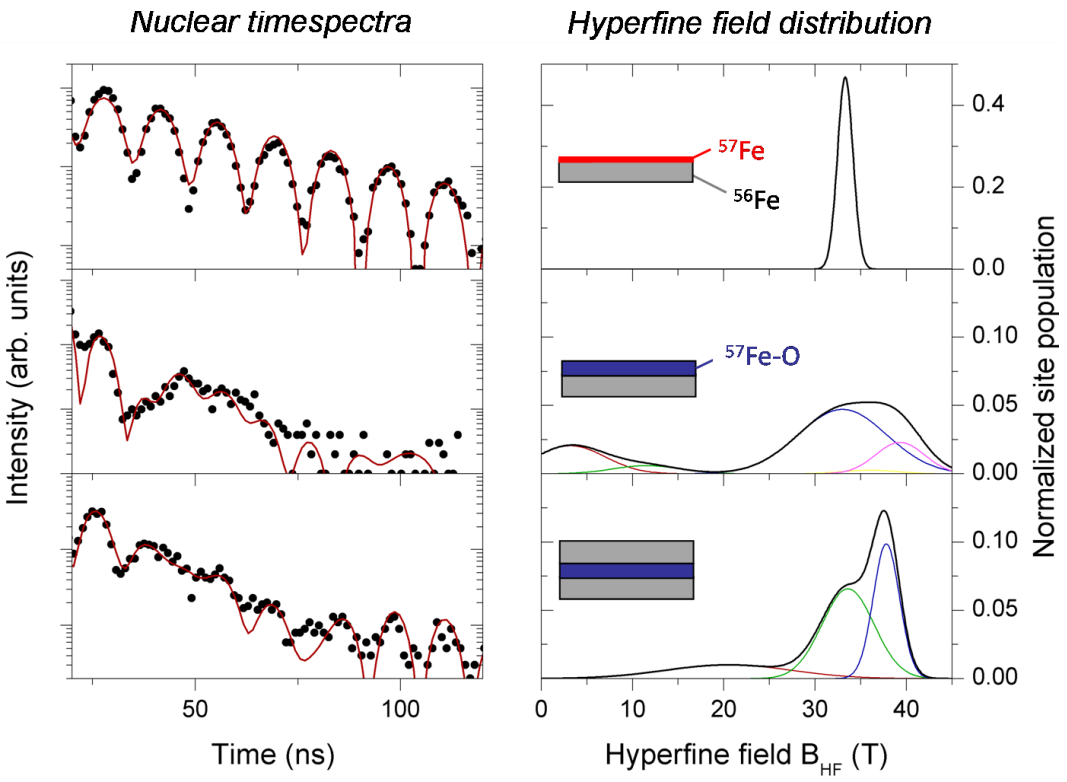

Figure 7.3: *In-situ* nuclear resonant scattering experiment on ^{57}Fe-oxide probe layers. Upper panel: the 0.6 nm thick ^{57}Fe is ferromagnetic and aligned parallel to the external field. Center panel: Oxidation of the probe layer. The high frequency beating disappears. Lower panel: Upon coverage with 2 nm ^{56}Fe, a fast beating reappear, corresponding to hyperfine field components around 33 and 38 T.

the Curie temperature of the surrounding FM. On the other hand, the blocking temperature (where exchange bias transition occurs) is decreasing. This implies that above T_B, the AFM layer is free to rotate upon magnetization reversal. Below T_B the interfacial AFM moments are frozen and an unidirectional anisotropy sets in. The reason for the decrease of T_B eventually lies in a reduced exchange coupling at the FM/AFM interface, compared to the intra-AFM exchange coupling.

These findings match quite well the experimental results obtained here: Magnetism in the thin FeO layer is only stabilized once it is surrounded by its metal parent, effectively increasing its Néel temperature. The fact that exchange bias transition is observed at low temperature supports this argument.

However, the remaining 2% of ^{57}Fe in the metal part of the sample (due to the use of ^{nat}Fe) prevents a precise analysis of the hyperfine field distribution. Therefore, in a subsequent experiment, the ^{nat}Fe target was replaced by an ^{56}Fe target. The hyperfine field distributions extracted from the fit of the timespectra, are shown on Fig. 7.3. After oxidation of the 0.6 nm ^{57}Fe probe layer the fast beating disappears. The resulting hyperfine field distribution shows a broad major

component (around 70 %) centered at 36 T. The remaining hyperfine fields are represented by broad distributions below 10 T. Upon deposition of a 2 nm thick ^{56}Fe layer, a fast beating reappears. Two major components with equivalent relative fraction appear now at 33 T and 38 T, which have significantly narrower distribution as compared to the free native oxide case. The small hyperfine field sites have disappeared, eventually due to the chemical reduction which was observed with XAS. The hyperfine field values can be put in relationship with bulk values of iron oxides. The Fe^{2+} sites like in FeO are usually reported to yield a hyperfine field around 40 T. The value of 38 T found in this study can therefore account for FeO type of site. The slightly smaller hyperfine field can either be due to a surface/interface effect or due to a temperature effect, as normal FeO is normally not magnetically ordered at room temperature. It is interesting to note that there always exists a component centered around 33 T, the value of ferromagnetic Fe metal. This observation supports the interpretation that the Fe metal present in the oxide is ferromagnetically ordered and can be responsible for the measured net magnetic moment of the oxide.

These results can be compared to what was observed by Beach *et al.* in their CEMS study. In fact, they performed the CEMS measurement on Fe/native-oxide multilayers which were not selectively doped with ^{57}Fe (*i.e.* the complete sample was prepared with ^{57}Fe). In order to analyze only the CEMS spectra of the oxide, they systematically subtracted the metal component. This prevented them to observe the metal component also present in the buried oxide. It can therefore be that the high magnetic moment they reported for the buried native oxide was originating from the metal inclusions, and not directly from the Fe^{2+} sites. The determination of the (eventual) net magnetic moment of the Fe^{2+} sites requires further investigations.

7.4 Conclusions

Studying the chemical and magnetic structure of the native oxide *in-situ* brings a deeper understanding of the observed properties of such layer that were observed *ex-situ*. The multicomponent free native oxide reduces to single component FeO upon deposition of Fe on its free surface. Surprisingly, this does not correspond to a magnetic transition. Instead, *in-situ* NRS shows that the oxide layer is magnetically stabilized upon deposition of a 2 nm thick metal layer. The persistence of a 33 T hyperfine field component indicates that the metal present in the oxide is ferromagnetically ordered and can be responsible for the observed net magnetization of the layer.

Chapter 8

Conclusions and perspectives

This work aimed at a better understanding of the magnetic structure of Fe/native-oxide multilayer systems. For that purpose, a series of x-ray and neutron scattering and x-ray spectroscopy experiments were carried out. The use of a dedicated ultra-high vacuum deposition system for *in-situ* studies brought a decisive advantage to study the formation of buried native oxide layers. The combination of nuclear resonant scattering and polarized neutron reflectometry proved to be ideally complementing the layer resolved study of the magnetic structure. In the following, a summary of the main findings is given.

The appearance of non-collinear magnetic coupling was for the first time observed in Fe/native-oxide multilayers. This interlayer coupling is mediated by a proximity magnetism type of interlayer coupling which implies antiferromagnetically ordered oxide spacer. The joint NRS and PNR study evidenced a net magnetization in the oxide layer.

The observation of exchange bias transition at low temperature confirms the antiferromagnetic nature of the buried oxide. However, a clear understanding of the oxide's chemical and magnetic structure required *in-situ* studies of the transition from the free to the buried oxide case.

The chemical structure was studied by *in-situ* x-ray absorption spectroscopy. It was found that the free native oxide is a non stoichiometric mixture of Fe^{2+} and Fe^{3+} type of sites. Upon deposition of Fe, the oxide reduces to an Fe^{2+} containing oxide which adopts a disordered FeO structure. This finding is surprising in many aspects, in particular because FeO is normally the less stable oxide to form in nature. Being able to create in a reproducible manner FeO nanolayers opens new possibilities for the use of this compound. Comparison with the oxidation of Nickel showed that the reduction process has a strong influence on the morphology of the created FeO/Fe interface. From the magnetic point of view, the reduction of the oxide observed in the XAS experiment does not correspond to a magnetic transition. It is necessary that the oxide is surrounded by ferromagnetic material to stabilize the AFM phase.

The *in-situ* experiments also showed that ferromagnetic Fe remains in the oxidized layer. This ferromagnetic part can account for the measured net magnetic

moment of the buried oxide. This phenomenon presumably also leads to the reduced canting angle (60° instead of 90°) usually observed in Fe/FeO multilayers. The origin of this Fe metal is still not clear. In particular it is not clear whether the metal remains in the form of nanocrystals stable against oxidation or metal atoms at grain boundary positions. This effect should be investigated in more detail. In particular one should investigate the possibility to remove these "defect" metal clusters by mild thermal annealing of the multilayer *a posteriori*. This could lead to a pure AFM state in the oxide and larger coupling angle.

Bringing together the consistent results of the *in-situ* and *ex-situ* studies, a deeper understanding of the particular structural and magnetic properties of these systems has been gained. It provides a link between the observed properties of the multilayer with the basic growth process of the buried oxide. This knowledge gives now the opportunity to tune the properties of the multilayer. This thesis therefore lays the foundation for extended study on transition-metal/native-oxide systems. The results presented in this work were obtained on native Fe-oxide layers oxidized up to saturation. The knowledge gained from the XAS experiments however showed that the buried oxide will most probably always present an FeO-like structure. This opens interesting perspective regarding the use of even thinner oxide layers, which would be produced by oxidation with lower exposure. While it is difficult to predict what effects the use of thinner oxide layers would produce, there are some hints that there are still more interesting effects to be expected. As can be seen in Appendix B, the reduction of the native oxide thickness leads to an increase of the coercive of the film which is not monotonic.

Finally, one sees that the number of parameters one can vary when preparing metal/native oxide multilayers, such as oxygen exposure, metal thickness, deposition temperature, is large. This potentially offers the freedom to easily tune the magnetic coupling and/or magnetic properties of the system, which should be investigated. In the upcoming fields of spin electronics, nanometer thick oxide layers are used in tunnel magnetoresistance devices. Having the possibility to create nanometer thick oxide layers by simple oxidation processes would therefore bring an ease of preparation for the industrial development of these technologies.

Appendix A

Computer control of the deposition system

The ultra-high vacuum system used during this doctoral thesis was also developed in order to render the deposition process fully automatized, as described in **paper I**. One of the main tasks was to develop the necessary electronic for the control of each individual instruments, as well as the corresponding control software. This chapter reviews the details of these developments, with the purpose to help future users of this system.

A.1 Description of the computer controlled equipment

In order to computer control the deposition process several instruments have to be remotely operated. Namely two sputter sources and their corresponding shutters, a mass flow controller for Argon gas and a step motor driven leak valve for the admission of low pressure gases. These different devices are all controlled via different interfaces (which will be described hereafter). The scheme applied was to use a general purpose USB protocol to control the system via a laptop computer. All the necessary electronics to convert the different signals to USB protocol are combined in an electronic box. A USB HUB is present to connect each separate apparatus and a single USB cable is finally needed to connect to the computer. In the following, the different controls available for each instrument are described together with their converter to USB protocol.

Sputter sources

The sputter guns are controlled by MDX500 power sources from Advanced Energy Industries inc. These power supplies operate in DC mode and therefore enable DC sputtering. The maximum power delivered is 500 W. However the sputter guns MAK 1.3" (from US inc., center source) and AJA A310-XP 1" (AJA international

inc., side sources) support a maximum of 350 W and 125 W, respectively.

The sputter sources are controlled via an analog interface. A 25-pole sub-D connector is present at the back of the control panel to provide the different necessary signals. The pin to pin corresponding signals are summarized in table A.1.

Pin	Name	Type	Description
1	I_{out}	Analog output 0-10 V	Monitoring source parameter: current. 10 V = 1 A.
2	P_{out}	Analog output 0-10 V	Monitoring source parameter: power. 10 V = 500 W.
3	V_{out}	Analog output 0-10 V	Monitoring source parameter: voltage. 10 V = 1000 V.
4	Water interlock	Digital input 0-15 V	Interlock signal watercooling. This signal is physically bridged with pins 5 and 6 in the SUB-D connector of the cables. 15 V = interlock condition satisfied.
5	Vacuum interlock	Digital input 0-15 V	Interlock signal vacuum conditions. This signal is physically bridged with pins 4 and 6 in the SUB-D connector of the cables. 15 V = interlock condition satisfied.
6	Main interlock	Digital input 0-15 V	Main interlock signal. This signal is physically bridged with pins 4 and 5 in the SUB-D connector of the cables. 15 V = interlock condition satisfied.
7	RMT_{OFF}	Digital input 0-15 V	Turn off the output power. It should be used simultaneously with pin 8. 0 V = off.
8	RMT_{ON}	Digital input 0-15 V	Turn on the output power. It should be used simultaneously with pin 7. 0 V = on.
9	Ground	Ground	Ground reference signal(0 V).
10	Reference	10 V reference	This pin provides a 10 V reference voltage.
12	$Level_{out}$	Analog output 0-10 V	Gives the programmed setpoint. Not used in the program. 10 V = maximum setpoint.

13	$Setpt_{OK}$	Digital output 0-15 V	Indicates if the output matches the requested setpoint. 0 V = setpoint reached.
14	V_{ref}	Output 15 V	15 V reference voltage.
16	P_{reg}	Digital input 0-15 V	Select the regulation method in conjunction with pin 17. When P_{reg}=0 V and I_{reg}=15 V, power regulation is selected. If P_{reg}=I_{reg}=0 V, voltage regulation is selected.
17	I_{reg}	Digital input 0-15 V	Select the regulation method in conjunction with pin 17. When I_{reg}=0 V and P_{reg}=15 V, current regulation is selected. If P_{reg}=I_{reg}=0 V, voltage regulation is selected.
20	Ground	Ground	Ground reference signal (0 V).
21	Ground	Ground	Ground reference signal (0 V).
22	$Output_{OK}$	Digital output 0-15 V	Indicator of output power turned on. 15 V=output on.
23	$Level_{in}$	Analog input 0-10 V	Input signal used to program the setpoint of the source. 10 V = maximum setpoint (either 1 A, 500 W or 1000 V).
25	Ground	Ground	Ground reference signal (0 V).

Table A.1: Signal provided by the MDX 500 sputter sources through the 25 pin SUB-D connector situated on the back of the sputter sources.

As can be seen, the control of the sputter sources requires various inputs and outputs of digital and analog signals. These signals will be provided by a multi input/output board miniLAB 1008 from Meilhaus GmbH. This part is a central piece in the control electronic and will be described in the following subsection.

Input/output board

As described in the previous section, a multi purpose input/output board is necessary to merge to an USB protocol all the signals needed for the sputter sources. As will be described later, other devices such as shut off valves or shutters also require digital signals, which will be provided by the same output board.

The front panel of the miniLAB 1008 is shown on Fig. A.1a. It provides 32 screw terminals with different input and output signals. For our requirement, two ME-UBRE (Fig. A.1b) relay boxes are connected to the miniLAB 1008. This is achieved by use of a 37 pole SUB-D connector on the minilab side, which splits into two 15-pole SUB-D connectors for the relay boxes. A single connection from the miniLAB 1008 to the USB HUB is then established.

The system can provide the following signals:

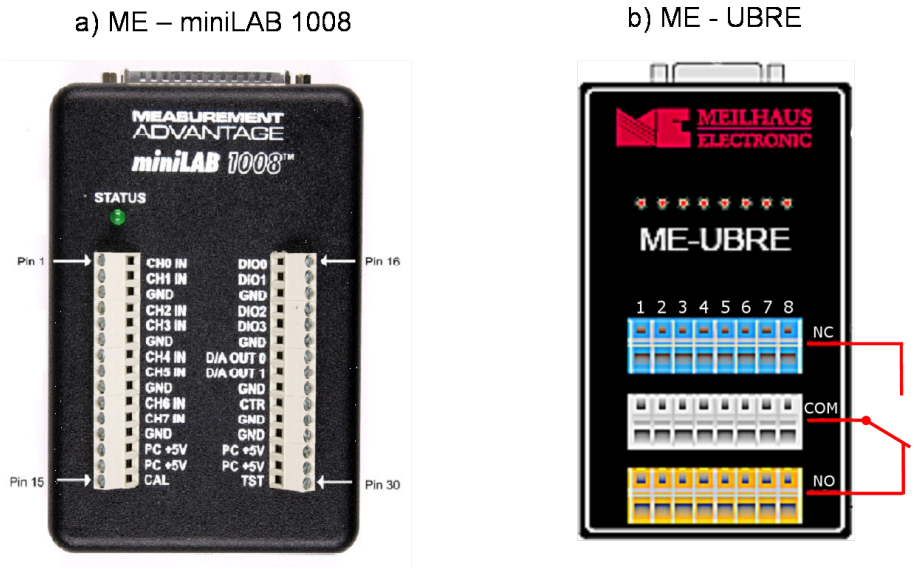

Figure A.1: Front panel of a) the miniLAB 1008 and b) the ME-UBRE relay box.

- 8 analog inputs, 0-10 V, 11 bit resolution.
- 4 Digital input output, 0-5 V, can be configured (via software) as input or output.
- 2 analog output, 0-5 V, 10 bit resolution.
- 16 relay controls via the 2 UBRE boxes.

A complete set of routine for control via LABVIEW are available and will be described in a later section.

Shutters

Motorized shutters are available for each sputter gun. The shutter is actuated via a magnetic coil motor. The opening of the shutters is controlled via relay terminals on the UBRE control box. The applied voltage (which determines the maximum torque the motor can stand) is adjusted via a separate power supply. The following limitations apply for proper operation conditions of the motor:

Max. torque (Ncm)	Voltage (V)	Current (A)	Working time
4.5	12	1.16	unlimited
16	24	2.33	max. 5 minutes
33	36	3.5	max. 3 minutes

Mass flow controller

The sputtering process requires stable argon gas injection with working pressures in the 10^{-3}-10^{-2} mbar range. This is achieved by a mass flow controller EL-flow F201C from Bronkhorst GmbH. It is rated for a maximum flow of 200 sccm (standard cubic centimeter/minute). Practically the pressure achieved in the present vacuum chamber range from 3×10^{-3}-3×10^{-2} mbar. A stable pressure is reached by setting an opening setpoint (between 0 and 100%) for the output valve. The mass flow controller itself is powered by a dedicated control unit. Communication to the computer is achieved using the RS232 protocol. For that purpose, an USB to RS232 converter is present in the main electronic box.

Because a mass flow controller always allows some gas flow, even in the closed position, an electromagnetic shut off valve is placed just behind the mass flow controller. A 24 V signal is provided by a small power supply encapsulated in the mass flow controller power supply box. The valve is actuated using a relay located on the UBRE box.

Oxygen leak valve

For the admission of oxygen (or other gases) at pressure in the range 10^{-8}-10^{-3} mbar, a step motor driven leak valve (VSE vacuum technology) is used. The opening of the valve (or better, position of the step motor) is regulated by an analog input 0-10 V signal. This signal is provided by an USB to analog converter UTA 12 (Elektro-Automatik GmbH) directly connected to the USB HUB. This is controlled using dedicated routines in LABVIEW.

Electronic box

The above mentioned interfaces are all merged in an electronic box which provides a single USB connector for connection to the remote laptop computer. The inner arrangement of the box is shown in Fig. A.2. As can be seen, the different instruments (miniLAB, UBRE, USB to RS232 and UTA 12) are all connected to a USB HUB which provides a single cable output for connection to the computer. Fig. A.2 also shows all the connections to the outside ports. The wiring diagram of the miniLAB 1008 to the SUB-D port of sputter sources is shown on Fig. A.3. This drawing is useful to check which channel number (which will be used in the LABVIEW program) is assigned to which pin of the sputter sources.

With this, all the necessary connections are presented. The last part is therefore dedicated to the description of the software implementation of these solutions.

A.2 Software control

As mentioned in **Paper I**, the system is completely controlled using LABVIEW. Before discussing the general architecture of the control program, a short intro-

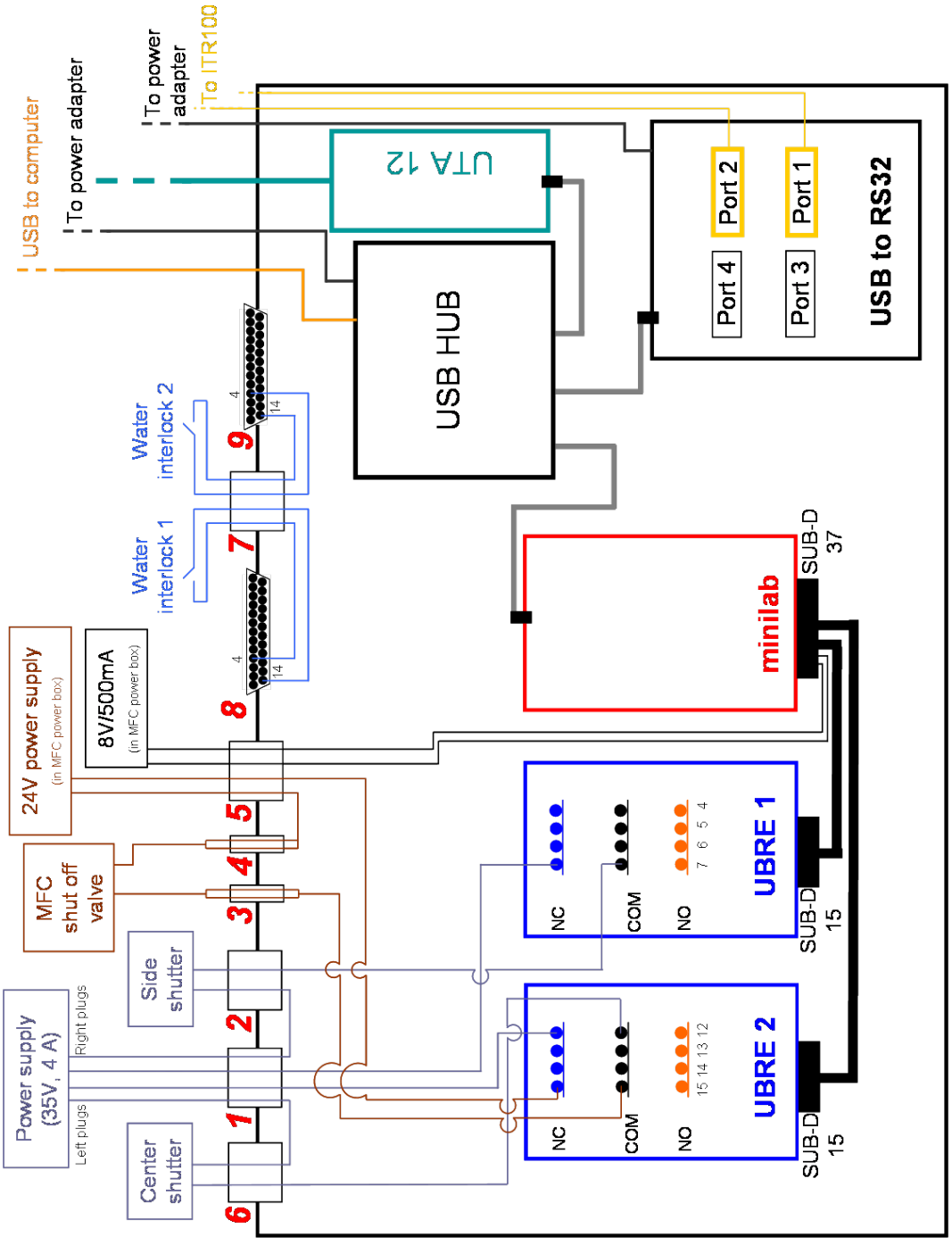

Figure A.2: Schematic diagram of the inner part of the electronic box. The connections from the sputter sources to the miniLAB and the UBRE relay boxes is not drawn for clarity but are drawn separately on Fig. A.3. Only the last four connectors of each UBRE relay box are shown.

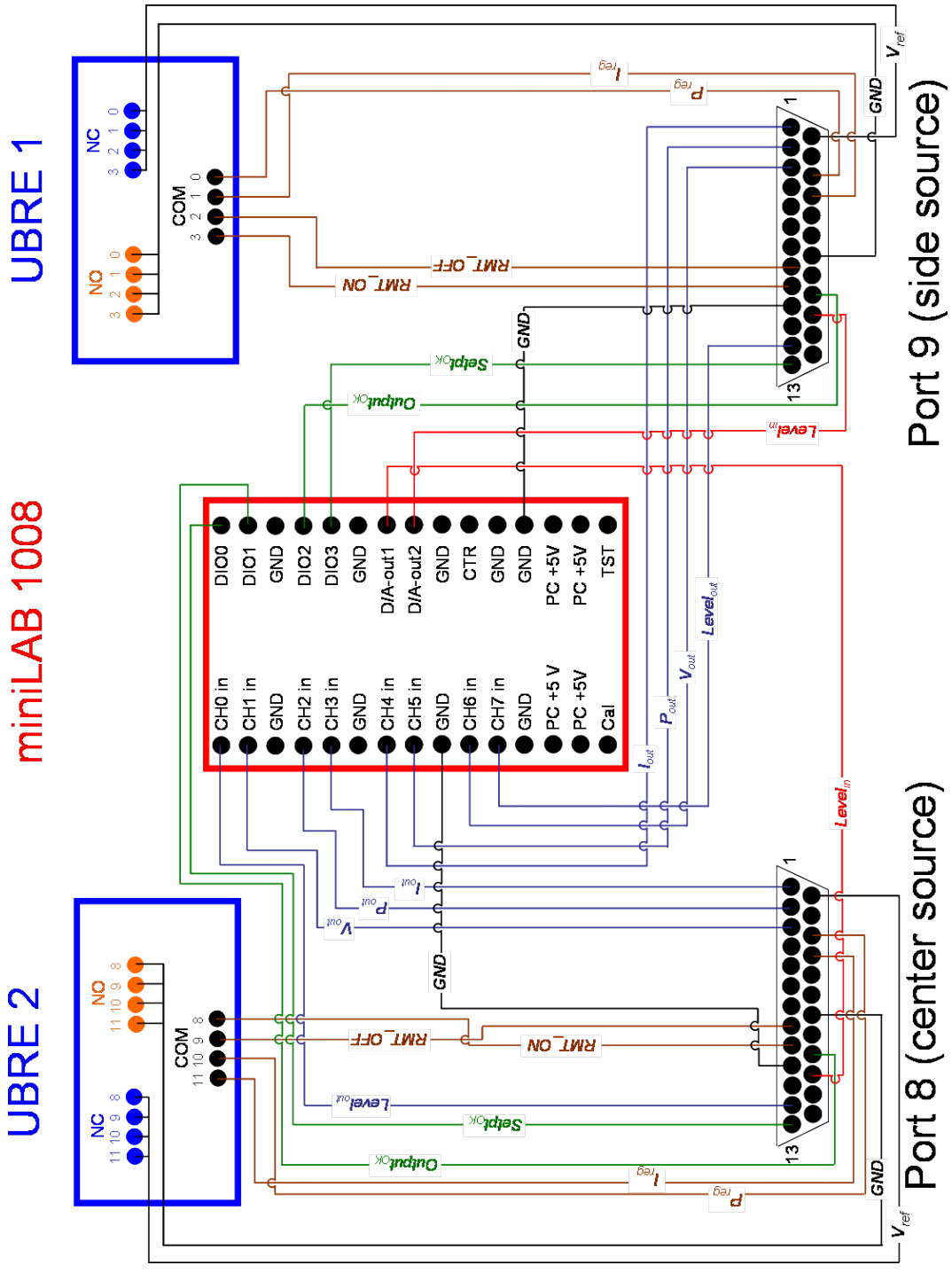

Figure A.3: Wiring diagram of the miniLAB 1008 to the input output SUB-D port of the sputter sources. Only the first four connectors of the UBRE relay boxes are shown.

duction to the particular routine used to control the different interfaces under LABVIEW is given.

miniLAB 1008

The minilLAB 1008 requires several drivers from Meilhaus GmbH to run properly with LABVIEW. A zip package including all the driver can be found on the Meilhaus website[1](170 MB). First the control software *Instacal*, *TracerDac* and *Universal library* should be installed. Once this is done and that the Labview software (National Instruments) is installed, one should additionally install the *Universal library for Labview*[2]. These are routines that provide Labview-type wiring blocks for control of the individual terminals of the miniLAB. Before starting to use Labview, the *Instacal* software should be run once to configure the board if it is a new installation.

Among the many VI's (a LABVIEW block diagram is called a VI) available for control of the unit[3], only a few of them are necessary for the control of the necessary ports.

Analog input

The signal present at any analog input (CH0 in to CH7 in) can be read using the `Ain.vi` routine. The output data then have to be converted to real (double presicion) number using the `Toeng.vi` routine. Because this is always performed together, I wrote a short macro which performs both task in a row, which is called `AInread_redlab(SubVI).vi`. The connector block diagram is shown on Fig. A.4a. As input, one has to provide the board number (which can be found by running the Instacal program), the channel number (0 to 7) and the range (which is always 0-10 V). As output one obtains the data (in Volt) and an eventual error code.

Analog output

For the analog output (mainly used to program the operating setpoint of the sputter source), the situation is a little bit more complicated. Additionally to the board and output channel (from 0 to 1) number, one has to provide the desired set point as a value between 0 and 2048 (the number of channels of the digital to analog converter). In Fig. A.4b the case of power regulation is demonstrated, where the maximum power output is 500 W.

a) AInread_redlab(SubVI).vi

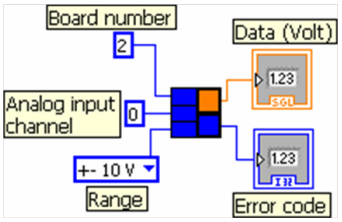

b) A out.vi

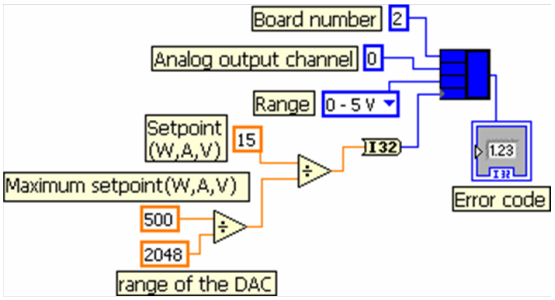

c) Dcfgport.vi

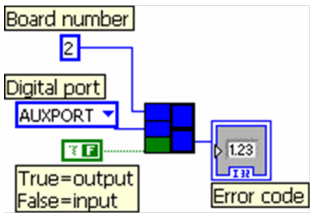

d) Dbit in.vi

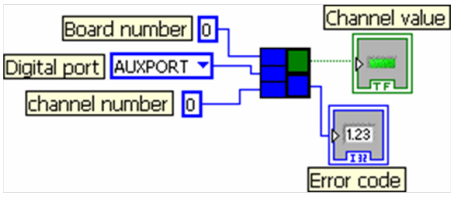

e) Dbit out.vi

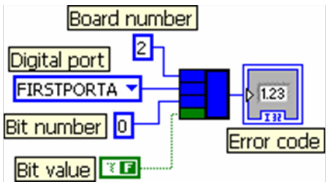

Figure A.4: Labview wiring diagram of the routines used to control the miniLAB 1008 unit.

Digital input output

There are two types of digital ports on the miniLAB1008. The digital input output *channels* directly present on the board constitute one digital *port* which is referred to as the `AUXPORT` port in the routines. The two 8-channel ports of the UBRE relays are labeled as `FIRSTPORTA`. Both have to be configured either as input or output port using the `Dcfgport.vi` routine. Once the port is configured as input (or output), all the individual bits within the ports will be input (or output). The relays (and therefore `FIRSTPORTA`) are configured as output and the `AUXPORT` are inputs which will be used to read the status of the sputter source (Output_{OK} and Setpt_{OK}).

The routine `Dbitin.vi` is used to read the value of an input bit channel. The board number, the port type (`AUXPORT`) as well as the bit number (0 to 3 in this case) have to be provided. In return, the digital bit value is given in the form of a boolean variable.

The routine `Dbitout.vi` is used to set the state of an output bit channel. The board number, the port type (`FIRSTPORTA`), the bit number (0 to 15 in this case) and the bit value (as a boolean) have to provided.

All the mentioned routines enable one to operate the sputtering sources, the shutters and the shut off valve using LABVIEW. The other instruments, however, use different interfaces, the details of which are given hereafter.

Mass flow controller

The power connection to the mass flow controller (MFC) is done using an standard RJ45 cable connected to a dedicated power supply. The interface for connection to the computer is the RS232 protocol. For that reason, an USB to RS232 (USB4COM, Meilhaus GmbH) is implemented in the control box and provides 4 additional COM ports. The MFC is usually plugged in the first port, which is for the moment recognized as COM port 3 under windows.

The mass flow controller (MFC) is controlled using a dedicated program called `FLOWDDE`[4]. This program controls the MFC and acts as a server for other programs like LABVIEW. In this sense, request will be made from LABVIEW to FLOWDDE to operate the MFC. For that reason the FLOWDDE software should be started, and the communication initiated before the LABVIEW software is started.

The DDE (Dynamic Data Exchange) protocol is directly implemented in LABVIEW. The corresponding routines can be used to access the FLOWDDE server. Self made routines are available to easily read and write the MFC setpoint. For

[1] `http://www.meilhaus.org/downloadserver/redlab/RedLab_Web_2_6.zip`

[2] Labview 8 required an updated version of the *Universal libraries* which can be obtained by contacting Meilhaus GmbH, if necessary

[3] For a complete list, see the operation manual SM-UL Labview.pdf provided with the software package.

[4] http://downloads.bronkhorst.com/

further details on data exchange using DDE and its implementation, the reader is referred to the *FLOWDDE* and *DDE under labview* manuals.

Two self made subroutines are used to write and read the setpoint of the MFC: `Setpoint mass flow 3.0.vi` and `Setpoint mass flow read.vi` . The first one takes as input the desired mass flow setpoint (between 1 and 100%) while the second one gives the actual set point as output.

As mentioned previously, the MFC is equipped with a shut off valve which is separately controlled using relays on the UBRE box. The valve requires 24 V to open. This voltage is provided by a small power supply placed inside the MFC control box.

Oxygen leak valve

The opening of the oxygen leak valve is controled by an analog 0 to 10 V signal. This cannot be provided by the miniLAB (which provides maximum 5 V output). An additional USB to analog converter is used, which enables 0 to 10 V signal. Prior to use with LABVIEW, the driver for the UTA12 unit should be installed[5]. Some ready made VI's should then be installed[6] as they will be used to access the converter from LABVIEW. Details on the use of the device can be found in the corresponding manual[7].

Practically, a self made macro is used to set a new voltage on the controller: `UTA12 setvoltage 3.0.vi`. It takes two inputs: the command and the desired voltage. The command input should be "setvoltage" and the voltage is a real number from 0 to 10.

Pressure reading

In addition to the control of the instruments, it is necessary to continuously read the pressure inside the chamber. This is read from the pressure gauge controller `Center One` (Leybold GmbH), which is connected to the main pressure gauge of the chamber, through an RS232 interface. The `Center One` is usually connected to COM port 2 of the USB to RS232 converter. A self made routine can be used to read the pressure: `pressure reading 3.0.vi`. The only input is the COM port number (5 in this case). The pressure is then output as a real number (in mbar units). The `Center One` reads the pressure every 0.1 s. The maximum reading rate for the pressure is therefore hardware limited to 10 Hz.

A.3 LABVIEW program architecture

The LABVIEW based control program is written as a modular architecture. The main concept lies in an infinite loop where the different tasks are run simultaneously

[5] `http://www.elektroautomatik.de/fileadmin/downloads/uta_usb_driver.zip`
[6] `http://www.elektroautomatik.de/fileadmin/downloads/UTA12_7.0.zip`
[7] `http://www.elektroautomatik.de/fileadmin/downloads/uta_direct_guide.zip`

and results obtained are transferred to global variables. This brings full flexibility to separately control the different instruments and ease the data exchange from subroutine to subroutine. The different actions the user can perform are usually supported by event handlers, which will perform requested tasks upon the completion of specific actions (like a mouse click). The block diagram of the main control program is given in Fig A.5.

Two special subroutines are implemented to perform dedicated tasks. The first one is the *oxidation cycle* routine. It allows to perform a controlled oxidation of the layers. The input parameter are the desired oxidation pressure (+ tolerance to variation), the total exposure and a starting value for the leak valve voltage (to give a starting value for the valve regulation). Once it is started, the valve is operated so that the requested pressure is reached using a regulation loop. The pressure is integrated over time to obtain a precise calculation of the total exposure. The block diagram of the oxidation cycle subroutine is shown in Fig A.6. The second subroutine is called *multilayer preparation* and is used to perform a completely automatized deposition process. That means that mass flow controller, sputter sources and shutters will be operated automatically. From the graphical user interface frontend, one can select the deposition time, pre-sputtering time, source setpoint and mass flow controller setpoint. Also one can use up to three different sputtering parameters in a row, and include oxidation cycles between the deposition. After that, one can also decide to repeat the layer stack a defined number of time, to create a superlattice. The block diagram corresponding to a simple deposition cycle is shown in Fig. A.7. If one adds oxidation cycles or other sputtering steps, they would be added at the end of the first sputtering step.

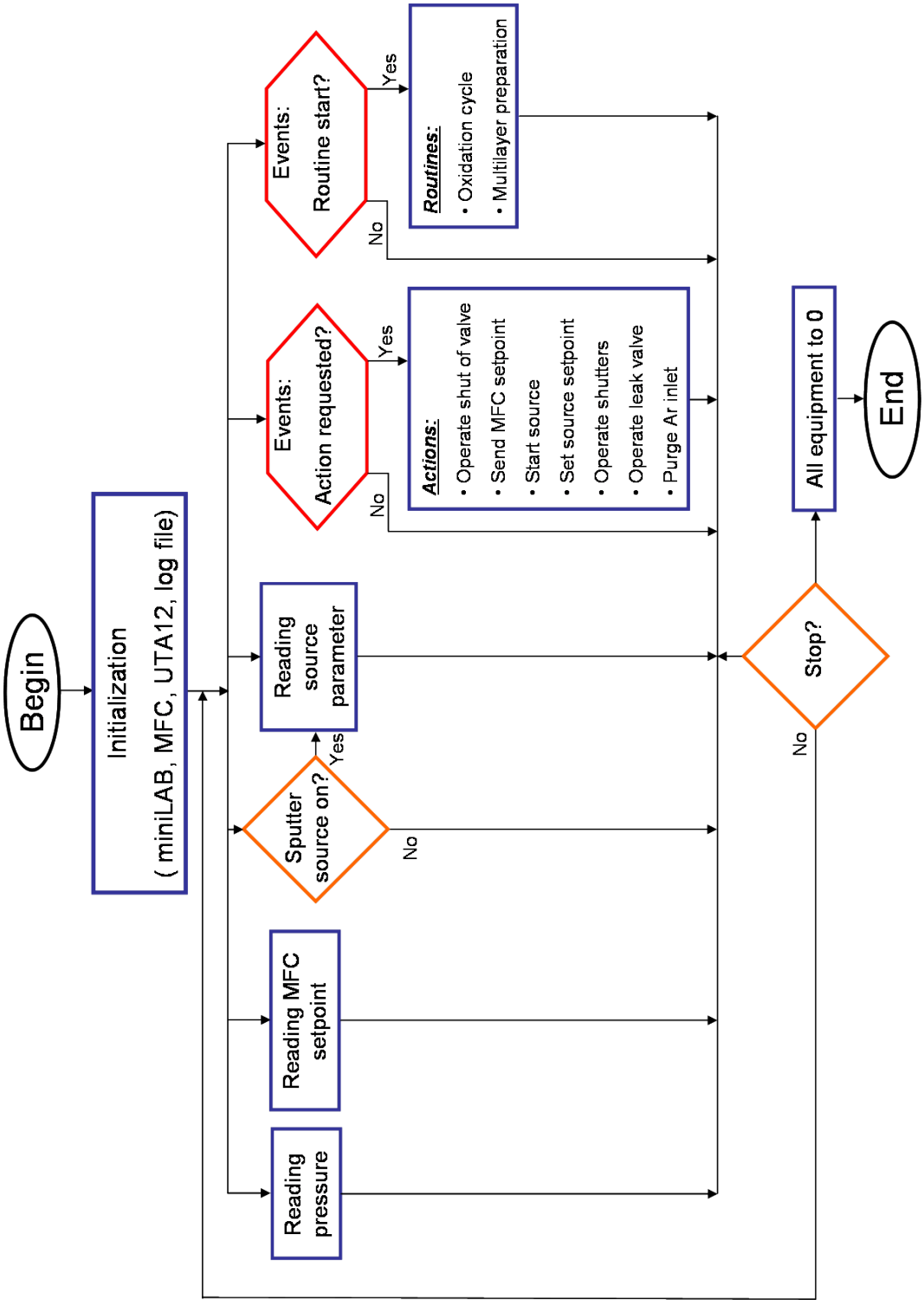

Figure A.5: Block diagram of the main control program.

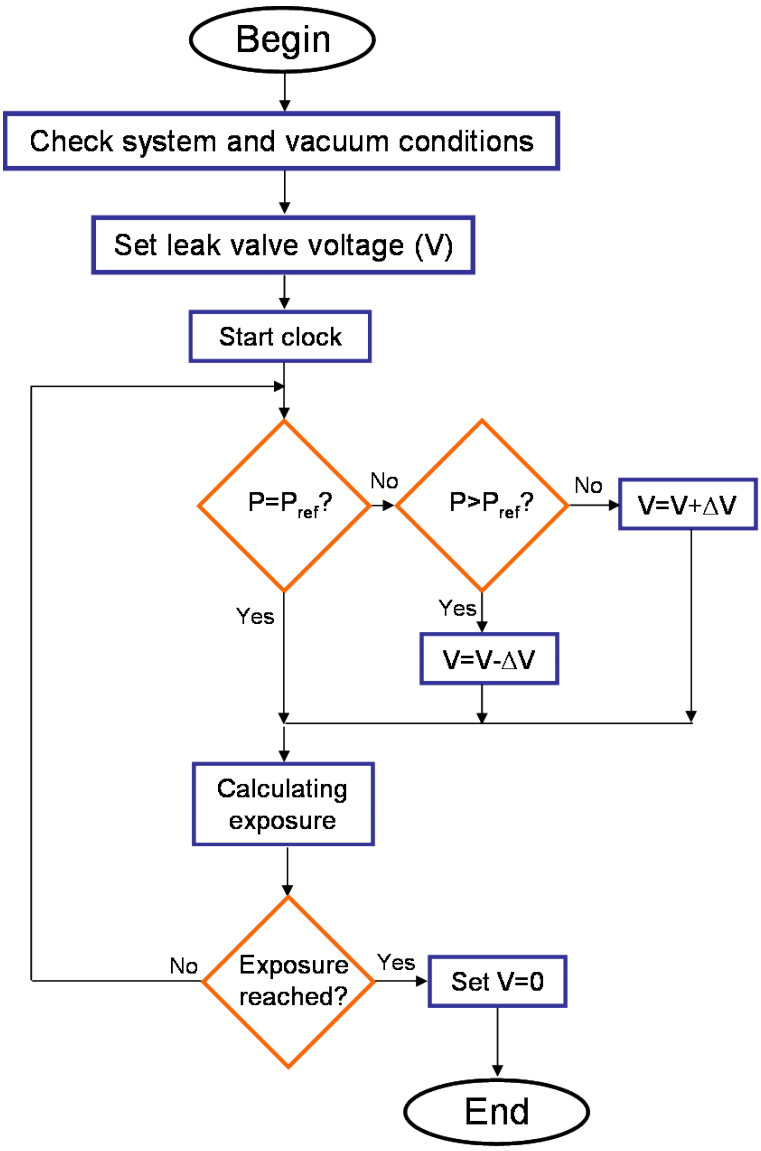

Figure A.6: Block diagram of the *oxidation cycle* subroutine.

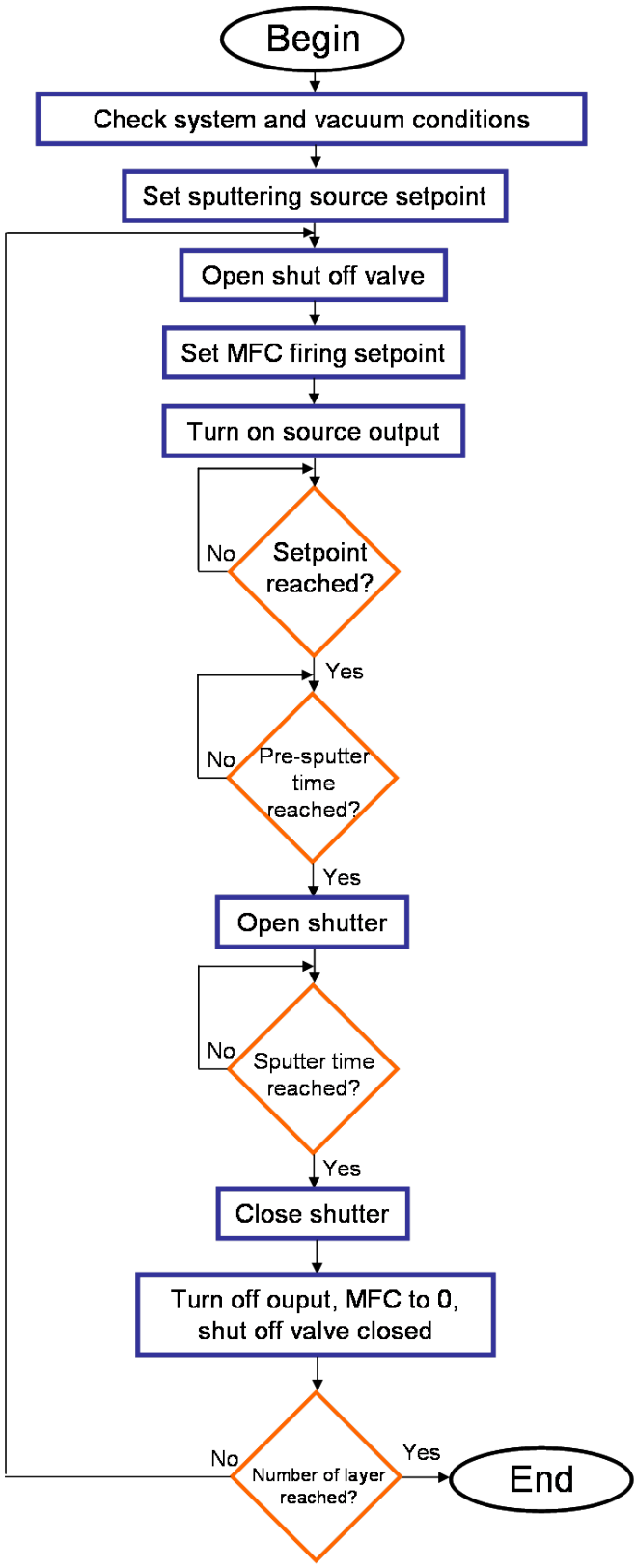

Figure A.7: Block diagram of the *multilayer preparation* subroutine.

Appendix B

Influence of the oxide thickness

In the following, magneto-optical Kerr effect hysteresis curve of Fe/Fe-oxide multilayers are displayed. The sample preparation was similar to what is described in chapter 5. For each sample, a total of 15 bilayers was deposited. The initial Fe thickness was kept constant at 2.5 nm and the oxygen exposure was varied. As can be seen in Fig. B.1, the coercivity is strongly varying when thinner oxide layer are used. One can also see that the magnetic anisotropy is also thickness dependent. The comparison of hysteresis curves at 1170 L and 520 L shows that both axis seems to be inverted. Several curves also displays a double switching behavior. In particular the transition from 650 L to 260 L shows that an increasing part of the moments switch at higher fields. This behavior is not clearly understood yet but might be related to an increase of the coercivity of the layer stack due to the formation of ferromagnetic bridge (pinholes) when ultrathin oxide layer are used.

Figure B.2 displays the measured coercivity as a function of the oxygen exposure used to grow the oxide layers. Surprisingly, this curve presents two minimas and show a general increase of the coercivity for thinner layer. Understanding this phenomenon requires further studies which are behind the scope of this work. However, it clearly shows that one can obtain layer systems with strongly varying magnetic response by simply varying the oxide layer thickness. The role of the oxide layer thickness should be investigated in more details in the future.

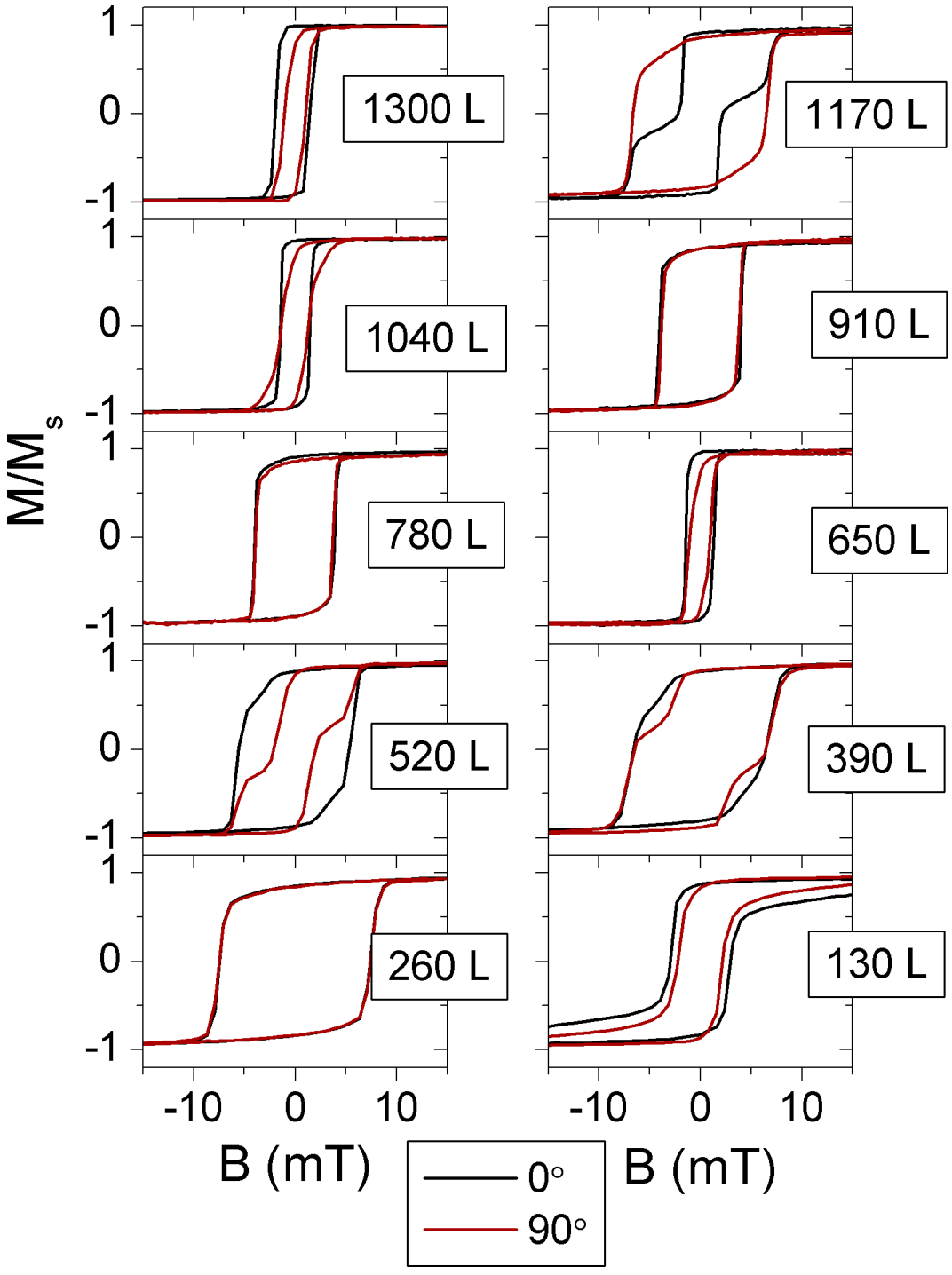

Figure B.1: MOKE hysteresis curves recorded on Si/[Fe(2.5 nm)/O(x)]$_{15}$/Ta(3 nm) multilayers where the native oxide was grown with different oxygen exposures.

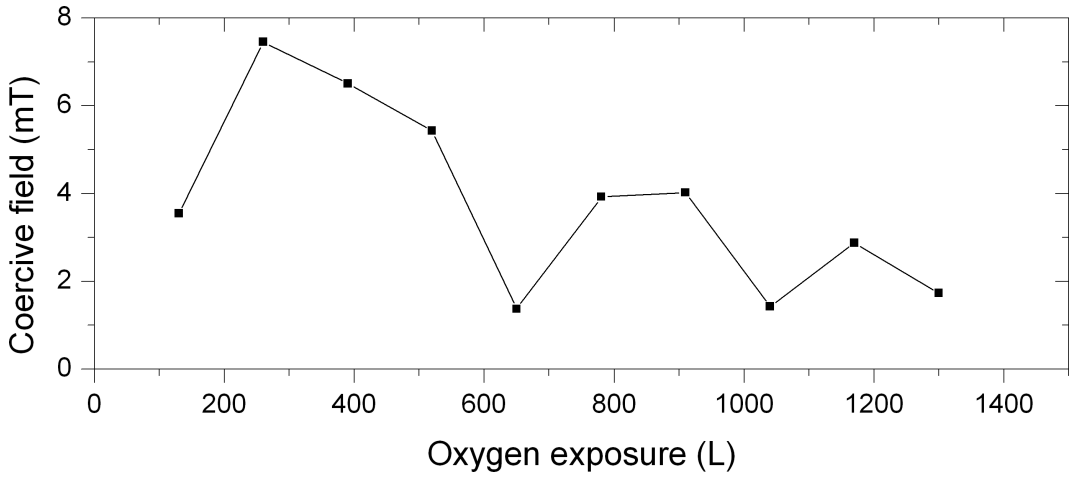

Figure B.2: MOKE hysteresis curves recorded on Si/[Fe(2.5 nm)/O(x)]$_{15}$/Ta(3 nm) multilayers where the native oxide was grown with different oxygen exposures.

Paper I
A compact UHV deposition system for in-situ study of ultrathin films via hard x-ray scattering and spectroscopy

A compact UHV deposition system for *in situ* study of ultrathin films via hard x-ray scattering and spectroscopy

Sebastien Couet,[a] Thomas Diederich, Kai Schlage, and Ralf Röhlsberger
Deutsches Elektronen Synchrotron (DESY), Notkestraße 85, 22603 Hamburg, Germany

(Received 4 June 2008; accepted 25 August 2008; published online 23 September 2008)

We report on a compact ultrahigh vacuum deposition system developed for *in situ* experiments using hard x rays. The chamber can be mounted on various synchrotron beamlines for spectroscopic as well as scattering experiments in grazing incidence geometry. The deposition process is completely remotely controlled and an ellipsometer is available for online monitoring of the layer growth process. The unique sample position in the chamber allows one to perform deposition, grazing incidence x-ray experiments, and ellipsometry measurements at the same time, enabling to correlate the x-ray analysis with parameters of the growth process. Additionally, the setup can be used to study *in situ* chemical and structural changes in an element specific manner by x-ray absorption spectroscopy. The flexibility and versatility of the system brings new possibilities to study the chemistry and structure of surfaces and interfaces in thin films systems during their formation. [DOI: 10.1063/1.2982059]

I. INTRODUCTION

Nowadays, thin films and multilayer structures are used in a large range of applications such as optical coating, microelectronics,[1] solar cell technology,[2] or magnetic recording.[3] Physical vapor deposition techniques such as molecular beam epitaxy or sputter deposition allow for a controlled deposition process and are widely used to grow thin films or multilayer structures. Generally, the properties of the complete system are largely influenced by the quality (structure, chemistry, thickness) of the different interfaces. The study of the growth process during the interface formation is therefore mandatory to tailor the properties of the final device. Usually, an ultrahigh vacuum (UHV) environment is required to study free surfaces, interface formation, or more generally, for any type of *in situ* study where analysis has to be carried out at selected steps of the preparation procedure. A large variety of analysis technique based on electron probes (Auger spectroscopy, x-ray photoelectron spectroscopy, low energy electron diffraction, etc.) as well as scanning probe microscopy techniques are readily available in common UHV systems. While a combination of these techniques can bring a complete characterization of the chemistry and morphology of thin film surfaces, their probing depth is usually restricted to a few nanometers.

On the other hand, hard x-ray scattering techniques are usually used to probe the structure of bulk material on various length scales in a noninvasive way. The possibility to tune the energy (or wavelength) of the x-ray photons to a particular absorption edge can be used to study chemical and structural parameters of the sample in an element specific manner.[4] The case of grazing incidence scattering is particularly interesting for the study of thin films and multilayers because this geometry allows to control the penetration depth of the x rays. Scattering and spectroscopy techniques can therefore be used in a depth resolved manner to study buried layers and interfaces.

Specular x-ray reflectivity can be used to obtain depth resolved density profiles with subnanometer resolution.[5,6] The analysis of the diffusely scattered radiation at small angles of incidence allows one to obtain information on the lateral ordering of layers or clusters on various length scales.[7] Resonant techniques such as nuclear forward scattering combined with the use of isotopic probe layers can be used to obtain magnetic depth profiles with sub nm resolution.[8]

The high intensity provided by modern synchrotron radiation sources enables one to collect data sufficiently fast to perform time resolved studies. In the last decade, the applications of x-ray scattering techniques to follow thin film growth *in situ* have attracted an increasing interest. In particular, *in situ* x-ray reflectivity was often used to follow the evolution of the film morphology (roughness, thickness) in real time during growth.[9–13] In order to perform reflectivity as well as other x-ray scattering experiments, several portable deposition systems have been developed.[13–15] They usually feature a compact design with large x-ray windows which allows to perform different x-ray scattering experiments such as reflectivity and small angle scattering. They usually accommodate space for Knudsen cells, e-beam evaporators, or sputter guns and have high (sometimes ultrahigh) vacuum capabilities.

In this paper, we describe a compact UHV deposition chamber that was developed to perform grazing incidence scattering and spectroscopy experiments *in situ* using hard x rays. The primary goal of this device is to study the growth and the interface formation of transition metal elements (Fe, Co, and Ni), as well as oxidation processes on such metallic surfaces. This requires particular care regarding vacuum

[a]Author to whom correspondence should be addressed. Electronic mail: sebastien.couet@desy.de.

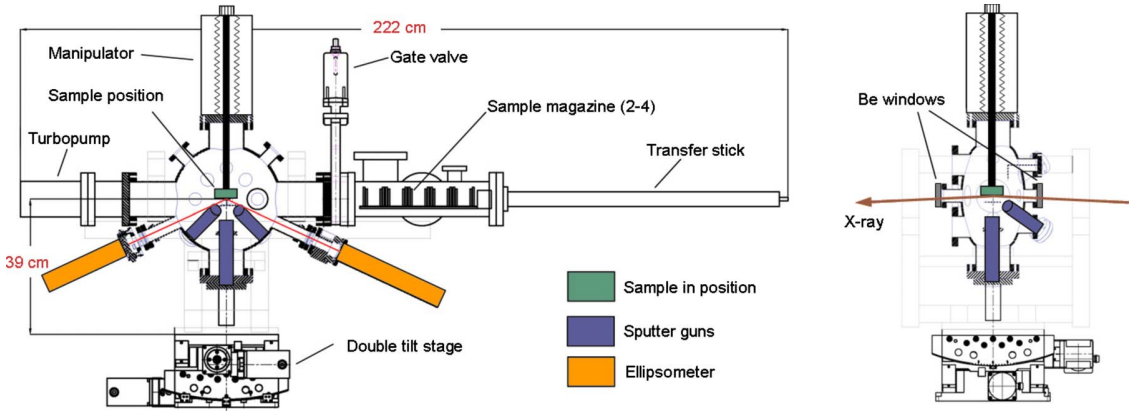

FIG. 1. (Color online) Sketch of the UHV deposition system. The sample is located in the center of the deposition/scattering chamber. Three sputter guns are implemented for deposition of different materials. An ellipsometer attached to the chamber allows one to monitor the growth process during deposition. The sample is in the center of rotation of a two-circle goniometer, allowing for precise angular adjustment with respect to the incoming x-ray beam. A load lock attached to the system is used for fast sample transfer without breaking the main chamber vacuum. The relatively compact dimensions of the system allows one to install it in many experimental stations of present synchrotron radiation sources.

quality and surface modification monitoring. The system has been kept compact to fit in most synchrotron experimental hutches without compromising the experimental flexibility. In particular it is equipped with a load/lock system for fast sample exchange and an ellipsometer for online monitoring of the growth process. The ellipsometry, together with a complete remote control of the deposition process, allows one to precisely follow the evolution of the sample surface during the x-ray scattering experiments. In the first part, the technical design and the general possibilities of the setup are discussed. As an example and a first application of this system, we will present two techniques which were combined to resolve the magnetic and chemical structure of free and buried native iron oxide layers. First, an *in situ* nuclear forward scattering experiment will demonstrate the possibilities to study magnetic thin film's growth in grazing incidence geometry. The second part is devoted to *in situ* x-ray absorption spectroscopy (XAS) experiments on ultrathin transition metal layers.

II. TECHNICAL DESIGN

One of the main goals was to build a system that is small enough to fit in most of the synchrotron experimental stations yet having enough freedom to keep flexibility in the sample preparation. The main concept relies on the sample position in the center of the chamber which is the same for deposition, grazing incidence x-ray scattering, and ellipsometry measurements, as depicted in Fig. 1. As will be described later, this geometry allows one to perform real-time studies where the deposition takes place at the same time as x-ray scattering data are collected.

The system is composed of a main UHV chamber that is used for the film preparation and the analysis using x rays, and a load-lock system for fast sample transfer without breaking the main chamber vacuum. As can be seen in Fig. 2, the system is surrounded by a rigid aluminum cradle (made of aluminum profile Rose-Krieger F50), which can be mounted on a heavy duty two-circle goniometer (maximum load 200 kg, HUBER Diffraktionstechnik GmbH, model 5202.8). This goniometer is equipped with step motors which achieve an angular precision of 10^{-5} deg. The center of rotation of this double tilt stage is located at the sample position, 390 mm above the goniometer plate. As will be described later, precise sample alignment with respect to the x-ray beam is achieved by moving the complete system placed on heavy duty horizontal and vertical (X-Z) translation tables commonly available at synchrotron facilities. This scheme leads to sample positioning precision of few microns with respect to the beam, without affecting the sample position in the chamber. With total dimensions of 222×80 cm^2, the system is still compact enough to be mounted on various synchrotron experimental stations.

UHV conditions are reached using a two stage turbomolecular pumping scheme coupled to a membrane pump. This is an oil-free pumping system that can easily reach UHV conditions ($<5 \times 10^{-10}$ mbar routinely achieved) and sustain gas injection at moderate pressure ($10^{-5}-10^{-2}$ mbar). The pressure in the main chamber is read out by a hot cathode pressure gauge ITR100 from Leybold (pressure range of $1.0 \times 10^{-10}-3 \times 10^{-2}$ mbar). In addition to the flanges used for sputter sources, ellipsometry and gas inlets, 3 CF40 and 1 CF63 flange can be used to connect other equipments such as additional gas inlet or a mass spectrometer.

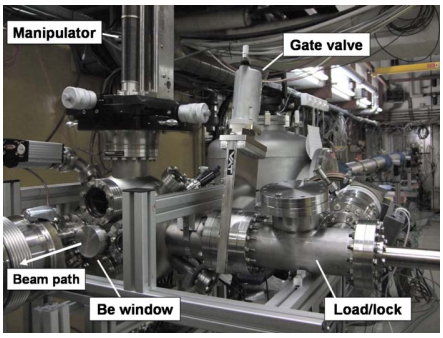

FIG. 2. (Color online) Picture of the deposition system at the BW4 beamline of HASYLAB. The beam enters and exits the chamber in grazing incidence geometry. A protection cap is placed on the Be exit window.

The load lock is equipped with a turbopump connected to another membrane pump. When high vacuum is reached in the load-lock chamber ($p < 1 \times 10^{-5}$ mbar), the membrane pump is disconnected to allow the load/lock turbopump to be connected to the second turbomolecular pumping stage. This way, pressures below 1×10^{-8} mbar can be reached in the load lock without the need for a baking out procedure. A sample magazine containing a maximum of four samples is available and transfer to the main chamber is done through a large CF100 gate valve. The details of the sample transfer system are given in Sec. II A. Two entrance and exit beryllium (PF-1 grade, Brush Wellman Inc.) windows for hard x rays can be used. They are 3.5 cm in diameter (placed on a CF40 flange) and have a thickness of 120 μm. This small thickness, together with the high purity grade, is chosen to avoid parasitic signal from eventual traces of heavy elements. In particular, the low concentration in Fe is particularly suited for nuclear forward scattering experiments on ^{57}Fe nuclei where any traces of Fe along the path of the x-ray beam lead to background signal. The transmission through this type of window is as high as 70% for energies above 3.5 keV. Moreover, the windows do not modify the beam profile significantly, as evidenced in a recent grazing incidence small angle x-ray spectroscopy (GISAXS) experiment.[16]

The system can be mounted on the beamline in 1 day while proper bakeout and cool down procedure requires another 3 days. For that reason, the setup is usually mounted in an unused experimental hutch while other experiments can be carried out in another experimental hutch of the beamline. If this scheme is not applicable, mounting the system during a longer shutdown period of the synchrotron (such as maintenance week) is usually preferred to maximize the use of the photon beam.

A. Sample environment

The main specifications for the sample holder system are imposed by the grazing incidence geometry used. The x-ray beam usually exhibits a vertical beam size in the range of 30–60 μm. Because the beam impinges on the surface at grazing angles (usually below 1°), this leads to a beam footprint size on the sample of 10–20 mm. In order to collect the full signal and avoid parasitic scattering from the sample edges, this requires samples of similar dimensions. The sample holder was therefore designed to accommodate relatively large samples and provide a completely free pathway for the x-ray beam in grazing incidence.

Three different types of sample holders are available. The first one is designed to fit samples as large as 25 $\times$ 40 mm^2. It can be used in any case where parasitic scattering from the sample holder edges has to be avoided, like in GISAXS. The second type of sample holder was developed to perform magnetic studies. It provides a permanent magnetic field of 70 mT in the plane of the sample. As shown on Fig. 3(a), it consists of hard (NdFeB) and soft (Fe) magnetic material and the design was optimized to provide better than 3% field homogeneity over the sample surface (20 $\times$ 15 mm^2). Finally, a sample holder equipped with a specially designed heater stage was developed to perform temperature dependent studies. As depicted in Fig. 3(b), the

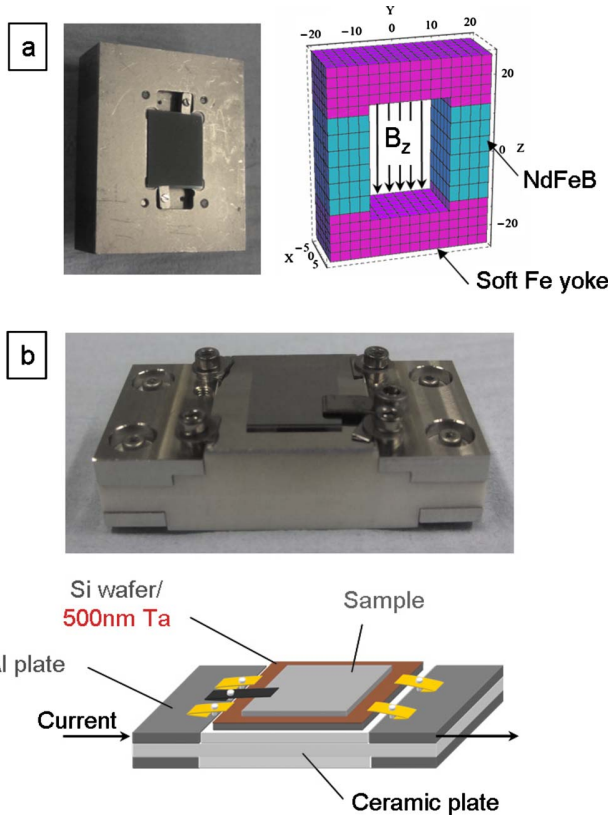

FIG. 3. (Color online) (a) Picture of the magnetic sample holder. The right part displays a schematic of the magnet configuration leading to an in-plane permanent magnetic field of 70 mT. (b) Picture and principle diagram of the heater. The sample is resistively heated via current flow through a 500 nm thick Ta layer on a Si wafer. The temperature is measured by a PT100 temperature sensor placed on the backside of the Si wafer.

sample is placed on a Si wafer coated with a 500 nm thick Ta layer. Heating is achieved by feeding a current of a few amperes through the Ta layer. This particular design allows for fast heating (up to 600 K/min) and cooling of the sample. The temperature is measured by a UHV compatible PT100 temperature sensor placed on the backside of the Si wafer. Temperature stability better than 0.1 K is achieved by proportional integral derivative regulation of the heating current. *In situ* temperature dependent x-ray experiments have not yet been carried out, but it is expected that the temperature stability achieved here should ensure stable experimental conditions once thermal equilibrium is reached.

In all cases, the holder is placed on a three axis rotary manipulator that allows a positioning of the sample in the center of the chamber with 0.1 mm accuracy. The position of the sample surface with respect to the center of rotation was determined by placing the sample in the center of the entrance window. This position can be easily reproduced upon sample change by controlling the position of the reflected laser beam of the ellipsometer from the sample surface. The position of the center of the window above the goniometer plate is then calculated to be in the center of rotation of the goniometer. The rotation of the sample enables one to perform scattering experiments along different in-plane orientations of the sample.

Two different sample transfers are available. In both

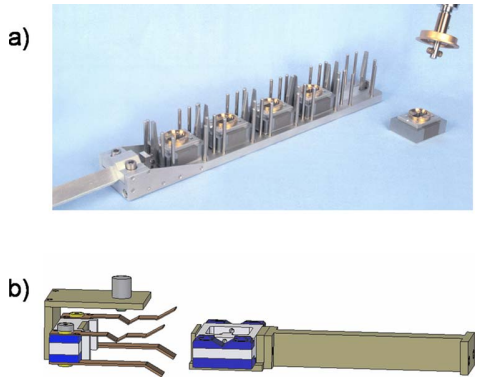

FIG. 4. (Color online) (a) Picture of the sample transfer system for room temperature sample holder. The sample is attached to the manipulator from the backside using a bayonet locking system. (b) Schematic drawing of the transfer system for the heater stage. The two clamps provide electrical contact for the heating plate and the PT100.

cases, the sample is slid horizontally from the load lock using a transfer stick. For the room temperature holders, the manipulator attaches to the backside of the holder using a bayonet system, as shown on Fig. 4(a). For the heater stage, a two fork clamping system is used on the manipulator. The two forks are used to provide electric contact to the heating plate as well as for the PT100, as shown on Fig. 4(b). Typical time needed to transfer a sample from the load lock to the main chamber is 1 min while the load lock can be pumped to sufficiently low pressure to allow sample transfer in less than an hour.

B. Deposition system

The basic setup of the chamber provides three conflat flanges (one CF100 at the bottom and two CF40 on the sides) centered on the sample position. While several different deposition systems can be implemented (such as Knudsen cells or electron beam evaporators), dc magnetron sputter deposition is usually preferred here for its pronounced advantages. For a given material, the deposition rate is a function of the argon gas pressure and of the power set point of the source only. The growth rate and the energy distribution of the sputtered atoms can be adjusted by controlling those parameters.[17] This gives the opportunity to adjust the morphology of the deposited films. For example, at high Ar pressure the sputtered atoms are thermalized and cluster growth is promoted. Second, the layers produced are homogeneous over areas of several square centimeters (10% thickness variation on a 50 mm diameter film). These are necessary conditions in view of the x-ray grazing incidence experiments. The deposition process is fast: a complete deposition cycle can be achieved in less than 1 min, and allows maximizing the measuring time during the experiment. This type of system can be easily computer controlled, as will be shown in Sec. IID. Finally, dc magnetron sputter deposition is a widely used deposition process in the industry. This setup can therefore be used to mimic industrial processes. The chamber is usually equipped with three dc magnetron sputter sources. The main deposition source is placed below the sample (normal incidence) at a distance of 63 mm from the sample and fits a 33 mm diameter target. At this target-sample distance, the homogeneity of the film is better than 10% on a 50 mm diameter sample. Two other sources (25.4 mm target) are placed on both sides of the sample with an incidence angle of 35° relative to the sample plane. While the oblique incidence prevents the formation of homogeneous layer, it can be used, for example, to imprint magnetic anisotropies in transition metal layers[18] or to deposit a protection layer before bringing the sample back to atmosphere. The deposition of a wedge layer can also provide a means to produce a thickness gradient in the sample. The three sputter guns are equipped with motorized shutters to precisely control the deposition time (opening time <0.5 s). Argon gas (99.9999% purity) is admitted using a mass flow controller which ensures stability and reproducibility of the Ar pressure better than 1% over a pressure range from 3×10^{-3} to 3×10^{-2} mbar.

Additionally, a step motor driven leak valve is mounted on the chamber to admit various gases in the pressure range from 5×10^{-8} to 5×10^{-3} mbar. As will be shown later, it can be used to perform defined oxidation processes by precisely controlling the total oxygen exposure.

C. Ellipsometry

As described above, the chamber is equipped with an ellipsometer used here to monitor the layer growth online. Ellipsometry is based on the measurement of the change in polarization state of visible light upon reflection from a medium. The fundamental ellipsometry parameters (that are measured) are Δ (intensity ratio) and Ψ (phase shift) and can be directly related to the ratio of R^p and R^s, the reflection coefficients for s and p polarized light, respectively,[19]

$$\frac{R^p}{R^s} = \tan\Psi e^{i\Delta}. \tag{1}$$

Since the reflection coefficients depend on the thickness and refractive index of the layer, measuring the change in Δ and Ψ during the deposition allows one to evaluate the thickness and composition of the layer being grown. We use an ELX-1 ellipsometer (Dr. Riss Ellipsometer Bau GmbH, Germany) equipped with a He–Ne laser emitting at 632.8 nm. The laser and detector are attached to the chamber symmetric to the sample position and perpendicular to the x-ray scattering plane, as shown on Fig. 1. The incidence and exit angle is fixed to 65° with respect to the sample surface. The determination of Δ and Ψ is performed by rotation of a quarter wave plate and an analyzer (placed in front of the detection diode) to minimize the transmitted intensity. A measurement cycle can be performed at 1 Hz repetition rate.

Figure 5 shows the ellipsometry curve for a typical multilayer structure grown during our experiments. In this case, a 2.5 nm thick Fe layer is sputter deposited at a growth rate of 0.1 nm/s. The layer is subsequently oxidized by controlled exposure to oxygen. A second Fe layer and an Al capping layer are subsequently deposited. Ellipsometry data are acquired continuously during the deposition. The growth of each layer corresponds to characteristic variation of Δ and Ψ in the ellipsometry curve. Modeling of the multilayer *a posteriori* allows one to relate the change in Δ and Ψ to the

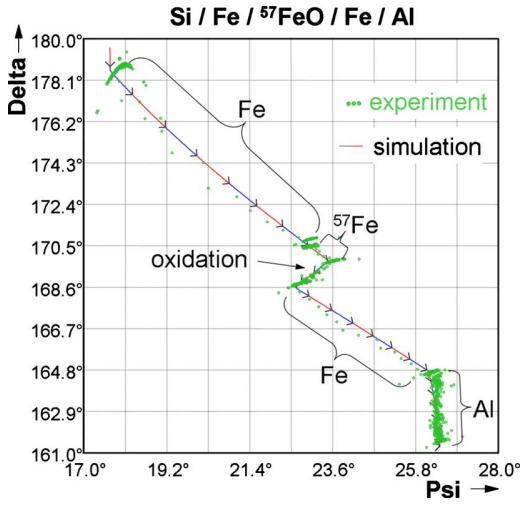

FIG. 5. (Color online) Ellipsometry curve of the growth of a Si/Fe (2.2 nm)/^{57}Fe–O (1.5 nm)/Fe (2.2 nm)/Al (3 nm) multilayer. The growth of each different layer shows a distinct evolution of the ellipsometry parameters Δ and Ψ. The simulation allows one to estimate the refractive index and the thickness of each layer.

refractive index and the thickness of each layer. This model can subsequently be used to monitor the growth process and determine when a certain layer thickness has been deposited. In the case of films below 5 nm, the precision is sufficient to measure monolayer coverage. Above that thickness the sensitivity progressively decreases due to the limited probing depth of light in metals. Furthermore, the technique is highly sensitive to oxidation processes on the surface and can be used to monitor eventual surface chemistry changes during an ongoing x-ray analysis. This is an important aspect either to monitor beam damage in the case of soft substrate (polymer), or to monitor adsorption of molecules due to the rest gas pressure on reactive surfaces.

As mentioned earlier, the ellipsometer is also used to check the position of the sample in the center of the chamber. Because the photodiode as a small entrance window of 2 mm diameter only, the position of the reflected beam is highly sensitive to the height of the sample in the chamber. Checking the reflection, one can easily reproduce the same sample position upon sample change.

D. Remote control system

For an x-ray experiment, the UHV system will be mounted inside the experimental hutch which will not be accessible during the measurement. To provide maximum flexibility and allow for real-time (deposition plus analysis) experiments to be performed, the deposition is completely remote controlled from outside the experimental hutch.

The different equipments operate using different communication protocols (analog signals for the sputter sources, RS232 for mass flow controller and pressure gauge, etc.). An interface box containing all the necessary converters (analog to digital and digital to analog converters, digital input output, relays, etc.) has therefore been designed to merge all the required connections to one single input/output USB port. The complete setup is then controlled using a LABVIEW program running on a remote laptop computer. This flexible solution is easily transportable and completely independent of the different computer systems used at the various synchrotron facilities. The control program presents itself as a single window graphical user interface (GUI), as shown in Fig. 6. Each instrument can be operated independently or at the same time with a continuous monitoring of all the relevant parameters such as pressure, mass flow controller set point, current, voltage, and power of the sputter sources. This gives full flexibility and security over the preparation procedure. Additionally, special procedures have been implemented to perform automatized tasks. The "oxidation cycle" routine can, for example, be used to perform a controlled oxidation of the deposited layer. In that case, the gas pressure is recorded as a function of time (10 Hz sampling rate). The pressure is then integrated over time, which allows one to calculate and precisely control the total exposure (pressure $\times$ time) of the sample to the gas. This can be used to perform oxidation cycles with exposure reproducibility better than 1%. The two parameters that have to be provided are therefore the gas pressure and total exposure desired. Additionally, a deposition sequence can be programed to grow complex multilayer or superlattice structures.

III. X-RAY SCATTERING TECHNIQUES TO STUDY THE GROWTH OF THIN METAL AND OXIDE FILMS

The general geometry for grazing incidence experiments is depicted on the right side of Fig. 1. This is a vertical scattering geometry where the x-ray beam is reflected downward. The two Be windows are placed on each side of the chamber to let the x-ray beam in and out in grazing incidence geometry. The distance from the center of the sample to the entrance or exit window is fixed to 17.5 cm which therefore allows measurements up to incident angles of $\theta=4°$ ($2\theta=8°$).

In the following, we describe an experiment that aimed at the determination of the evolution of the magnetic structure of buried native iron oxide layers during their formation. This type of ultrathin oxide layers (produced by exposure of a metal substrate to molecular oxygen) embedded in its metal counterpart are expected to exhibit structural and magnetic properties that deviate strongly from any bulk iron oxide phases. In particular, an anomalously high magnetic moment per atom[20] as well as an antiferromagnetic ordering at room temperature[21] were reported recently. In order to unravel how such magnetic properties evolve in buried native oxide layers, we studied the formation of these layers *in situ* by nuclear forward scattering. For an overview of the experimental technique, see Ref. 22 and references therein. The sensitivity of the method to the magnetic structure of buried layers combined with the possibility to completely isolate the oxide signal from the surrounding metallic Fe by using isotopic probe layers render this technique an ideal candidate for this type of investigations. This experiment is a stepwise experiment where x-ray scattering is performed after each deposition/oxidation and was for the first time made possible thanks to this setup.

The experiment was performed at the nuclear resonance beamline ID18 of the European Synchrotron Radiation

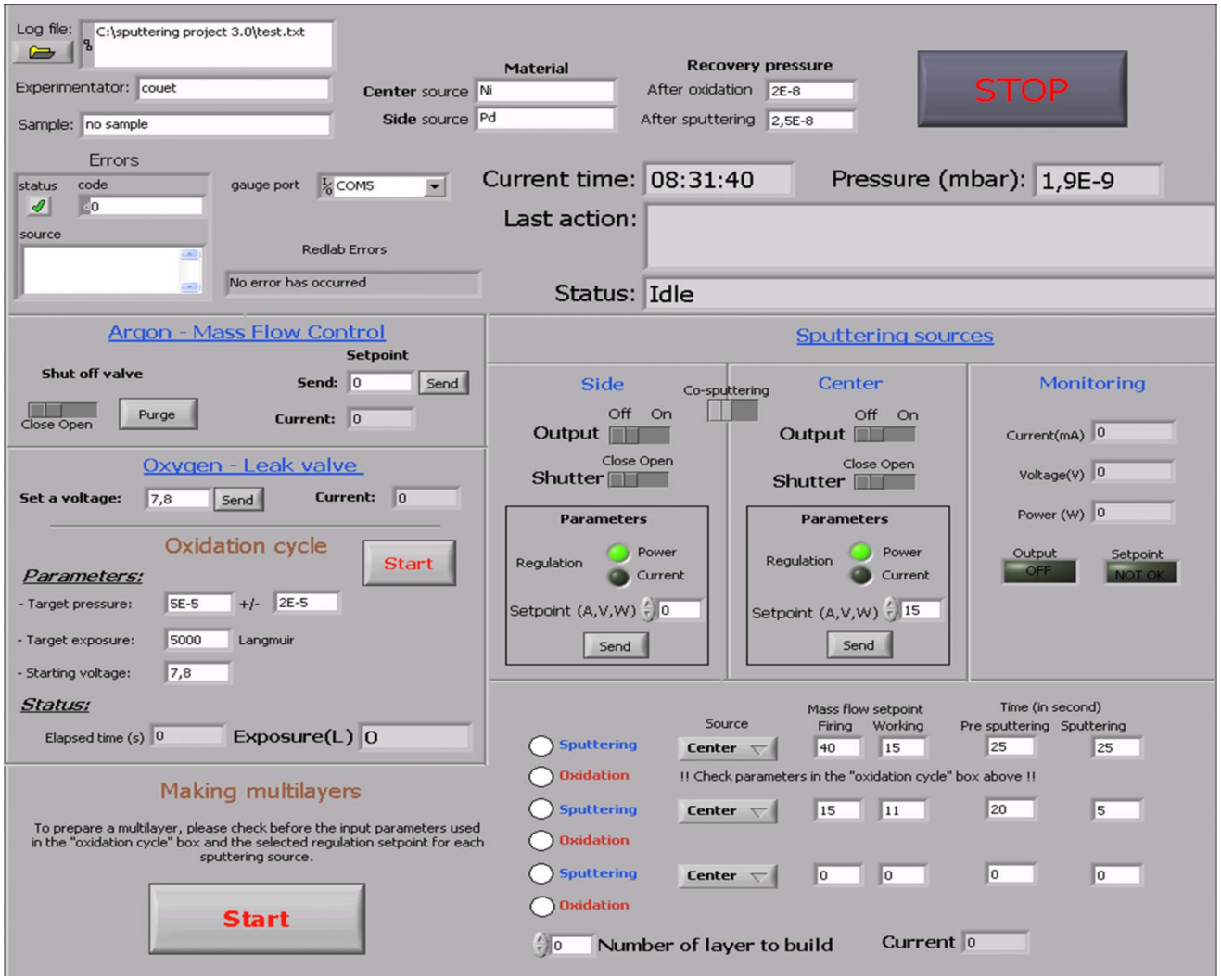

FIG. 6. (Color online) GUI of the LABVIEW based control program for the deposition process. Separate control and monitoring is available for each sputter sources and gas inlets. A sequence of deposition and gas exposure step can be programed to grow multilayer structures consisting of metal and oxide films.

Facility (ESRF).[23] The UHV system was placed on the double tilt stage referenced in Fig. 1. To precisely position the sample relative to the incoming x-ray beam, the whole system was placed on an *X-Z* table (lateral +vertical movement which allowed alignment of the sample with respect to the X-ray beam with a few micron accuracy). The beam was focused to 30 μm in the vertical direction using a Kirkpatrick–Baez mirror to match the sample cross section in grazing incidence geometry. The substrate [superpolished Si(100) wafer] was placed on a magnetic sample holder to fix the magnetization direction. In order to study exclusively the magnetic properties of the native oxide, we deposited an ultrathin (0.6 nm) ^{57}Fe probe layer on top of a 2 nm thick Fe layer. The layer was then oxidized to saturation and stepwise covered with Fe. The experiment was performed at a fixed incidence angle θ of 0.24°, which is well above the critical angle of Fe (0.21°) at 14.4 keV. At each preparation step, nuclear time spectra (the temporal evolution of the nuclear decay after pulsed excitation) were recorded to follow the evolution of the magnetic structure.

Figure 7(a) shows the time spectra corresponding to the pure 0.6 nm thick ^{57}Fe layer deposited on top of the 2 nm thick ^{nat}Fe layer. The fast beating pattern corresponds to a hyperfine field B_{HF} of 32 T, a typical value for ferromagnetic α-Fe at room temperature. The shape of the spectra indicates that the magnetization is oriented in the plane of the sample parallel to the incoming photon wavevector and the external field. After exposure to 6500 L (1 L=10^{-6} Torr s) of oxygen, the ^{57}Fe probe layer is completely oxidized and the fast beating is replaced by a long period oscillation [Fig. 7(b)] due to residual quadrupole interactions in the oxide. The small hyperfine field associated with this beating indicates that the free native oxide is in a superparamagnetic or nonmagnetic state. Subsequent deposition of Fe [Figs. 7(c)–7(e)] leads to a reappearance of a fast beating, indicating a progressive magnetic ordering of the oxide layer. While chemical changes in the oxide are expected upon deposition of Fe, the progressive magnetic transition suggests that the magnetism in the buried native oxide is supported and stabilized by the surrounding metallic Fe. Complementary results can be found in Ref. 21.

The experiment shows the potential to perform *in situ*

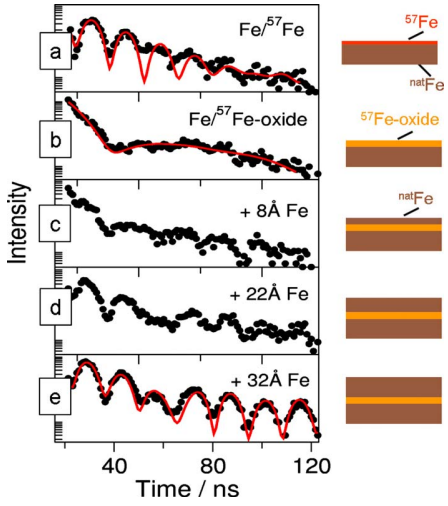

FIG. 7. (Color online) Results of a nuclear forward scattering experiment where an ultrathin ^{57}Fe probe layer is used to resolve the magnetic structure of a buried native oxide layer at different steps of the growth. (a) Time spectra of the pure 0.6 nm thick ^{57}Fe probe layer placed on top of a 2 nm ^{Nat}Fe layer. The fast beating is related to the ferromagnetic ordering of α-Fe. (b) Oxidized ^{57}Fe oxide. The large period beating indicates a nonmagnetic state. [(c)–(e)] Progressive reappearance of the beating pattern with increasing Fe coverage, sign of a recovery of the magnetic order.

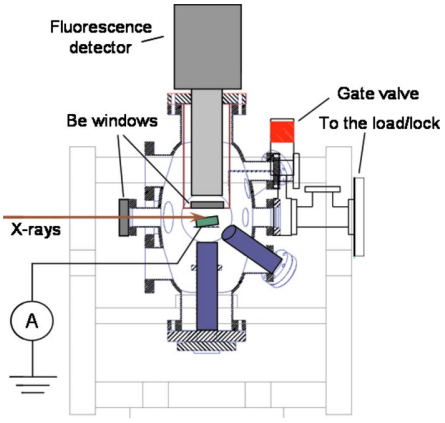

FIG. 8. (Color online) Sketch of the setup for x-ray absorption experiment. Compared to the setup presented in Fig. 1, the manipulator is placed in horizontal position. The incidence angle is therefore adjusted manually. The load lock is connected to the main chamber through a smaller CF40 gate valve. This allows placing the fluorescence detector in vertical geometry 4 cm above the sample. The TEY is recorded by measuring the drain current on the sample using a low current electrometer (Keithley 4517A).

x-ray scattering experiments, as it is the only way to observe changes in buried layers during the deposition. In this case, the use of isotopic probe layers allows one to access the magnetic properties of the sample in a layer specific manner. Because of its relation with oxidation process on Fe surfaces, it requires a sufficiently clean environment to avoid contamination during the x-ray analysis (typically 30 min acquisition time). The continuous ellipsometer analysis confirms that the surfaces do not suffer from the long x-ray exposure or from the residual gas pressure. This experiment was made possible for the first time with this setup.

The ability to measure GISAXS was also demonstrated recently. The experiment, performed at the beamline BW4 of the DORIS III storage ring (Hamburg, Germany), showed the possibility to use *in situ* GISAXS to study metal growth on polymer surfaces.[16] In that case, gold was stepwise deposited on a mixed diblock-triblock copolymer and GISAXS patterns were taken at selected gold coverages. This allowed evidencing a progressive diffusion of the gold particles into the polymer matrix and a preferred agglomeration of gold clusters around one of the two polymer chains. This type of experiments can also be coupled with the ellipsometry measurement, providing a unique picture of the optical properties as well as the microscopic structure of the film in real time.

Another possible approach is to record GISAXS patterns *during* the growth. Preliminary experiments carried out at the BW4 beamline[24] have shown that GISAXS patterns with sufficiently high statistics can be acquired within 1 s with this setup. The development of fast read-out large area single photon counting detectors based on hybrid pixel technology[25] opens the possibility to record GISAXS pattern in only a few ten ms.

IV. X-RAY SPECTROSCOPY OF ULTRATHIN FILMS

Soft XAS is already a widely used technique to probe chemistry and magnetism of thin films *in situ*. In this energy range however, the resonant absorption usually leads to a strong reduction in the probing depth. This results in complicated data analysis in the case of depth sensitive experiments. In addition, when the fluorescence signal is measured, it is often integrated over the energy. This prevents, for example, to isolate the extended fine structure part of the signal (which usually extents up to 800 eV above the edge). These problems are overcome in the case of hard XAS where energy dispersive fluorescence detectors are generally available.

A classical hard x-ray absorption experiment takes place in transmission geometry where the intensity of the incident and transmitted x-ray beam is measured as a function of the photon energy. However, thin films are usually grown on thick, absorbing substrates (such as silicon or glass) and the transmission geometry is not applicable.

Two other detection schemes can be used for thin film studies: the fluorescence yield (FY) and the total electron yield (TEY). The FY measures the fluorescent photons reemitted by the absorbing atoms. This is an energy dispersive single photon counting measurement which allows one to isolate the contributions from different elements. The technique has a large probing depth (limited only by the attenuation of x ray in matter) but suffers from self-absorption effects[26] in concentrated samples. On the other hand, the measure of the TEY provides an energy integrated signal that is intrinsically surface sensitive. It is based on the measure of the drain current on the sample which is induced by the photoabsorption. The usual probing depth of the method is determined by the average mean free path of the electrons in the sample and is estimated to be around 50–100 nm for excitation with hard x rays.[27]

These two systems are therefore complementary: FY can be element selective while TEY provides the desired surface sensitivity. Both detection schemes were implemented on the chamber. As the fluorescent photons are emitted isotropically, the detector has to be placed as close as possible to the sample to cover a sufficiently large solid angle. As shown in

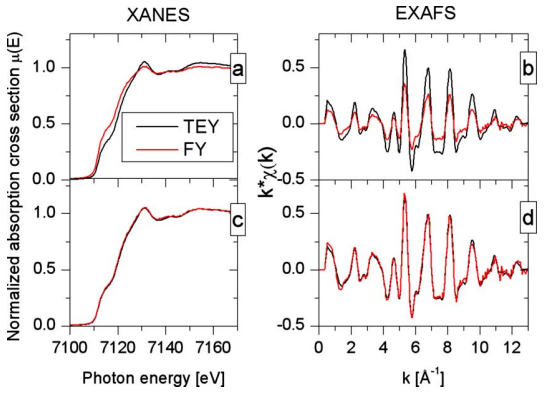

FIG. 9. (Color online) Comparison of the TEY and FY signals of a 30 nm thick Fe layer. The incidence angle was 20°. (a) Normalized XANES spectra. (b) Weighted EXAFS spectra. [(c) and (d)] Results after correction of the FY for self absorption: the two signals match almost perfectly.

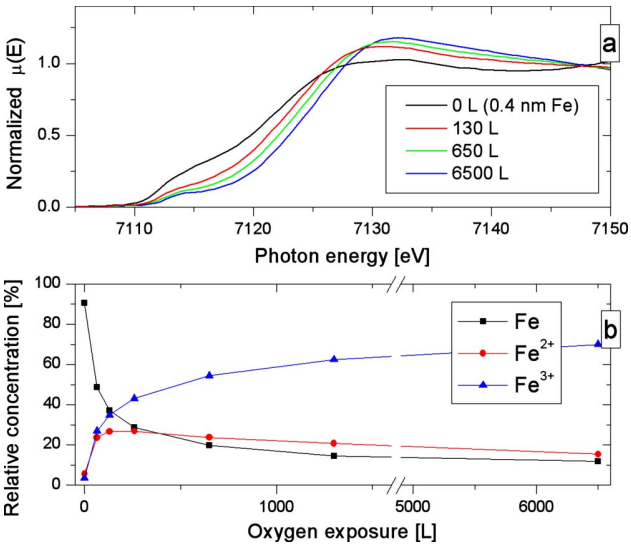

FIG. 10. (Color online) (a) XANES spectra at selected step of the oxidation of a 0.4 nm thick Fe layer. The shift of the edge toward higher energy indicates an increase in the oxidation stage. (b) Relative concentration of the different oxide species as a function of the oxygen exposure. The growth law for Fe^{2+} differs from the general growth law for oxide.

Fig. 8, the geometry of the experiment has to be changed compared to the grazing incidence case. The sample manipulator is now placed horizontally, the incidence angle of the x rays with respect to the sample will therefore be adjusted manually. The load lock is now connected to the chamber through a CF40 gate valve. The sample holding system has been modified to accommodate for the new geometry. In particular only one sample can be placed in the sample magazine. The free CF100 flanges on the top of the chamber enables the use of a special tube equipped with a Be window which allows to bring the external Ge detector (Canberra) as close as 40 mm to the sample surface. The TEY is measured by isolating the sample from the ground and connecting it to a Keithley low current electrometer (Keithley 4517A) using shielded cables and standard safe high voltage feedthrough.

We tested the performance of the two detection systems at the A1 beamline of the DORIS III storage ring (Hamburg, Germany). As a reference layer, we deposited a 30 nm Fe layer onto a Pd coated Si wafer. Both the x-ray appearance near edge structure (XANES) and extended x-ray absorption fine structure (EXAFS) of the Fe *K*-edge (7112 eV) were recorded up to 700 eV above the edge. The normalized spectra are shown in Figs. 9(a) and 9(b). It is directly seen that the TEY provides a much better signal to noise ratio. The result for TEY is remarkable with respect to the small current measured: the background current is around 30 pA and the edge jump is around 300% of this value (5% for a 0.4 nm thick layer). The observed noise in the EXAFS oscillation accounts for a signal stability of few tens of femtoampere. It is a remarkable result in regards of the relatively simple detection scheme used. However, the TEY and FY spectra do not exhibit the same shape. This is especially seen in the EXAFS signal where the oscillation amplitude of the FY is reduced. This behavior is typical for self-absorption effects which seem to be significant even in the case of thin (but dense) films. Proper corrections for self-absorption were done using the algorithm developed by Booth and Bridges[28] which was implemented in the ATHENA analysis software.[29] As can be seen in Figs. 9(c) and 9(d), correction for self-absorption leads to an almost perfect matching of the two signals. This means that both the energy resolved (FY) and energy integrated (TEY) signals provide the same information in the case of thin films. A comparison of both signals should lead to proper correction of self-absorption effect in FY. Due to better statistical quality, the TEY signal should be used whenever energy discrimination is not required.

As a first experiment with this setup, we followed the initial stages of the oxidation process of an ultrathin Fe layer. We deposited a 0.4 nm thick Fe layer onto a Pd coated Si substrate and performed a stepwise oxidation at an oxygen pressure of 1×10^{-5} mbar. The corresponding XANES spectra are shown in Fig. 10(a). Starting with the pure Fe layer, we observe a gradual shift of the edge toward higher energies with increasing oxygen exposure, indicating an increase in the overall oxidation state of the Fe atoms up to saturation at 6500 L. Using a linear combination of reference spectra of the pure oxide compounds, it is possible to extract the relative concentration of each chemical sites. The results are shown in Fig. 10(b). One observes that the growth differs for Fe^{2+} and Fe^{3+} type of sites, especially that Fe^{2+} is created only at the early stage of the oxidation, when the Fe supply is sufficient. A more detailed study of these results will be published elsewhere.[30]

We see that the extreme stability of the TEY signal allows one to record hard x-ray XAS spectra in the monolayer regime, which would become even more advantageous at third generation synchrotron sources. In particular, this opens interesting perspectives for time resolved x-ray absorption studies on thin films growth or interface formation in heterostructures and multilayers.

V. CONCLUSIONS AND PERSPECTIVES

We have described a compact UHV setup which can be used for *in situ* studies via x-ray scattering and spectroscopy. The sample position in the main chamber allows simultaneously performing deposition, ellipsometry measurement,

and grazing incidence x-ray scattering. This offers unique possibilities to study *in situ* thin film growth, magnetic transitions in thin films, cluster growth on surfaces, and interface formation. The instrument described here has enabled us to gain insight into thin film growth processes that would not have been possible otherwise. The possibility to perform XAS with the same deposition setup allows one to look at different aspects of the same system. In the case of the XAS experiment, the development of an efficient TEY detection scheme capable of measuring ultrathin films with good signal stability opens interesting possibilities to perform time resolved XAS studies. The examples presented here demonstrate that both grazing incidence scattering and absorption spectroscopy can be performed in separate experiments. A unique application of this setup would be to combine these techniques in a single experiment on a beamline that combines both techniques. This scheme would, for example, allow direct correlation between density depth profile and chemistry at selected steps of the growth of a multilayer structure. Together with ellipsometry, this scheme can provide a link between optical properties and microscopic properties of surfaces and buried layers, a key role in the development of polymer/metal systems. A future development of the experimental setup will include a complete temperature control of the sample from the frontend GUI, allowing controlled deposition process at elevated temperature.

ACKNOWLEDGMENTS

The authors gratefully acknowledge R. Rüffer and S. Stankov from the ID18 beamline for there help during the NFS experiments as well as E. Welter and D. Zajac from HASYLAB for assistance during the x-ray absorption experiment. This work was supported by the European Commission under FP6 Contract No. NMP4-CT-2003-001516 (DYNASYNC).

[1] S. J. Pearton, F. Ren, A. P. Zhang, and K. P. Lee, Mater. Sci. Eng., R. **30**, 55 (2000).
[2] K. L. Chopra, P. D. Paulson, and V. Dutta, Prog. Photovoltaics **12**, 69 (2004).
[3] S. D. Bader, Rev. Mod. Phys. **78**, 1 (2006).
[4] C. Lamberti, Surf. Sci. Rep. **53**, 1 (2004).
[5] M. Tolan, *X-Ray Scattering from Soft-Matter Thin Films*, Springer Tracts in Modern Physics Vol. 148 (Springer, Berlin, 1999).
[6] R. Röhlsberger, in *Advances in Solid State Physics*, edited by B. Kramer (Springer, Berlin, 2003), Vol. 43, pp. 529–544.
[7] P. Müller-Buschbaum, E. Bauer, E. Maurer, S. V. Roth, R. Gehrke, M. Burghammer, and C. Riekel, J. Appl. Crystallogr. **40**, s341 (2006).
[8] R. Röhlsberger, H. Thomas, K. Schlage, E. Burkel, O. Leupold, and R. Rüffer, Phys. Rev. Lett. **89**, 237201 (2002).
[9] R. L. Headrick, S. Kycia, Y. K. Park, A. R. Woll, and J. D. Brock, Phys. Rev. B **54**, 14686 (1996).
[10] J.-P. Schlomka, M. Tolan, and W. Press, Appl. Phys. Lett. **76**, 2005 (2000).
[11] T.-B. Hur, Y.-H. Hwang, H.-K. Kim, and H.-L. Park, J. Appl. Phys. **96**, 1740 (2004).
[12] Y.-P. Wang, H. Zhou, L. Zhou, R. L. Headrick, A. T. Macrander, and A. S. Özcan, J. Appl. Phys. **101**, 023503 (2007).
[13] L. Peverini, E. Ziegler, T. Bigault, and I. Kozhevnikov, Phys. Rev. B **72**, 045445 (2005).
[14] W. Matz, N. Shell, W. Neumann, J. Bottiger, and J. Chevallier, Rev. Sci. Instrum. **72**, 3344 (2001).
[15] D. Carbone, O. Plantevin, R. Gago, C. Mocuta, O. Bikondoa, A. Alija, L. Petit, H. Djazuli, and T.-H. Metzger, J. Synchrotron Radiat. **15**, 414 (2008).
[16] E. Metwalli, S. Couet, K. Schlage, R. Röhlsberger, V. Körstgens, M. Ruderer, W. Wang, G. Kaune, S. V. Roth, and P. Müller-Buschbaum, Langmuir **24**, 4265 (2008).
[17] T. Nakano and S. Baba, Vacuum **80**, 647 (2006).
[18] M. T. Umlor, Appl. Phys. Lett. **87**, 082505 (2005).
[19] R. M. A. Azzam and N. M. Bashara, *Ellipsometry and Polarized Light* (North-Holland, Amsterdam, 1986).
[20] G. S. D. Beach, F. T. Parker, D. J. Smith, P. A. Crozier, and A. E. Berkowitz, Phys. Rev. Lett. **91**, 267201 (2003).
[21] Th. Diederich, S. Couet, and R. Röhlsberger, Phys. Rev. B **76**, 054401 (2007).
[22] R. Röhlsberger, *Nuclear Condensed Matter Physics with Synchrotron Radiation*, Springer Tracts in Modern Physics Vol. 208 (Springer, Berlin, 2004).
[23] R. Rüffer and A. I. Chumakov, Hyperfine Interact. **97**, 589 (1996).
[24] S.V. Roth, A. Rothkirch, G. Kaune, W. Wang, M.M. Abul Kashem, S. Couet, A. Diehert, R. Gehrke, H. Graafsma, M. Lohmann, E. Metwalli, M. Ruderer, A. Timmann, K. Schlage, R. Röhlsberger, and P. Müller-Buschbaum, HASYLAB Annual Report , 2007.
[25] C. Broennimann, E. F. Eikenberry, B. Henrich, R. Horisberger, G. Huelsen, E. Pohl, B. Schmitt, C. Schulze-Briese, M. Suzuki, T. Tomizaki, H. Toyokawa, and A. Wagner, J. Synchrotron Radiat. **13**, 120 (2006).
[26] L. Tröger, D. Arvanitis, K. Baberschke, H. Michaelis, U. Grimm, and E. Zschech, Phys. Rev. B **46**, 3283 (1992).
[27] A. Erbil, G. S. Cargill III, R. Frahm, and R. F. Boehme, Phys. Rev. B **37**, 2450 (1988).
[28] C. H. Booth and F. Bridges, Phys. Scr., T **115**, 202 (2005).
[29] B. Ravel and M. Newville, J. Synchrotron Radiat. **12**, 537 (2005).
[30] S. Couet, K. Schlage, K. Saksl and R. Röhlsberger, Phys. Rev. Lett. **101**, 056101(2008).

Paper II
Noncollinear coupling of iron layers through native iron oxide spacer layer

Noncollinear coupling of iron layers through native iron oxide spacers

Thomas Diederich, Sebastien Couet, and Ralf Röhlsberger
Hamburger Synchrotronstrahlungslabor (HASYLAB), Deutsches Elektronen-Synchrotron (DESY), Notkestraße 85, 22603 Hamburg, Germany

(Received 21 May 2007; revised manuscript received 4 July 2007; published 1 August 2007)

We have found a magnetic superstructure in multilayers that consist of iron and its native oxide. Employing nuclear resonant scattering of synchrotron radiation from ^{57}Fe probe layers, this manifests as 1/2-order Bragg peaks in the reflectivity curve. From the field dependence of their intensity, we deduce the existence of two magnetic sublattices that are canted by an angle of almost 90° and rotate as one unit in low fields. For higher fields, the two sets of moments gradually align collinear to the external field. This behavior can be explained by a coupling of two adjacent Fe layers that is mediated by an antiferromagnetic order in the oxide spacer between them.

DOI: 10.1103/PhysRevB.76.054401 PACS number(s): 75.70.Cn, 61.10.Kw, 75.25.+z, 76.80.+y

I. INTRODUCTION

The discovery of oscillatory interlayer coupling of ferromagnetic layers through nonmagnetic spacers has initiated a multitude of activities in fundamental and applied research. Meanwhile, also the properties of multilayered systems consisting of directly coupled magnetic layers have found increasing interest due to their rich landscape of magnetic phases.[1] Relatively unexplored systems are heterostructures that are formed of a magnetic material and its native oxide. These layer systems were recently proposed as a new material with high magnetization and low electrical conductivity.[2] The magnetic order, however, that develops in such systems and leads to their remarkable magnetic properties remained rather unexplored.

In this paper, we report on the magnetic structure of polycrystalline multilayers consisting of Fe and its native oxide. Remarkably, we find a magnetic superstructure with an almost orthogonal moment alignment between adjacent Fe layers that are separated by an ultrathin oxide layer. The magnetic structure could be revealed by employing nuclear resonant scattering (NRS) of synchrotron radiation from ultrathin ^{57}Fe probe layers embedded in the layer system.[3–5] Samples are typically illuminated under grazing angles of a few milliradians and the specularly reflected signal is recorded. The magnetic hyperfine interaction renders this technique very sensitive to the magnitude and the direction of magnetic fields at the position of the ^{57}Fe nuclei. These parameters become accessible via the analysis of temporal beat patterns in the reflected signal that is recorded after pulsed excitation by synchrotron radiation. Analyzing this signal as a function of momentum transfer, the method allows one to determine the depth profile of the magnetic moment orientation. For instance, magnetic superstructures in periodic layer systems manifest as additional Bragg peaks that appear between the structural Bragg peaks,[6] similar as in polarized neutron reflectometry.

II. EXPERIMENTS

In this experiment, Fe layers with a thin (0.6 nm) ^{57}Fe probe layer embedded were prepared by dc sputter deposition in a UHV chamber on Si(100) substrates. Native Fe-oxide layers were formed at room temperature via exposure to 6500 L (1 L$=10^{-6}$ Torr s) oxygen at a pressure of about 5×10^{-5} mbar. Under these conditions, a 1.6 nm thick film of Fe oxide forms. Multilayers were then obtained by alternating deposition of Fe and subsequent exposure to oxygen. A terminating Al layer (4 nm) was used for protection against oxidation in *ex situ* experiments.

The experiments have been carried out at the Nuclear Resonance beamline ID18 of the European Synchrotron Radiation Facility (ESRF).[7] A series of time spectra was recorded *in situ* to follow the evolution from a single iron layer over an Fe/Fe-oxide bilayer to a trilayer (Fe[1.7 nm]/Fe oxide[1.6 nm]/Fe[2.5 nm]), as shown in Figs. 1(a)–1(c), respectively. In these measurements, an external field of $\vec{H}=700$ Oe was oriented parallel to the photon wave vector $\vec{k}_0$. The incident angle was kept at $\varphi=0.24°$, which is above the critical angle of Fe ($\varphi_c=0.22°$) and ensures that the whole depth of the sample is probed.

III. RESULTS

The beat pattern in Fig. 1(a) is characteristic for a parallel alignment of the Fe layer magnetization with $\vec{k}_0$, and its period corresponds to a magnetic hyperfine field of 32.6 T at the nuclei. This situation does not change if the Fe layer is oxidized, as shown in Fig. 1(b). Even though the oxide is in very close proximity (0.6 nm apart) to the probing ^{57}Fe layer, neither the magnitude of the hyperfine field nor its orientation is affected. This proves the very sharp boundary between the Fe metal and its native oxide. However, covering this bilayer with another iron layer (with ^{57}Fe embedded) leads to a significant change in the time spectrum as shown in Fig. 1(c). The envelope of the beats is no longer exponential, but the intensity ratios of neighboring peaks exhibit an extra modulation. This can be attributed to a noncollinear alignment of the magnetic hyperfine fields in the two probe layers with the external magnetic field. From the data, one derives a coupling angle between the magnetic moments of these layers of $60°\pm5°$, which is symmetric about the direction of the external field.

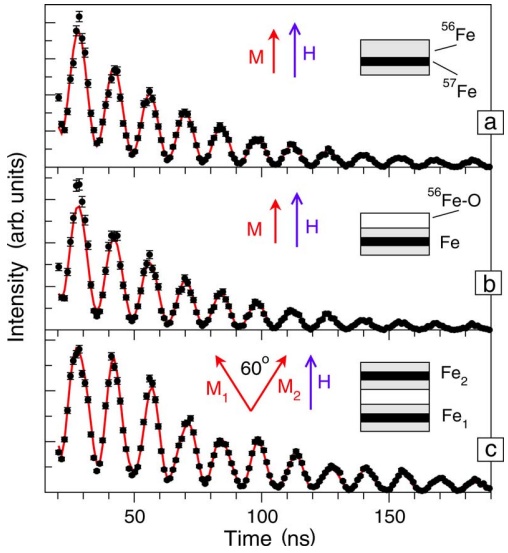

FIG. 1. (Color online) Time spectra of NRS at three different stages of the growth of an Fe/Fe-oxide/Fe trilayer. The solid lines are theoretical simulations from which the magnetization direction in the ^{57}Fe probe layers relative to the external magnetic field of $\vec{H}$=70 mT was deduced. While for a single iron layer the magnetization is parallel to $\vec{H}$, the two magnetic moments in the trilayer are canted by an angle of about 60°.

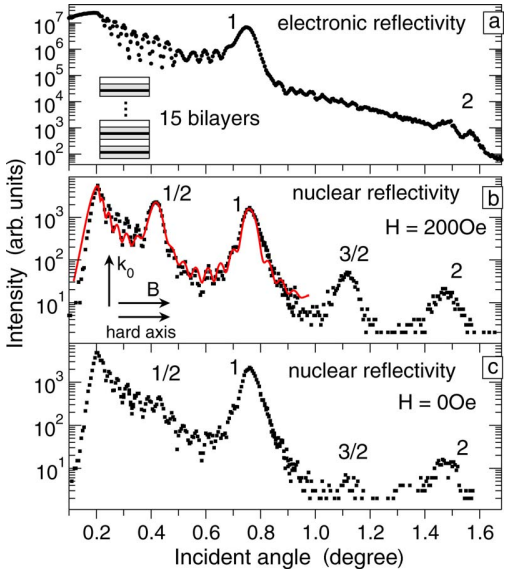

FIG. 2. (Color online) (a) Electronic and [(b) and (c)] nuclear reflectivity curves of the Fe/Fe-oxide multilayer. In the nuclear reflectivity (b), half-order Bragg peaks appear due to a noncollinear arrangement of the magnetic moments in adjacent iron layers. In the scattering geometry used here (arrows), these peaks vanish for zero field (c), proving their pure magnetic origin. The solid line in (b) is a simulation.

Of particular interest now is the evolution of this spin structure with increasing number of bilayers. In order to investigate the long-range order between the moments in the Fe layers, a multilayer stack consisting of 15 bilayers ([Fe(1.7 nm)/Fe oxide(1.6 nm)]) was prepared with the ^{57}Fe layer embedded in the center of every Fe layer. The electronic reflectivity in Fig. 2(a) shows a pronounced first-order Bragg peak, which arises due to the chemical periodicity. From these data, one can determine the thicknesses of the Fe and the Fe oxide that constitute the bilayer with an accuracy of about 0.1 nm. Almost equal thicknesses of the Fe and the Fe-oxide layers lead to a suppression of the second-order peak. For measurement of the nuclear reflectivity (i.e., the time-integrated delayed photons within a time window ranging from 12 to 170 ns after excitation), the sample was aligned with the hard axis of magnetization parallel to the external field and perpendicular to the photon beam direction. The magnetic hard and easy axes were determined via magneto-optical Kerr effect (MOKE) measurements, as shown in Fig. 3(a). The MOKE hysteresis loop for the easy axis is very square with a coercivity of 35 Oe, indicating the soft magnetic properties of this system. This anisotropy was most likely induced by the arrangement of the sputter sources within the chamber, leading to an oblique deposition[8] of the ^{57}Fe, while the atoms from the ^{56}Fe target reached the substrate in normal incidence. Nuclear reflectivity curves of the multilayer are shown in Figs. 2(b) and 2(c). In an external field of $\vec{H}$=200 Oe applied perpendicular to $\vec{k}_0$ (transverse geometry), additional half-order Bragg peaks appear [Fig. 2(b)], indicating a magnetic periodicity that is twice as large as the chemical one. In the case of NRS, these half-order peaks are observed if the projection of the magnetic moments of subsequent Fe layers on the direction of $\vec{k}_0$ is different, as it could be the case for two canted moments. The difference of these projections determines the intensity of the half-order peaks which would reach its maximum value for an antiparallel alignment of the moments along $\vec{k}_0$. In remanence, only a small residue of the half-order peak remains [Fig. 2(c)]. Obviously, a reorientation of the mo-

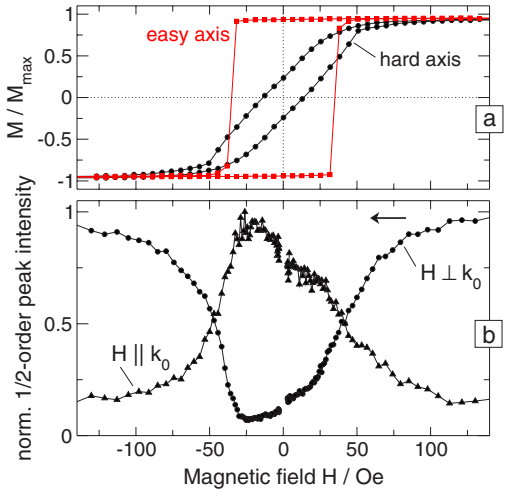

FIG. 3. (Color online) (a) MOKE hysteresis loops for easy and hard axes of the Fe/Fe oxide multilayer. (b) Field dependence of the 1/2-order peak for the magnetic field perpendicular and parallel to the incident photon beam. The hard axis was, in both cases, parallel to the external field.

ments has taken place where the difference in the projections of the moments on the direction of $\vec{k}_0$ vanishes. The half-order peaks also disappear if the sample, together with the external field, is rotated azimuthally by 90°, so that $\vec{H}$ is parallel to $\vec{k}_0$ (longitudinal geometry). These observations prove the purely magnetic origin of the half-order peaks. Moreover, one can conclude that the canting of the successive iron moments must be symmetric around the direction of the external magnetic field. From the simulation of the nuclear reflectivity shown in Fig. 2(b), we derive a canting angle of about 85° between adjacent iron layers.

Monitoring the intensity of the magnetic 1/2-order peak, we investigate the low-field properties and the switching behavior of the coupled iron layer spins. This has been done in longitudinal ($\vec{H} \| \vec{k}$) and transverse ($\vec{H} \perp \vec{k}$) geometries with the hard axis parallel to the external field. The respective curves are presented in Fig. 3(b). In the transverse geometry, the 1/2-order peak intensity drops with decreasing field and reaches again its maximum value after field reversal. This behavior can be attributed to a rotation of the coupled moments as one unit with a fixed canting angle. The minimum position at −30 Oe then corresponds to the coercive field where the magnetic moments are symmetric about $\vec{k}_0$. However, the measured field dependence of the 1/2-order peak intensity could also be explained if the magnetization of the iron layers breaks up into randomly oriented domains in low fields. To rule out this interpretation, we measured the field dependence also in longitudinal geometry. In the case of domain formation, one does not expect any change in the 1/2-order signal with external field. The measured curve, however, clearly shows a pronounced maximum for small field values, confirming the coherent rotation of the canted moments as a single domain. The absence of a domain structure is also supported by the analysis of the diffuse NRS. Its angular distribution does not show any sign of lateral magnetic inhomogeneities that are smaller than the resolution limit of about 60 μm.

With further increasing fields, the 1/2-order peak intensity decreases gradually, as shown in Fig. 4, and reversibly recovers upon releasing the external field back to zero. The inset in Fig. 4 shows the longitudinal magnetization of the sample as determined via MOKE magnetometry. The shape of the curve is in accordance with the model presented here: While the steep rise at low fields is due to the rotation of the effective moment toward the external field, the slow increase toward high fields reflects the gradual alignment of the two coupled moments, very similar to the case of a coupled trilayer as demonstrated in Ref. 9. The pictograms in Fig. 4 summarize the orientation and the relative coupling angle of the two sets of moments in the sample. The field dependence of the coupling angle as derived from the 1/2-order peak intensity is shown in Fig. 6 and will be discussed later.

IV. DISCUSSION

It is clear that the mechanism leading to the observed coupling strongly depends on the properties of the native Fe-oxide layer. In the literature, one finds a lively debate on

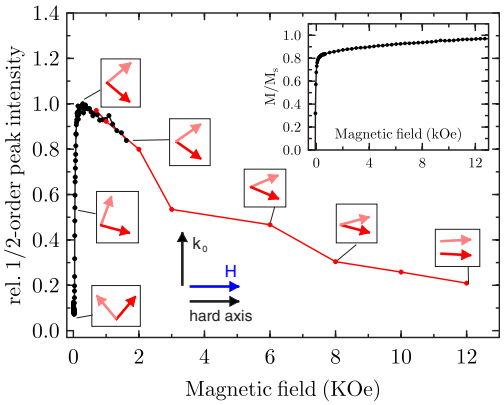

FIG. 4. (Color online) Intensity of the 1/2-order peak as a function of the external magnetic field in a geometry given by the arrows. Pictograms indicate the orientation of the system of coupled moments. The inset shows the positive branch of a longitudinal MOKE magnetization curve of this sample.

the nature of such oxide layers,[10–15] the structure of which is governed by the crystalline orientation of the surface, the temperature, and the oxygen pressure. In our case, the situation is even more complex due to the polycrystalline structure of the Fe metal from which the oxide originates. Recent studies have shown that buried native oxide layers are intrinsically different from any known surface or bulk Fe oxides.[2] These layers appear to be ferromagnetically ordered, consisting of two different components, one carrying no magnetic moment like an antiferromagnet and the other exhibiting ferrimagnetic order with an anomalously high moment. In order to reveal the chemical nature of the oxide, we performed x-ray absorption measurements at the DORIS storage ring (DESY, Hamburg). The normalized absorption coefficient of a 5 nm thick Fe-oxide layer on Si (produced by multiple deposition of Fe and subsequent oxidation) is shown in Fig. 5. The dashed lines are *ab initio* self-consistent multiple scattering calculations of x-ray absorption for FeO and Fe_3O_4 by

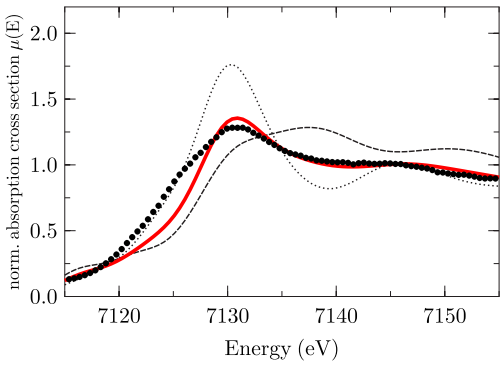

FIG. 5. (Color online) Normalized x-ray absorption coefficient of a 5 nm Fe-oxide layer on Si, produced via multiple deposition of Fe and subsequent oxidation under the same conditions as applied for production of the Fe/Fe-oxide multilayer. The dashed and dotted lines are theoretical calculations for FeO and Fe_3O_4, respectively, based on the FEFF code for x-ray absorption (Ref. 16). The solid red line results from a 1:1 superposition of both calculated curves.

employing the FEFF code.[16] The basic shape of the measured curve is reproduced by assuming a mixture of these oxides in a ratio of roughly 1:1. The contribution of Fe_2O_3 to the measured data seems to be negligible. The remaining deviations in the regime around the absorption edge are most probably due to variations in the chemical state of the oxide in combination with structural disorder that render it to be nonstoichiometric. Although the nature of the oxide is not fully resolved at this stage, these data provide enough evidence to conclude that the oxide contains a significant fraction of antiferromagnetically ordered Fe spins.

These observations lead us to the conclusion that the origin of the magnetic interlayer coupling observed here is most likely a mechanism that was suggested by Slonczewski.[17] In this model, an antiferromagnetic spacer layer mediates the coupling between two ferromagnetic layers via the short-range Heisenberg exchange coupling. Assuming perfectly flat, uncompensated interfaces of the spacer layer, one would obtain either ferromagnetic or antiferromagnetic coupling depending on the number of lattice planes in the spacer layer. Lateral variations of the thickness, however, lead to a competition between ferro- and antiferromagnetic coupling, that results in a noncollinear coupling between the adjacent ferromagnetic layers, as reported previously for coupled trilayers,[9,18,19] Fe/Cr multilayers,[20] and Fe_3O_4/CoO superlattices.[21] The equilibrium configuration is given by the local minima of the magnetic free energy $F=F_c+F_a-\vec{H}\cdot(\vec{M}_1+\vec{M}_2)\,d_{\mathrm{Fe}}$, where F_c is the coupling energy density, F_a is the anisotropy energy density, and the last term describes the Zeeman energy of the coupled moments $\vec{M}_1$ and $\vec{M}_2$ in the external field $\vec{H}$ with d_{Fe} being the thickness of the Fe layers. According to Slonczewski, the coupling energy has the form

$$F_c = C_+\theta^2 + C_-(\theta-\pi)^2, \tag{1}$$

where θ is the angle between the magnetizations of adjacent layers. If the constants C_+ and C_- are of equal magnitude, orthogonal coupling of the moments is favored. This description is in contrast to models that rely on bilinear and/or biquadratic coupling based on RKKY-type interaction between adjacent layers, where the coupling energy is given by

$$F_c = -J_{BL}\cos\theta - J_{BQ}\cos^2\theta, \tag{2}$$

with J_{BL} and J_{BQ} being the constants for bilinear and biquadratic couplings, respectively. Therefore, a fit of the experimental data with these two models should allow us to distinguish between them. In fact, a fit with Eq. (1) (solid line in Fig. 6) leads to a very good agreement with the data. For C_+ and C_-, we obtain the values of 0.122 and 0.086 erg/cm^2, respectively. These values are in the same range as those found for some previously studied trilayer systems.[9,18] On the other hand, the best fit with Eq. (2), shown as a dashed line, significantly deviates from the measured data. This strongly supports the validity of the Slonczewski model in our case.

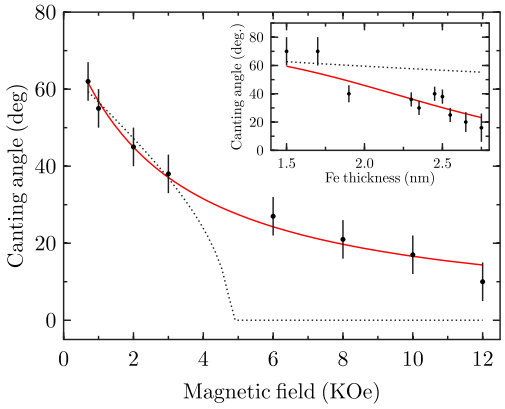

FIG. 6. (Color online) Coupling angle between the two magnetic Fe sublattices in the Fe/Fe-oxide multilayer. The solid line is a fit according to the Slonczewski model, and the dashed line is the best fit obtained assuming bilinear and/or biquadratic coupling. The inset shows the thickness dependence of the coupling angle for an external field of 700 Oe, where the solid line is a visual guide while the dashed line is a calculation according to Eq. (1).

More details about the coupling mechanism could be revealed via the thickness dependence of the magnetic structure. While the Fe-oxide thickness is difficult to control in case of such polycrystalline systems, we have investigated the magnetic coupling here as a function of Fe layer thickness d_{Fe}. The inset of Fig. 6 displays the low-field canting angle as it decreases with increasing d_{Fe}. This dependence cannot be described by the Zeeman term in the magnetic free energy alone, because it leads only to a weak thickness dependence (dashed line). It is clear that the model introduced here has to be refined to take also into account the ferrimagnetic part of the oxide (contributed by the Fe_3O_4) that participates in the coupling. For that reason, the microscopic structure of the native oxide layers still has to be explored.

In conclusion, using NRS, we were able to directly observe a noncollinear coupling of polycrystalline iron layers through a native oxide spacer. This coupling seems to be mediated by antiferromagnetically ordered components in the oxide. The canting angle between adjacent layers is close to 90° as observed before for some single-crystalline systems. Remarkably, the coupling persists over a large number of Fe/Fe-oxide bilayers, giving rise to a long-range magnetic correlation in a multilayer that is stable up to rather high fields beyond 12 kOe. This easy-to-prepare system may open interesting perspectives for applications in magnetoengineering and related fields.

ACKNOWLEDGMENTS

Sincere thanks go to R. Rüffer, S. Stankov, K. Schlage, and T. Klein for their assistance during the experiments at ESRF, to K. Saksl, E. Welter, and O. Seeck for their support at HASYLAB, and to J. Korecki for helpful discussions. We gratefully acknowledge K. Saksl for providing the FEFF calculations for the Fe oxides. This work was supported by the European Commission under FP6 Contract No. NMP4-CT-2003-001516 (DYNASYNC).

[1] R. E. Camley and R. L. Stamps, J. Phys.: Condens. Matter **5**, 3727 (1993).
[2] G. S. D. Beach, F. T. Parker, D. J. Smith, P. A. Crozier, and A. E. Berkowitz, Phys. Rev. Lett. **91**, 267201 (2003).
[3] L. Niesen, A. Mugarza, M. F. Rosu, R. Coehoorn, R. M. Jungblut, F. Roozeboom, A. Q. R. Baron, A. I. Chumakov, and R. Rüffer, Phys. Rev. B **58**, 8590 (1998).
[4] C. L'abbé, J. Meersschaut, W. Sturhahn, J. S. Jiang, T. S. Toellner, E. E. Alp, and S. D. Bader, Phys. Rev. Lett. **93**, 037201 (2004).
[5] R. Röhlsberger, H. Thomas, K. Schlage, E. Burkel, O. Leupold, and R. Rüffer, Phys. Rev. Lett. **89**, 237201 (2002).
[6] T. S. Toellner, W. Sturhahn, R. Röhlsberger, E. E. Alp, C. H. Sowers, and E. E. Fullerton, Phys. Rev. Lett. **74**, 3475 (1995).
[7] R. Rüffer and A. I. Chumakov, Hyperfine Interact. **97/98**, 589 (1996).
[8] M. T. Umlor, Appl. Phys. Lett. **87**, 082505 (2005).
[9] P. A. A. van der Heijden, C. H. W. Swüste, W. J. M. de Jonge, J. M. Gaines, J. T. W. M. van Eemeren, and K. M. Schep, Phys. Rev. Lett. **82**, 1020 (1999).
[10] G. W. R. Leibbrandt, G. Hoogers, and F. H. P. M. Habraken, Phys. Rev. Lett. **68**, 1947 (1992).
[11] S. J. Roosendaal, A. M. Vredenberg, and F. H. P. M. Habraken, Phys. Rev. Lett. **84**, 3366 (2000).
[12] H.-J. Kim, J.-H. Park, and E. Vescovo, Phys. Rev. B **61**, 15288 (2000).
[13] K. Mori, M. Yamazaki, T. Hiraki, H. Matsuyama, and K. Koike, Phys. Rev. B **72**, 014418 (2005).
[14] K. Mori, M. Yamazaki, T. Hiraki, H. Matsuyama, and K. Koike, Phys. Rev. B **74**, 026405 (2006).
[15] E. Vescovo, Phys. Rev. B **74**, 026406 (2006).
[16] A. L. Ankudinov, B. Ravel, J. J. Rehr, and S. D. Conradson, Phys. Rev. B **58**, 7565 (1998).
[17] J. C. Slonczewski, J. Magn. Magn. Mater. **150**, 13 (1995).
[18] M. E. Filipkowski, J. J. Krebs, G. A. Prinz, and C. J. Gutierrez, Phys. Rev. Lett. **75**, 1847 (1995).
[19] C.-H. Lai and K. H. Lu, J. Appl. Phys. **93**, 8412 (2003).
[20] A. Schreyer, J. F. Ankner, Th. Zeidler, H. Zabel, C. F. Majkrzak, M. Schäfer, and P. Grünberg, Europhys. Lett. **32**, 595 (1995).
[21] Y. Ijiri, J. A. Borchers, R. W. Erwin, S.-H. Lee, P. J. van der Zaag, and R. M. Wolf, J. Appl. Phys. **83**, 6882 (1998).

Paper III
How metallic Fe controls the composition of its native oxide

How Metallic Fe Controls the Composition of its Native Oxide

Sebastien Couet,[1,*] Kai Schlage,[1] Karel Saksl,[2] and Ralf Röhlsberger[1]

[1]*Deutsches Elektronen Synchrotron (DESY), Notkestraße 85, 22603 Hamburg, Germany*

[2]*Institute of Materials Research, Slovak Academy of Sciences, Watsonova 47, 04353 Kosice, Slovak Republic*

(Received 18 April 2008; published 1 August 2008)

We have studied *in situ* the oxidation of ultrathin iron layers and monitored the chemical changes induced by subsequent deposition of Fe metal using hard x-ray absorption spectroscopy. The site sensitivity of the technique allows us to quantify the composition of the layer throughout the oxidation or deposition process. It is found that the thin native oxide incorporates a significant fraction of Fe atoms remaining in a metallic configuration even in the saturated state. Subsequent deposition of Fe leads to a complete reduction of the oxide that adopts an FeO-like structure containing Fe^{2+} sites only.

DOI: 10.1103/PhysRevLett.101.056101 PACS numbers: 81.15.−z, 61.05.cj, 81.16.Pr

In recent years, intensive research has been conducted on transition metal oxide compounds, thin films, and multilayers due to their potential use as building blocks in magnetic structures like spin valves and magnetic tunnel junctions (for a review, see [1] and references therein). Recently, metal–native-oxide multilayers (MNOM, produced by metal deposition and subsequent oxygen exposure) have been proposed as new compounds combining high magnetization and low conductivity [2]. In these systems, the buried oxide possesses magnetic properties that strongly deviate from any bulk iron oxide phase [2,3]. However, the influence of the surrounding metal on the structure of the oxide is not yet identified and prevents clear understanding of the observed magnetic properties of MNOM systems.

The oxidation of iron itself has been extensively studied in the past decades. Studies performed on polycrystalline [4] as well as on single crystalline [5] surfaces have shown that the oxidation of iron can be understood in the framework of the coupled current mechanism introduced by Fromhold and Cook more than 50 years ago [6]. While those experiments explain very well the observed growth *kinetics*, the actual *composition* of the native oxide is still a matter of debate and is obviously highly dependent on preparation parameters like temperature and surface orientation ([7–11] and references therein). X-ray absorption spectroscopy at the L edges was recently used to characterize the extent of oxidation or reduction processes arising at the interface between Fe and other transition metal oxides (CoO and NiO) [12]. Remarkably, the interaction of Fe with its own oxide phases was never quantitatively studied before.

In this Letter, we present a quantitative x-ray absorption spectroscopy (XAS) study of the oxidation of ultrathin iron layers and the changes induced by subsequent coverage with Fe. The sensitivity of the XAS signal to the oxidation state and the local environment of the absorbing atom is used to follow the evolution of the oxide's structure in a quantitative and site specific manner. The use of ultrathin layers (in contrast to other studies which used thick substrates [4,5,7–9]) allows one to directly resolve the intrinsic composition of the growing oxide and disentangle the influence of the substrate.

The experiment was performed *in situ* in a compact UHV deposition chamber (base pressure 1×10^{-9} mbar) mounted on the A1 beam line of the DORIS III storage ring (DESY, Hamburg). The Fe K-edge absorption signal was recorded by measure of the total electron yield and fluorescence yield. Polycrystalline layers were grown by dc magnetron sputtering (Ar pressure 5×10^{-3} mbar) on superpolished Si(001) substrates. Prior to the Fe deposition, a 6 nm thick Pd buffer layer was deposited to avoid unwanted oxidation at the SiO_2/Fe interface. Iron layers, with thicknesses ranging from 0.4 to 2 nm, were then deposited, stepwise oxidized to saturation (oxygen pressure 1×10^{-5} mbar), and subsequently covered with a second Fe layer. Both the near edge (XANES) and the extended fine structure (EXAFS) spectra of the Fe K edge were recorded (30 min acquisition time) at selected steps of the preparation. The influence of the residual gas pressure was checked by repeated XAS scans on a 0.8 nm thick metallic Fe layer, showing no detectable changes over several hours.

The different bulk iron oxide phases can be described as a combination of three different Fe sites distributed over interstitial positions in a close packed fcc oxygen lattice [13]. For quantitative XANES analysis, we used bulk iron oxide reference samples of FeO (single crystal, Mateck GmbH, Germany), Fe_3O_4 and γ-Fe_2O_3 (both are powders diluted in a polyethylene matrix). As we do not expect that the oxidized layer adopts a long range crystalline ordering, the three bulk oxide references will rather be used to obtain the site specific concentration of Fe^{2+}_{oct}, Fe^{3+}_{tet}, and Fe^{3+}_{oct} in the layer. The subscripts "tet" and "oct" refer to ions in tetrahedral or octahedral positions.

Figure 1(b) shows the XANES spectra illustrating the stepwise oxidation of a 0.8 nm thick Fe layer. With increasing oxygen exposure, the onset of the absorption edge shifts to higher energies, indicating an increase of the overall oxidation state. Above 1300 L (1 L $= 10^{-6}$ Torr s), the saturation regime is reached and only little changes are still visible towards 6500 L. To quantify the composition of the

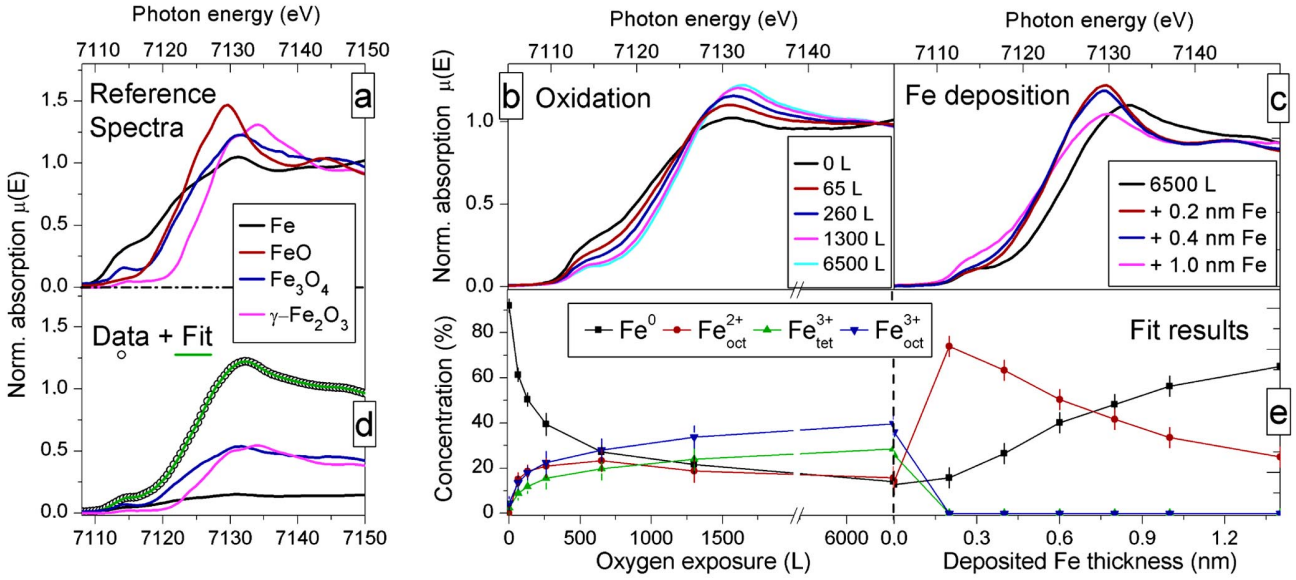

FIG. 1 (color online). (a) Fe K-edge XANES spectra of reference samples for Fe, FeO, Fe_3O_4, and γ-Fe_2O_3. (b) Evolution of the absorption edge position and shape for a 0.8 nm Fe layer exposed to an increasing amount of oxygen. (c) Evolution of the spectrum upon coverage of the saturated oxide by Fe. (d) Least square fitting of the saturated oxide spectra using a linear combination of reference spectra. (e) Evolution of the relative concentration of the different chemical sites as a function of oxygen exposure (left) and as a function of the Fe coverage on top of the saturated oxide (right).

layer, we fitted the spectrum of the oxidizing layer with a linear combination of the reference spectra. A fit of the saturated oxide, along with the contributions of the different references, is displayed in Fig. 1(d). Quantitative results are shown in the left-hand panel of Fig. 1(e). At low exposures, Fe^{2+}_{oct} and Fe^{3+}_{oct} sites are created in equal quantities. Above 250 L, the formation of Fe^{2+}_{oct} is hindered due to the reduced availability of Fe atoms at the surface while the number of Fe^{3+}_{oct} and Fe^{3+}_{tet} sites continues to grow. It is important to note that the oxide composition never corresponds to a stoichiometric bulk oxide. In principle, this could correspond to the formation of different stoichiometric oxides at crystallites exposing differently oriented surfaces to the oxygen. Grazing incidence x-ray diffraction measurements from a multilayered Fe/oxide sample indicated a lateral grain size of 10 nm for the 1.5 nm thick metal layers. No sign of crystalline structure was found for the oxide layers. We therefore expect that the oxidation does not lead in this case to stoichiometric oxide. The oxidation procedure was performed with Fe layer thicknesses ranging from 0.4 to 2 nm. In each case, the oxidation curve follows a similar evolution as in Fig. 1(e). This indicates that the influence of an eventual nonuniformity of the initial Fe layers plays a minor role in the conclusions developed here.

Several studies on iron oxidation at room temperature (RT) reported the possible presence of metallic Fe in the oxide layer [2,5,9], without being able to disentangle the influence of the thick Fe substrate on the origin of the signal. The use of ultrathin Fe layers allows us to address this question in a more quantitative manner. In Fig. 1(e), we see that the concentration of Fe metal is not zero in saturation, although one would expect the layer to be completely oxidized, as reported in Ref. [2]. Figure 2 shows the evolution of the Fe^0 concentration in the saturated (6500 L) oxide as a function of the initial Fe layer thickness. The Fe^0 concentration remains around 12% (a constant fraction of the total Fe content) for all Fe thicknesses below 0.8 nm, even for exposures as high as 25 000 L. Above 0.8 nm, the proportion of metallic Fe increases almost linearly, indicating that a metallic layer remains below the oxide in the thicker layer. We can therefore expect that the metallic signal observed for the thin layers originates from Fe atoms which are still in a metallic environment and distributed throughout the oxide. While it is difficult to address the exact origin of this phenomenon, these measurements give new insight in the

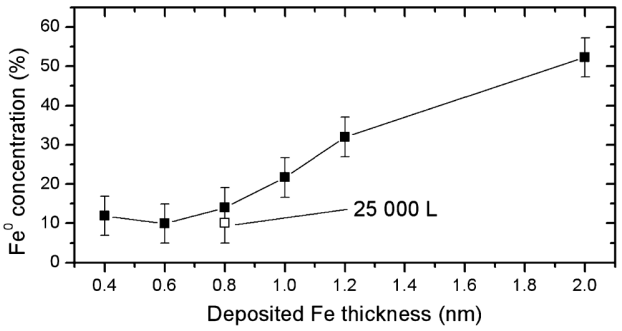

FIG. 2. Evolution of the Fe^0 concentration in the saturated (6500 L) oxide as a function of the initial Fe layer thickness.

previously reported possible presence of metallic Fe in an oxidized layer. These considerations should be taken into account when discussing the structure of such oxide.

As discussed by Beach *et al.* [2], buried native iron oxide layers (i.e., Fe oxidized at RT and covered with Fe) possess structural and magnetic properties different from any bulk iron oxide phase, like a higher density and an anomalously high magnetic moment per atom. However, they were not able to relate the initial structure of the free oxide to the observed properties of the buried oxide. These questions can be directly addressed here by performing stepwise Fe deposition on top of the saturated oxide and analyzing the near edge structure of the x-ray absorption signal. The corresponding XANES spectra are shown in Fig. 1(c). Starting with the saturated native oxide, a drastic change of the spectrum occurs upon coverage with only 0.2 nm of Fe. The profile obtained differs from what was observed during the oxidation and indicates a fundamental change of the Fe's chemical environment. The result of the fitting procedure is shown in the right-hand panel of Fig. 1(e). The change is attributed to a reduction of the native oxide to an FeO-like structure where only Fe^{2+}_{oct} sites are present. This was observed for every initial Fe layer thicknesses. In contrast to the free native oxide which exhibits a mixture of several different chemical environments the buried native oxide adopts a well-defined composition made of Fe^{2+}_{oct} sites only (plus the original Fe^0 content).

The fact that the 1.5 nm thick oxide layer is reduced to an FeO-like environment is remarkable. It implies that the Fe deposited on top of the layer can effectively diffuse to distances larger than 1 nm from the interface. At room temperature, thermal diffusion of cations is negligible and additional driving mechanisms are therefore expected to induce the diffusion. During the oxidation, the difference in the work functions of the metal and the oxygen O^- level leads to the appearance of a potential $V_M = \phi_o - \phi_m$ (the Mott potential [6]) across the oxide that induces a sufficiently large electric field to promote the cation diffusion through the oxide, as shown in Fig. 3(a). When the oxygen supply is shut off [Fig. 3(b)], V_M disappears and only a residual electric field is present at the metal-oxide interface due to the space charges built up in the oxide [14]. Deposition of Fe on top of the saturated oxide results in a reduction of the first Fe^{3+} monolayer to Fe^{2+} (this process does not require cations transport). In the case of an ultrathin metal adsorbate like here, the space charges appearing at the new oxide-metal interface leads to a net charge on the metal overlayer. A strong electric field is created at the interface which promotes the diffusion of ions. It should be noted that the process of Fe-oxide reduction is not an artifact of the stepwise deposition of Fe described above but occurs also for deposition of thicker Fe layers in one step.

From the chemical point of view, only one type of coordination site exists in the buried oxide. However, the

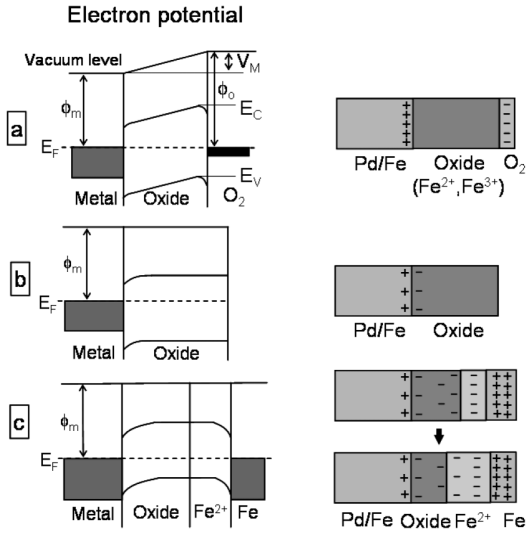

FIG. 3. Electron energy diagram (left-hand panels) and net charge distribution (right-hand panels) at different stages of the oxidation or reduction. E_F is the Fermi level. ϕ_m and ϕ_o are the metal and O^- level work functions, respectively. E_C and E_V are the energy levels of the conduction and valence band of the oxide, respectively. (a) Oxidation. The Mott potential $V_M = \phi_o - \phi_m$ appears across the oxide layer, promoting the cation diffusion. (b) When the oxygen supply is shut off, the system is in equilibrium and only a small residual electric field is present at the metal-oxide interface due to the induced space charge in the oxide. (c) After deposition of Fe. The space charge in the oxide induces a net charge on the ultrathin Fe adsorbate which promote the Fe diffusion in the oxide. The right-hand inset shows the progressive growth of the Fe^{2+} layer.

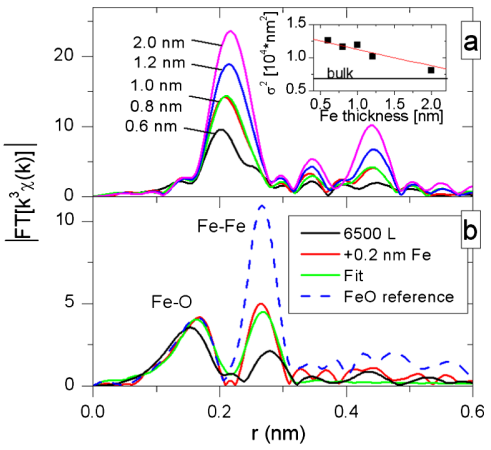

FIG. 4 (color online). (a) Fourier transform (FT) modules in the r space of the EXAFS signal of unoxidized Fe layers of different thickness. The inset shows the evolution of the mean square displacement σ^2 of the first coordination shell. (b) FT of the EXAFS signal for the saturated native oxide (6500 L) and subsequent coverage with 0.2 nm Fe (+ 0.2 nm Fe). The fitted radial distribution of the latter was obtained by fitting the filtered EXAFS signal constrained to the first two subshells ($r <$ 0.3 nm). For comparison, a FeO reference for bulk FeO is given (dashed line).

oxidation and reduction processes involve diffusion of cations through the oxide, which implies a modification of the structural quality of the lattice. To investigate the structural changes that take place during the oxidation process, we used the EXAFS part of the absorption signal, which is sensitive to the local order (i.e., nearest neighbor distance, coordination numbers) of the absorbing atoms. Figure 4(a) shows the Fourier transform of the EXAFS signal for different thicknesses of the initial, nonoxidized Fe layer. The intensity of the first coordination shell peak gradually increases with increasing layer thickness. Values of the mean square displacement σ^2 shown in the inset were extracted from the EXAFS fit procedure by fixing the total number of atoms N in the first shell to 14 (bulk value for bcc Fe). While the values found for the thinnest layers are typical for highly disordered systems, σ^2 gradually decreases and almost reaches the bulk value of polycrystalline Fe for the 2 nm thick layer. The linear dependence of σ^2 on the initial amount of Fe deposited documents a smooth transition from ultrathin to thin films. This supports our interpretation that even the 0.4 nm thick layer behaves essentially as a continuous Fe layer. Figure 4(b) shows the Fourier transform modules of the EXAFS signal for the saturated oxide, for the reduced layer, and for the pure FeO reference sample. The Fe-O (first nearest neighbor) peak for the reduced oxide layer matches the profile of the FeO reference, indicating that each Fe atom has the same direct environment as FeO. However, the lower intensity of the Fe-Fe peak compared to FeO points to a rather disordered structure. In fact, the results indicate a large σ^2 of 0.0165 Å^2. This value is 2 times larger than the value related to thermal vibration observed in Fe_3O_4 at room temperature [15], indicating a high degree of static disorder. In that sense, we see that deposition of Fe on top of a free native oxide leads to the formation of a layer with a well-defined local order that is comparable to that of bulk FeO, but with a larger degree of structural disorder.

In summary, we have quantitatively studied the chemical change occurring during the oxidation of Fe layers as well as during the deposition of Fe on such oxide. The use of ultrathin layers combined with the site specificity of x-ray absorption allowed us to quantitatively resolve the composition of the oxide at all stages of the oxidation or reduction process. We evidenced the presence of metallic Fe as a constituent of ultrathin iron layers that were oxidized at room temperature. Deposition of Fe on top of the multicomponent oxide leads to a reduction of this layer resulting in a single type of Fe^{2+}_{oct} sites arranged in an FeO-like structure. These findings bring new insight into the previously reported properties of buried native iron oxides. The higher density and the higher magnetic moment per atom that was reported by Beach *et al.* [2] can be partly accounted for by the presence of metallic Fe in the layer. The fact that the native oxide covered with Fe exhibits a unique FeO-like structure raises new questions regarding magnetic ordering. In particular, the RT magnetic order observed recently [2,3] implies that the ordering temperature of the buried native oxide is much increased compared to the bulk Néel temperature of FeO ($T_N = 198$ K). Understanding how the complex magnetic structure of such ultrathin oxide layers influence the electronic transport in Fe/FeO multilayers might open interesting possibilities for spin electronic applications.

The results of this study are expected to be valid not only for iron, but apply to any metal with several coexisting oxidation states. This means that the coverage of a native metal oxide with the pure metal reduces the oxide to its lowest oxidation state and stabilizes it. The deposition procedure described here thus represents a simple way to obtain metal–metal-oxide heterostructures with unique electronic and magnetic properties.

The authors gratefully acknowledge E. Welter and D. Zajac for their help during the measurements at HASYLAB as well as Th. Diederich for his support. K. Saksl is indebted to the Slovak Grant Agency for Science for financial support (Grant No. 2/7196/27).

*Author to whom correspondence should be addressed.
sebastien.couet@desy.de

[1] M. Finazzi, L. Duó, and F. Ciccacci, Surf. Sci. Rep. **62**, 337 (2007).
[2] G. S. D. Beach, F. T. Parker, D. J. Smith, P. A. Crozier, and A. E. Berkowitz, Phys. Rev. Lett. **91**, 267201 (2003).
[3] Th. Diederich, S. Couet, and R. Röhlsberger, Phys. Rev. B **76**, 054401 (2007).
[4] P. C. J. Graat, M. A. J. Somers, A. M. Vredenberg, and E. J. Mittemeijer, J. Appl. Phys. **82**, 1416 (1997).
[5] S. J. Roosendaal, A. M. Vredenberg, and F. H. P. M. Habraken, Phys. Rev. Lett. **84**, 3366 (2000).
[6] A. T. Fromhold and E. L. Cook, Phys. Rev. **163**, 650 (1967).
[7] H.-J. Kim, J.-H. Park, and E. Vescovo, Phys. Rev. B **61**, 15 284 (2000).
[8] K. Mori, M. Yamazaki, T. Hiraki, H. Matsuyama, and K. Koike, Phys. Rev. B **72**, 014418 (2005).
[9] S. J. Roosendaal, B. van Asselen, J. W. Elsenaar, A. M. Vredenberg, and F. H. P. M. Habraken, Surf. Sci. **442**, 329 (1999).
[10] M. W. Ruckman, J. Chen, M. Strongin, and E. Horache, Phys. Rev. B **45**, 14 273 (1992).
[11] G. Bhargava, I. Gouzman, C. M. Chun, T. A. Ramanarayanan, and S. L. Bernasek, Appl. Surf. Sci. **253**, 4322 (2007).
[12] T. J. Regan, H. Ohldag, C. Stamm, F. Nolting, J. Lüning, J. Stöhr, and R. L. White, Phys. Rev. B **64**, 214422 (2001).
[13] D. V. Dimitrov, K. Unruh, G. C. Hadjipanayis, V. Papaefthymiou, and A. Simopoulos, Phys. Rev. B **59**, 14 499 (1999).
[14] Q. Fu and T. Wagner, Surf. Sci. Rep. **62**, 431 (2007).
[15] B. A. Wechsler, D. H. Lindsley, and C. T. Prewitt, Am. Mineral. **69**, 754 (1984).

Paper IV
The magnetic structure of coupled Fe/FeO multilayers revealed by nuclear resonant and neutron scattering methods

The magnetic structure of coupled Fe/FeO multilayers revealed by nuclear resonant and neutron scattering methods

S Couet[1], K Schlage[1], Th Diederich[1],R Rüffer[2], K Theis-Bröhl[3], K Zhernenkov[4], B P Toperverg[3,5], H Zabel[3] and R Röhlsberger[1]

[1]Deutsches Elektronen-Synchrotron (DESY), Notkestraße 85, 22603 Hamburg, Germany

[2]European Synchrotron Radiation Facility (ESRF), 38043 Grenoble, France

[3]Ruhr Univ Bochum, Dept Phys, 44780 Bochum, Germany

[4]Institute Max Von Laue Paul Langevin, 38042 Grenoble, France

[5]Petersburg Nuclear Physics Institute, 188300 Gatchina, Russia

E-mail: `sebastien.couet@desy.de`

Abstract. We have studied the magnetic structure that forms in a Fe/native Fe oxide multilayer by nuclear resonant scattering of synchrotron radiation and polarized neutron reflectometry. Magnetic field dependent experiments revealed a non collinear magnetic arrangement of the adjacent metallic layer which is mediated by an antiferromagnetically ordered oxide layer. Despite its antiferromagnetic (AFM) order, the oxide presents a small net magnetization attributed to the presence of metallic Fe clusters within the AFM matrix which align parallel with the external field. The presence of a strong uniaxial anisotropy prevents the system to form small magnetic domains in remanence. Rather the canting remains close to 90° throughout the magnetization reversal on the hard axis. The results and the influence of the uniaxial anisotropy are discussed in the framework of the proximity magnetism model.

1. Introduction

The discovery of an antiferromagnetic coupling between ferromagnetic (FM) layers separated by metallic spacer layers has triggered a multitude of activities in fundamental and applied research. This, for example, led to the development of giant magneto resistive read heads which are now widely used in the hard disk technology. This interlayer spin coupling is fairly well understood in terms of the RKKY model, which implies long range exchange interaction mediated by conducting band electrons in the spacer layer [1, 2]. Transition metal monoxides (TMO) like CoO or NiO have recently attracted special interest to be used as spacer layer [3, 4] due to their unique magnetic and electric properties. They possess an antiferromagnetic (AFM) ground state combined with a low conductivity which prevents long range RKKY-type exchange interactions. Instead, their magnetic coupling properties are mainly ruled by the interfacial exchange interaction between metallic FM and insulating AFM layers. This means that the interface of the TMO with the FM layers plays a determining role to the overall magnetic coupling. A FM/AFM interface is also the basic requirement for the appearance of the well known exchange bias effect [5] where an unidirectional anisotropy is induced in the coupled FM, an effect which is characterized by an increased coercitivity and a shift of the hysteresis loop. The presence of many FM/AFM interfaces in a TM/TMO layer stack could lead to a combination of long interlayer magnetic ordering and exchange bias phenomena, which has not been extensively studied so far.

In a recent study, Beach et al. [6] proposed to use natively grown oxide layers (*i.e.* oxide layers grown by exposure to oxygen) to form metal/native oxide multilayers (MNOM) combining a large magnetic moment with a low conductivity. These two properties render this type of multilayers ideal candidates for high frequency magnetic applications for their ability to efficiently damp eddy currents while maintaining a high net magnetization. Recently, we reported on the occurrence of non-collinear magnetic coupling between adjacent Fe layers in similar Fe/native oxide systems [7]. The magnetic field dependence of the spin arrangement pointed towards a proximity magnetism coupling model [2] which implies an AFM order of the buried native oxide. However, the microscopic spin arrangement of both the metal and the oxide layers has not yet been resolved and prevents a complete understanding of the observed magnetic properties of these systems.

Element specific X-ray scattering methods based on magnetic dichroism effects (*e.g.* XMCD, XMLD) [8, 9] are difficult to apply in this case to obtain layer resolved information because the magnetic atom (Fe) is present in both the metal and the oxide layer. On the other hand, isotope sensitive scattering methods like nuclear forward scattering of synchrotron radiation (NFS) and polarized neutron reflectometry (PNR) can provide a large nuclear contrast and a sub nm depth resolution [10] if isotopic probe layers (^{56}Fe,^{57}Fe) are embedded into the layer system.

In this study, we combined the two methods of nuclear forward scattering and polarized neutron reflectometry to study the microscopic magnetic structure of

isotopically enriched Fe/native oxide superlattices. The use of isotopic ^{57}Fe probe layers placed either in the metallic or in the oxide part of the system allowed to study *independently* the magnetic structure of each set of layers by NFS. PNR was applied to obtain the magnetic contrast between the metal and the oxide, ideally complementing the NFS results.

2. Sample characterization

Two different types of superlattices were prepared that are depicted in Figs. 1a and b. The first one with a 0.6 nm ^{57}Fe probe layer placed in the middle of the metallic ^{56}Fe layer will be referenced as the *metal doped* sample. The second one has an ^{57}Fe-oxide probe layer embedded in the oxide part of the system and will be referenced has the *oxide doped* sample. The samples were prepared by DC magnetron sputter deposition in a UHV chamber (base pressure 5×10^{-10} mbar) described in detail elsewhere [11]. The Fe/native oxide superlattices were grown on superpolished Si(100) substrates by deposition of a 2 to 3 nm thick Fe layer and subsequent controlled exposure to 6500 Langmuir (1 L=10^{-6}mbar×s) of molecular oxygen. This sequence is then repeated to produce a superlattice of 15 bilayers. A final 3 nm Al capping layer is deposited to prevent further oxidation of the samples in air. The nominal structure of the samples is Si/[Fe(1.8nm)/FeO_x(1.6nm)]$_{15}$/Al(3nm). In [12], the chemical structure of the buried native oxide was investigated by *in-situ* X-ray absorption spectroscopy which showed that the layer adopts a disordered but pure FeO like structure upon deposition of the metal on top of the saturated oxide.

The oblique incidence of the sputtered ^{57}Fe atoms with respect to the sample surface leads to a strong uniaxial anisotropy due to preferential alignment of polycrystalline columns during the growth process [13]. The low-field hysteresis curves along the easy and hard axis, as recorded by MOKE magnetometry, are shown on Fig. 1c. The inset shows the progressive increase of the net magnetization in high fields which saturates only above 1.2 T, as reported in [7].

3. Experimental methods

As will be shown later, Fe/FeO_x multilayers exhibit a complex magnetic structure where both the metal and the oxide are magnetically ordered. The two scattering methods that we employed will yield complementary information. NFS is used as a layer selective probe to study *separately* the metal or the oxide part of the system while PNR will provide the contrast *between* adjacent metal/oxide layers.

Nuclear forward scattering of synchrotron radiation is a time resolved method where the time dependent de-excitation of ^{57}Fe nuclei in the sample is recorded after pulsed excitation by a synchrotron radiation source. Because this de-excitation occurs on the nanosecond timescale, the signal from the ^{57}Fe probe layer can be isolated from the electronic charge scattering (which occurs on the fs timescale) using fast avalanche

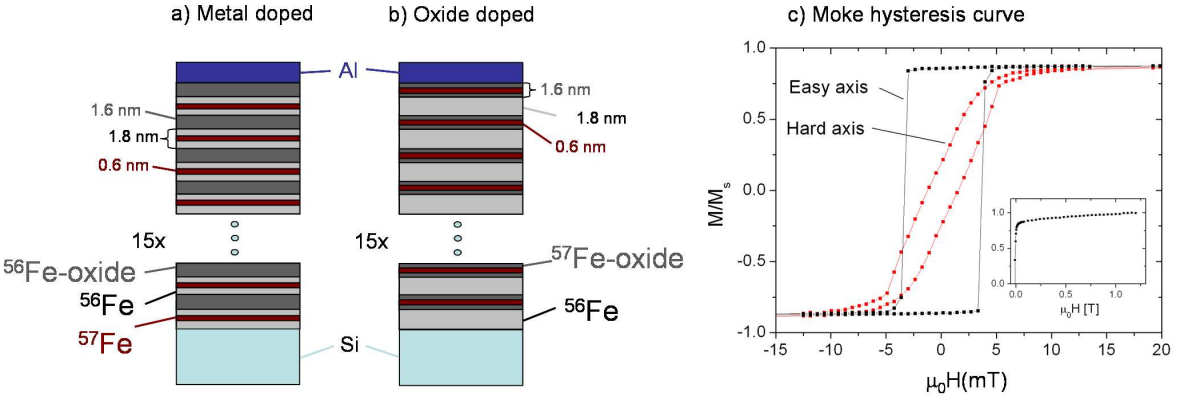

Figure 1. Schematic sample structure for (a) the metal doped and (b) the oxide doped sample. A 0.6 nm ^{57}Fe probe layer is embedded in each metal (a) or oxide (b) layers of the superlattices. c) Typical easy and hard axis hysteresis curve of these systems. An uniaxial anisotropy is induced by the oblique deposition of the ^{57}Fe with respect to the sample surface. The inset shows the high field branch of the hysteresis, which exhibit a slow increase of the net magnetization with increasing field. Saturation is reached only above 1.2 T.

photodiode (APD) detectors [14]. The recorded signal is therefore intrinsically free of charge scattering background. The sensitivity to the hyperfine structure of the nucleus renders the techniques highly sensitive to the magnitude and orientation of the magnetic field at the position of the ^{57}Fe nuclei. The advantage of the technique here comes from the possibility to selectively probe the magnetic structure of the metal or the oxide by placing ultrathin ^{57}Fe probe layers in these parts. The sample is typically illuminated in grazing incidence geometry and the specularly reflected signal is recorded. If this signal is recorded as a function of the momentum transfer (nuclear resonant reflectivity), one can obtain the magnetic depth profile of the ^{57}Fe in the system. In particular, periodic magnetic structure cause a variation of the nuclear scattering amplitude that leads to superstructure peaks between the structural Bragg peaks in the nuclear reflectivity.

Polarized neutron reflectometry shares some of the formalism of magnetic X-ray scattering. However, as a nuclear scattering technique, PNR can provide large scattering contrast even for different isotopes of the same element (further details on the PNR method can be found in Ref [15, 16]). In ours case the large difference in the nuclear scattering length density between ^{56}Fe and ^{57}Fe (8.36×10^{-6}Å^{-2} and 1.9×10^{-6}Å^{-2}, respectively) allows to vary the nuclear contrast in the multilayer structure [17]. The magnetic scattering length is on the other hand due to the interaction of neutrons with the magnetic moment of the atoms (it will be the same for ^{56}Fe and ^{57}Fe) and is a fingerprint of the absolute magnetic moment of the atom. The full polarization analysis allows one to resolve the complete in-plane magnetization of the sample. In contrast to the NFS studies, we used PNR to determine the magnetic contrast between the metal and the oxide layers.

The nuclear forward scattering experiments where carried out at the nuclear

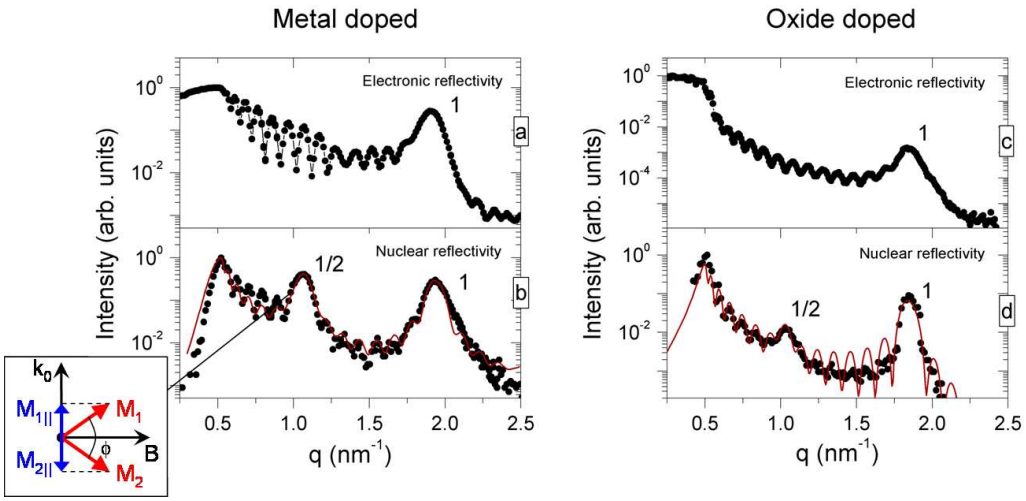

Figure 2. Electronic (a and c) and nuclear (b and d) X-ray reflectivity for the metal doped (a and b) and oxide doped (c and d) superlattices recorded with nuclear forward scattering. The red lines are fit. The appearance of superstructure half order Bragg peak accounts for a magnetic unit cell twice as large as the chemical one. The intensity of this peak is directly related to the difference in the projection of the two magnetic sublattices along the photon wavevector $\vec{k_0}$, as depicted in the inset of (b). In this case we found a canting angle between the magnetization of two adjacent Fe layers of 80° for the metal doped sample and an average canting angle of 20° between the magnetization of adjacent oxide layer in the oxide doped sample.

resonance beamline ID18 [18] of the European Synchrotron Radiation Facility (ESRF) in the 16 bunch mode of operation. The energy of the incoming photon was tuned to the ^{57}Fe nuclear resonance at 14.4 keV which corresponds to a photon wavelength of 0.862 Å. The polarized neutron reflectometry experiment was performed at the ADAM high resolution reflectometer [19] of the Institute Laue Langevin (ILL) where the wavelength of the neutrons was set to 4.41 Å.

4. Layer resolved magnetic structure

4.1. Nuclear forward scattering results

Major features of the magnetic structure in the Fe/FeO superlattice were revealed using the nuclear forward scattering technique (NFS) on the *metal doped* sample. A small magnetic field of 20 mT is applied parallel to the film surface and perpendicularly to the scattering plane to define the magnetization. As can be seen on Fig. 2b, a half order Bragg peak appears between the structural Bragg peak in the nuclear reflectivity. Its position accounts for a magnetic period two times larger than the chemical one and is indicative of non-collinear magnetization orientation in neighboring metallic Fe layers. In this geometry, the intensity of the half order Bragg peak is directly related to the difference in the projection of the magnetic hyperfine fields within the two magnetic sublattices along the photon wave vector $\vec{k_0}$ [20]. As depicted in the inset of Fig. 2b for

a symmetric opening of the magnetization of the two magnetic sublattices relative to the external magnetic field, the projection difference increases with increasing canting angle. The intensity of the 1/2 order peak therefore accurately determines the relative orientation of two adjacent Fe layers which is found to be around 80° in a 20 mT field. The nuclear reflectivity curves in Fig. 2 were fitted using the CONUSS program package for analysis of nuclear resonant scattering data [21]. A field dependent study [7] shows that the canting angle decreases only asymptotically with increasing external field. This type of behavior is described by the proximity magnetism model developed by Slonczewski [2] which assumes an AFM order in the spacer layer.

In the present case, the coupling is mediated by direct exchange interaction at the FM/AFM interface that is then transferred via the AFM order to the top ferromagnetic layer. Statistical variations of the thickness of the AFM layer results in a distribution of even or odd numbers of atomic planes in the AFM. Thus, the energetically favored configuration is a 90° coupling angle between the ferromagnetic layer, a value close to what is found in our experiment. Several other studies reported similar coupling behavior for trilayer systems [3, 4], where the 90° coupling is supposed to be sustained by a twist in the AFM to match the magnetization directions that are imposed by the exchange interactions at the adjacent interfaces. The occurrence of a correlated magnetic order over many bilayers implies a strong exchange coupling between the metal and the oxide.

The fact that the native oxide adopts an AFM ordering is quite surprising because the bulk Néel temperature of FeO is 198 K. However, as was established by van der Zaag et al. [22], the Néel temperature of thin AFM layers embedded between FM layers can drastically increase compared to bulk values to reach the Curie temperature of the surrounding FM in the limit of ultrathin films. In that case, the blocking temperature T_B below which exchange bias effects appear do not match T_N but is drastically reduced compared to the bulk case. Low temperature magnetization measurements indicated a blocking temperature of 70 K for our layer system, supporting the interpretation that the oxide is antiferromagnetically ordered at room temperature.

A similar nuclear reflectivity study was performed on the *oxide doped* sample, as shown on Fig. 2d. Surprisingly, a half-order Bragg peak is also observed, which indicates that a long range non-collinear magnetic order exists also within the oxide layers. A fit of this peak assuming a magnetically correlated system of oxide layers would yield an average canting angle of 20° between the magnetization direction in the oxide layers. However, the same fit could be obtained if one assumes that only a fraction (around 25%) of the moments in the oxide adopts a 90° canting angle while the rest of the layer remains in a compensated AFM state. Hence, this measurement does not provide a unique solution concerning the internal magnetic structure of the oxide. However, it still implies that the oxide layers exhibit a long range magnetic correlation throughout the layer stack, and indicates that parts of the oxide layer are not in a purely AFM state.

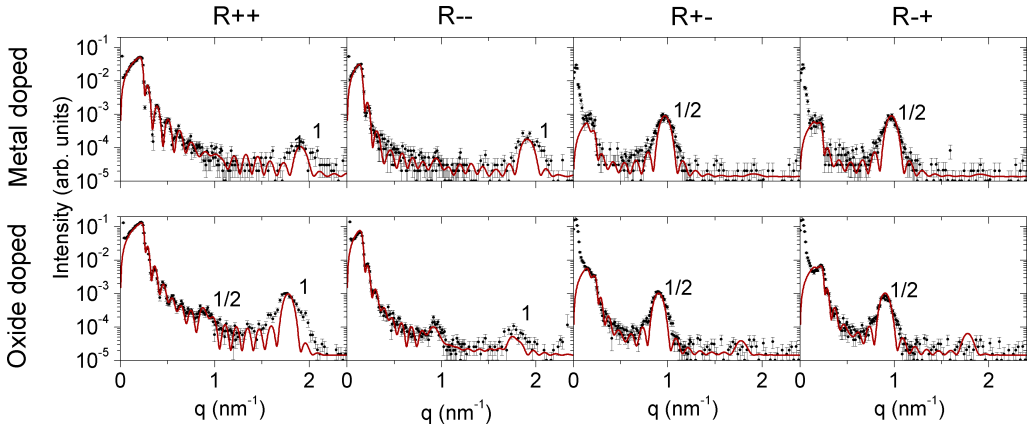

Figure 3. Polarized neutron reflectivity curves of the *metal doped* and oxide doped Fe/native oxide superlattices. The red lines are results of the fit. A magnetic field of 20 mT was applied in-plane of the sample and parallel to the neutron spin polarization. Top row: The appearance of 1/2 order Bragg peak in the spin flip channels evidences the non collinear orientation of the magnetization in adjacent Fe layers symmetric around the magnetic field direction. Bottom row: For the oxide doped sample, the presence of a small 1/2 order Bragg peak in the non spin flip channels indicates that the net magnetization of the oxide layers is not collinear with the external field.

4.2. Polarized neutron reflectivity results

The use of probe layers enables us to study the magnetic structure of defined part of the multilayers. The metal adopts a non-collinear coupling through an AFM like oxide which also possess some net magnetic moment. However, these informations were obtained on different samples. So far no direct information on the interaction between adjacent metal/oxide layers have been gained. In particular, the restriction of the information to the ^{57}Fe probe layers does not allow to distinguish the relative orientation of the net magnetization of the oxide compared to the metal. The same samples were therefore studied with polarized neutron reflectometry. A small magnetic field of 20 mT was applied along the hard axis and parallel to the neutron spin polarization in both cases. The two sets of reflectivity are shown on Fig. 3. The red lines are results of the least square routine [23] applied to simultaneously fit all four PNR curves to the theoretical model. The non-spin-flip (NSF) reflectivities (R++ and R−−) are mostly sensitive to the layer's magnetization parallel to the neutron spin (in this case parallel to the external field). The different positions of the critical edge for R++ and R−− directly relate to the net magnetization of the sample. For the metal doped sample, the scattering length densities of the metal and oxide layers (resulting from the weighted sum of the constituent species) are equal. This means that the first order Bragg peak observed here is of pure magnetic origin. The half order Bragg peak in the spin flip channels references to a coupling angle between the metal layers of 80°, symmetric around the direction of the applied magnetic field. The fit of the reflectivity curve indicates that the metal layer possess a magnetic moment of 2.15 μ_B per atom, a similar value compared to bulk

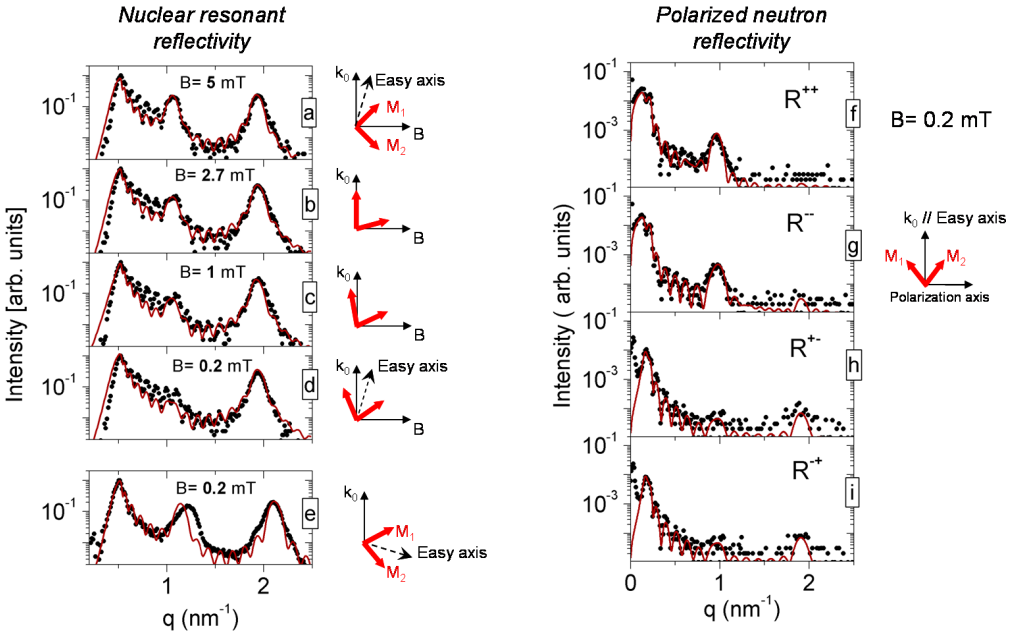

Figure 4. (a) to (d) Nuclear resonant reflectivity curve during magnetization reversal of the *metal doped* sample. The magnetic field is applied close to the hard axis and perpendicular to the scattering plane. The decrease of the half-order Bragg peak intensity account for a coherent rotation of the coupled moment as one unit. In remanence, the net magnetization is aligned on the easy axis. (e) The half order Bragg peak reappears once the sample is turned by 90°, confirming that the magnetic moments stay coupled in remanence. (f) to (i) Polarized neutron reflectivity in the remanent state. The 1/2 order peak appears now in the spin flip channels. A coupling angle of 70° in remanence is derived from both the NFS and PNR measurements

Fe ($2.2\,\mu_B$). The oxide also possesses a small net magnetic moment of $0.5\,\mu_B$ per atom pointing in the same direction as the net magnetization of the metal layers.

For the *oxide doped* sample, the situation is somewhat different. The presence of the half order Bragg peak in the spin flip reflectivity accounts for a canting of the metal layers which amounts here to 40°, a smaller value compared to the *metal doped* sample. Additionally, it is necessary to assume a non collinear spin arrangement in the oxide part of the layer to account for the small half order peak present in the non spin flip channels. In this case, the overall net magnetization of the oxide is perpendicular to the magnetic field. The reason for this phenomenon is not clear but might be due to small structural differences of the *metal doped* and *oxide doped* sample, the effect of which will be discussed in a later section.

5. Magnetization reversal

The hard axis magnetization reversal was monitored by taking NFS reflectivity curves of the metal doped sample at defined steps of the reversal. The corresponding curves are depicted on Figs. 4a to d, where the external field was applied close to the hard axis and

perpendicular to $\vec{k_0}$. In this geometry, the half order Bragg peak intensity is maximum when the magnetization of the two sublattices are symmetrically tilted to left and to the right with respect to the magnetic field. When the external field is reduced, the half order Bragg peak intensity decreases and almost vanishes in zero applied field. This could be due either to a reduction of the canting angle, domain formation or coherent rotation of the net magnetization of the total system (with constant canting angle) back into the easy axis direction. The first two possibilities can be ruled out by taking measurements with the sample rotated by 90° in remanence, as shown on Fig. 4e. In this case, the half order Bragg peak reappears and accounts for a 70° canting angle, indicating that the layers magnetization stayed canted through the magnetization reversal and that the net magnetization is now aligned along the easy axis. This is confirmed by a polarized neutron reflectivity curve recorded in remanence. As the position of the critical edge in the R++ and R−− channels is the same, we infer that there is no net magnetization along the hard axis. The half order Bragg peak accounts for a 70° canting angle in remanence. These measurements therefore confirm the canting angle found with the NFS data. However PNR allows to determine the magnetic moment per atom, which is found to be $2.15\mu_B$, the same value as was found prior to the magnetization reversal. This supports the notion of a coherent rotation of the coupled ferromagnetic layers as one unit.

The formation of small magnetic domains is also ruled out by a 2D mapping of the off specular diffuse neutron scattering. Magnetic domains usually lead to diffuse scattering sheets running across the magnetic Bragg peak [24]. As shown on Fig. 5, the absence of diffuse scattering in remanence accounts for magnetic domains that must be larger than $30\,\mu$m and can therefore be considered as macroscopic.

6. Discussion

From the results presented above, two particular properties of the oxide can be derived. First, the oxide layer always possesses some magnetic moment, although it is supposed to be in an antiferromagnetic state. Second, the uniaxial anisotropy induced by the oblique deposition of the ^{57}Fe probe layer influences the system differently, depending on whether the probe layer is embedded into the metal or into the oxide. In particular, it prevents the system from forming small magnetic domains in remanence.

According to the proximity magnetism model of Slonzcewski [2], the 90° coupling angle between adjacent Fe layers is the result of a competition between areas of differing interlayer thickness which favor either a parallel or anti parallel alignment of the FM layers. The coupling energy density W can be described by the following phenomenological equation.

$$W = C_+\theta^2 + C_-(\theta - \pi)^2 \tag{1}$$

where C_+ and C_- are constants related to parallel or anti parallel alignment. The energy

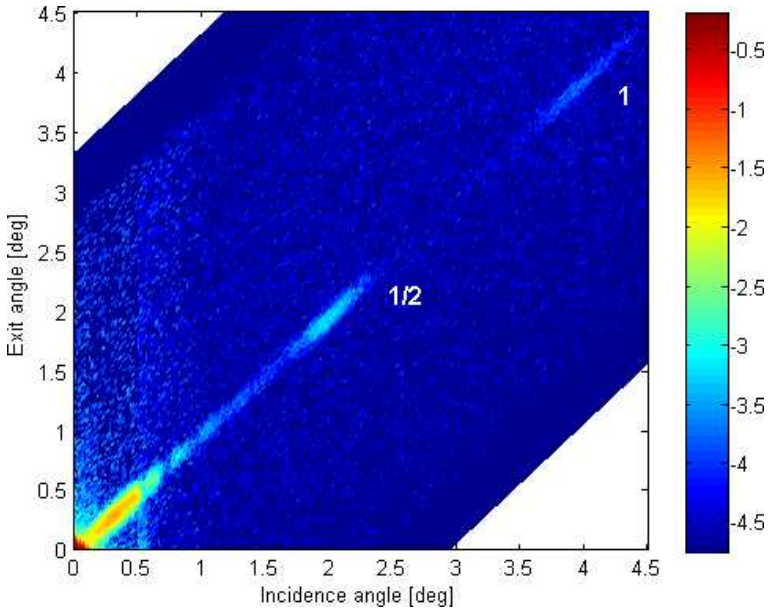

Figure 5. 2D scattering map measured on the *metal doped* sample in remanence. The specularly reflected beam is indicated by the ridge running along the diagonal on the graph. The absence of diffuse scattering around the half order Bragg peak indicates that the system does not decay into small magnetic domains. The lower limit for the domain size is estimated to be around 3 μm.

minimum of the system is found by setting the derivative of W to 0. That is:

$$\frac{dW}{d\theta} = 2C_+\theta + 2C_-(\theta - \pi) = 0 \tag{2}$$

which leads to the expression:

$$\frac{C_+}{C_-} = \frac{\pi - \theta}{\theta} \tag{3}$$

This equation shows that the important quantity to determine the canting angle in remanence is the ratio $\frac{C_+}{C_-}$. A 90° coupling angle minimizes the system energy if both thicknesses are present in the same fraction (*i.e.* $\frac{C_+}{C_-} = 1$). Physically , the interface coupling induces a twist of the AFM which differs depending on the number of AFM layers [3], as depicted in Fig. 6. In this case, the resulting net magnetic moment of the AFM is close to zero. For a polycrystalline layer, the twist is supposed to be confined to one grain [25] and only a very small net moment can eventually be expected at the grain surface. However, as we demonstrated recently [12], buried native oxide layers grown at room temperature incorporate a fraction of around 10% of Fe in a metallic state. In the case that the metallic regions are ferromagnetic and align to the external field, they could be responsible for the measured net moment in the oxide. This picture would be consistent with the findings that the coupling angle is below 90° in low magnetic fields, which indicates a larger value of C_+ and therefore a predominance of ferromagnetic coupling.

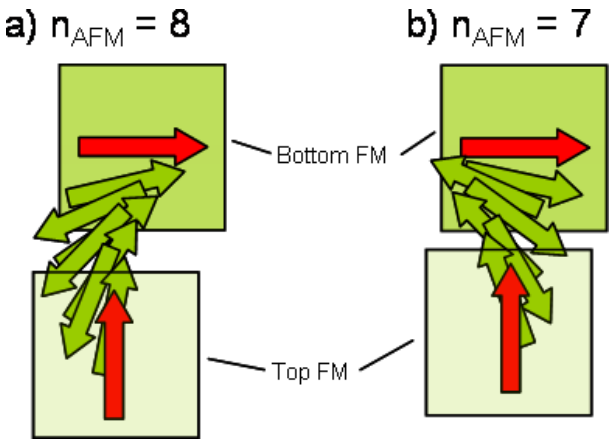

Figure 6. Two examples of possible twist structures in the AFM spacer layer when the magnetic moments of the surrounding metal layers are constrained to be non-collinear. Depending on the number of AFM atomic planes (even or odd), the rotation will occur clockwise or counterclockwise. The canting angle will deviate from the 90° coupling case if on the average the distribution of the layer thicknesses is not balanced.

The influence of the oblique deposition of the ^{57}Fe probe layers on the magnetic structure of the superlattice is somewhat more complicated to understand. It clearly provides a way to create a strong uniaxial anisotropy which allows one to have a well defined remanent state. However, it dramatically changes the magnetic structure of the oxide spacer layer when the ^{57}Fe probe layers are placed in its middle. According to equation 3 the reduced coupling angle of 40° between the metallic layers accounts for a ratio C_+/C_- larger than 4 which means that ferromagnetic coupling is greatly favored. This large proportion of FM coupling might be a hint of deviation from a pure proximity coupling through an AFM spacer. In particular, the oblique deposition of the ^{57}Fe might leave defects in the polycrystalline oxide layer which would allow for direct FM coupling through pinholes, as depicted on Fig. 7a. This direct pinhole coupling could then be responsible for the reduced coupling angle observed. This interpretation would also be in agreement with the more pronounced coupling angle measured on the metal doped sample. In that case, the ^{57}Fe probe layer is in the middle of the metal. As shown on Fig. 7b, defects in this layer would not influence the overall magnetic properties of the metal, and would therefore have little influence on the coupling through the AFM oxide.

7. Conclusions and outlook

Using a combination of isotope sensitive scattering methods, we have obtained a layer resolved magnetic depth profile in a superlattice composed of metallic Fe and its native oxide. The antiferromagnetic arrangement of the oxide spacer layers leads to a strong exchange coupling of adjacent metallic layers which is mediated by exchange interactions at the metal/oxide interfaces. The non-collinear arrangement is robust against external magnetic field and completely reversible. We measured the magnetization reversal with

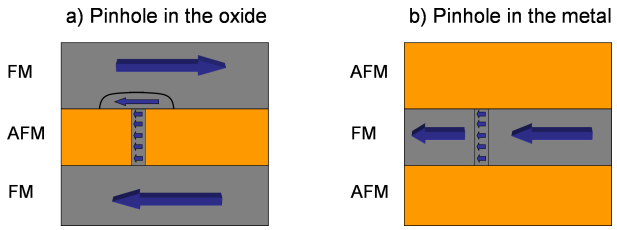

Figure 7. Schematic representation of the presence of defects in the oxide or in the metal layer. a) Pinholes in the AFM oxide layers leads to an effective ferromagnetic coupling between the two metal, reducing the overall coupling angle. b) A defect in the metal layer would not affect the overall magnetic structure but eventually leads to small reduction of the total moment.

the field applied along the hard axis, which takes place via coherent rotation of the coupled moments as one unit. Off specular neutron scattering confirmed that the system stays single domain in remanence and the decay into magnetic domains can be excluded within the resolution limit of the instrument. The presence of metallic Fe in the natively grown oxide can account for the observed net magnetic moment in the antiferromagnetic layer which tends to reduce the coupling angles between the metallic layers. We expect that removal of these clusters for example by mild thermal treatments should help to optimize the observed magnetic coupling properties. The ease of preparation of such MNOM systems and the strength of the 90° coupling could open interesting possibilities for spin engineering of magnetic layer systems.

The two nuclear techniques used here complement themselves ideally to study complex magnetic structures. x-ray based nuclear forward scattering is ideal to perform systematic studies of selected parts of the sample using isotopic probe layers while the sensitivity of polarized neutron reflectometry to the magnetic moment of atoms is ideally suited to take snapshots of the whole system in a defined magnetic state. These considerations should trigger further joint x-ray and neutron scattering studies of magnetic multilayer systems.

Acknowledgment

A.I. Chumakov and S. Stankov are gratefully acknowledged for their precious help during the nuclear resonant scattering experiment at ID18. Many thanks goes to M. Wolff who provided support and advices at the ADAM neutron reflectometer at the Institute Laue Langevin, Grenoble. H. Z. and B.T. acknowledge support from BMBF 03ZA7BOC.

References

[1] P. Bruno, Phys. Rev. B **52**, 411 (1995)
[2] J.C. Slonczewski, J. Magn. Magn. Mater. **150**, 13 (1995)
[3] P.A.A. van der Heijden, C.H.W. Swüste, W.J.M. de Jonge, J.M. Gaines, J.T.W.M. van Eemeren and K.M. Schep, Phys. Rev. Lett. **82**, 1020 (1999)

[4] A. Brambilla, P. Biagioni, M. Portalupi, M. Zani, M. Finazzi, L. Duò, P. Vavassori, R. Bertacco and F. Ciccacci, Phys. Rev. B **72**, 174402 (2005)
[5] J. Nogués and I.K. Schuller, J. Magn. Magn. Mater. **192**, 203 (1999)
[6] G.S.D. Beach and A.E. Berkowitz, IEEE Trans. on magnetics **41**, 2053 (2005)
[7] Th. Diederich, S. Couet and R. Röhlsberger, Phys. Rev. B 76, 54401 (2007)
[8] H.-C. Mertins, S. Valencia, A. Gaup, W. Gudat, P.M. Oppeneer and C.M. Schneider, Appl. Phys. A **80**, 1011 (2005)
[9] A. Nefedov, J. Grabis, H. Zabel, Phys. B: Condens. Mat. **357**, 22 (2004)
[10] R. Röhlsberger, H. Thomas, K. Schlage, E. Burkel, O. Leupold and R. Rüffer, Phys. Rev. Lett. **89** 237201 (2002)
[11] S. Couet, Th. Diederich, K. Schlage and R. Röhlsberger, submitted to Rev. Sci. Inst.
[12] S. Couet, K. Schlage, K. Saksl and R. Röhlsberger, Phys. Rev. Lett. **101**, 056101 (2008)
[13] M.T. Umlor, Appl. Phys. Lett. **87**, 82505 (2005)
[14] A.Q.R. Baron, Hyperfine Interact. **125**, 29 (2000)
[15] C.F. Majkrzak, K.V. ODonovan, N.F. Berk, *Neutron Scattering from Magnetic Materials*, Chatterji Tapan, Elsevier Science (2006)
[16] H. Zabel, K. Theis-Bröhl, B.P. Toperverg, *Polarized neutron reflectivity and scattering of magnetic nanostructures and spintronic materials*, Handbook of Magnetism and Advanced Magnetic Materials, Vol. 3 - Novel Techniques, H. Kronmüller, S.P.S. Parkin, Wiley, New York (2007), pp. 2327 - 2362
[17] A. Schreyer, R. Siebrecht, U. Englisch, U. Pietsch, H. Zabel, Physica B **248**, 349 (1998)
[18] R. Rüffer and A.I. Chumakov, Hyperfine Interact. **97/98**, 589 (1996)
[19] M. Wolff, K. Zhernenkov, H. Zabel, Thin solid films **515**, 5712 (2007)
[20] D.L. Nagy, L. Bottyán, L. Deák, E. Szilágyi, H. Spiering, J. Dekoster and G. Langouche, Hyperfine interact. **126**, 353 (2000)
[21] W. Sturhahn, hyperfine interact. **125**, 149 (2000)
[22] P.J. van der Zaag, Y. Ijiri, J.A. Borchers, L.F. Feiner, R.M. Wolf, J.M. Gaines, R.W. Erwinand M.A. Verheijen, Phys. Rev. Lett. **84**, 6102 (2000)
[23] B.P. Toperverg and V. Deriglazov, unpublished
[24] V. Lauter-Pasyuk, H.J. Lauter, B.P. Toperverg, L. Romashev, V. Ustinov, Phys. Rev. Lett. **89**, 167203 (2002)
[25] H. Xi, R.M. White, Phys. Rev. B **62**, 3933 (2000)

Bibliography

[1] G.S.D. Beach and A.E. Berkowitz, IEEE Trans. Magn. **41**, 2043 (2005)
Co-Fe metal/native oxide multilayers: A new direction in soft magnetic thin film design I. Quasi-static properties and dynamic response

[2] G.S.D. Beach and A.E. Berkowitz, IEEE Trans. Magn. **41**, 2053 (2005)
Co-Fe metal/native oxide multilayers: A new direction in soft magnetic thin film design II. Microscopic characteristics and interactions

[3] G.S.D. Beach, F.T. Parker, D.J. Smith, P.A. Crozier and A.E. Berkowitz, Phys. Rev. Lett. **91**, 267201 (2003)
New magnetic order in buried native iron oxide layers

[4] A.H. Morrish, John Wiley & sons, (1966)
The physical principles of magnetism

[5] P.W. Anderson, Phys. Rev. **79**, 350 (1950)
Antiferromagnetism. Theory of superexchange interaction

[6] J. Curély, Monatsh. Chem. **136**, 1013 (2005)
Magnetic orbitals and mechanisms of exchange II. Superexchange

[7] P.W. Anderson, Phys. Rev. **115**, 1 (1959)
New approach to the theory of superexchange interactions

[8] M.T. Johnson, P.J.H. Bloemen, F.J.A den Broeder and J.J. de Vries, Rep. Prog. Phys. **59**, 1409 (1996)
Magnetic anisotropy in metallic multilayers

[9] D. Sander, J. Phys.: Condens. Matter **16**, 603 (2004)
The magnetic anisotropy and spin reorientation of nanostructures and nanoscale films

[10] P. Grünberg, R. Schreiber, Y. Pang, M.B. Brodsky and H. Sowers, Phys. Rev. Lett. **57**, 2442 (1986)
Layered magnetic structures: Evidence for antiferromagnetic coupling of Fe layers across Cr interlayers

[11] J.C. Slonczewski, Phys. Rev. Lett. **67**, 3172 (1991)
Fluctuation mechanism for biquadratic exchange coupling in magnetic multilayers

[12] S.S.P. Parkin, N. More and K.P. Roche, Phys. Rev. Lett. **64**, 2304 (1990)
Oscillations in exchange coupling and magnetoresistance in metallic superlattice structures: Co/Ru, Co/Cr, and Fe/Cr

[13] Y. Yafet, Phys. Rev. B **36**, 3948 (1987)
Ruderman-Kittel-Kasuya-Yosida range function of a one-dimensional free-electron gas

[14] Z.-P. Shi, P.M. Levy and J.l. Fry, Phys. Rev. B **49**, 15159 (1994)
Interlayer magnetic coupling in metallic multilayer structures

[15] P. Bruno, Phys. Rev. B **52**, 411 (1995)
Theory of interlayer magnetic coupling

[16] J.C. Slonczewski, J. Magn. Magn. Mat. **150**, 13 (1995)
Overview of interlayer exchange theory

[17] R. Coehorn, Phys. Rev. B **44**, 9331 (1991)
Period of oscillatory exchange interactions in Co/Cu and Fe/Cu multilayer systems

[18] S.O. Demokritov, J. Phys. D: Appl. Phys. **31**, 925 (1998)
Biquadratic interlayer coupling in layered magnetic systems

[19] H. Xi and R.M. White, Phys. Rev. B **62**, 3933 (2000)
Coupling between two ferromagnetic layers separated by an antiferromagnetic layer

[20] L. Néel, Comptes rendus **255**, 1676 (1962)
Magnétisme - sur un nouveau mode couplage entre les aimantations de deux couches minces ferromagnétiques

[21] J.C.S. Kools, W. Kula, D. Mauri and T. Linn, J. Appl. Phys. **85**, 4466 (1999)
Effect of finite magnetic film thickness on Néel coupling in spin valves

[22] D.B. Fulghum and R.E. Camley, Phys. Rev. B **52**, 13436 (1995)
Magnetic behavior of antiferromagnetically coupled layers connected by ferromagnetic pinholes

[23] E.E. Fullerton, J.S. Jiang, M. Grimsditch, C.H. Sowers and S.D. Bader, Phys. Rev. B **58**, 12193 (1998)
Exchange-spring behavior in epitaxial hard/soft magnetic bilayers

[24] J. Meersschaut, C. L'abbé, F.M. Almeida, J.S. Jiang, J. Pearson, U. Welp, M. Gierlings, H. Maletta and S.D. Bader, Phys. Rev. B **73**, 144428 (2006)
Hard-axis magnetization behavior and the surface spin-flop transition in antiferromagnetic Fe/Cr(100) superlattices

[25] M.E. Filipkowski, J.J. Krebs, G.A. Prinz, C.J. Gutierrez, Phys. Rev. Lett. **75**, 1847 (1995)
Giant near-90 coupling in epitaxial CoFe/Mn/CoFe sandwich structures

[26] J. Als-Nielsen, D. McMorrow, John Wiley & Sons (2001)
Elements of modern x-ray physics

[27] R. Röhlsberger, Springer Tracts in Modern Physics, Vol. 208 (Springer-Verlag, Berlin, 2004)
Nuclear Condensed Matter Physics with Synchrotron Radiation.

[28] R. Röhlsberger, H. Thomas, K. Schlage, E. Burkel, O. Leupold and R. Rüffer, Phys. Rev. Lett. **89**, 237201 (2002)
Imaging the magnetic spin structure of exchange coupled thin films

[29] A.Q.R. Baron, Hyperfine Interact. **125**, 29 (2000)
Detectors for nuclear resonant scattering experiments

[30] D. Kmiec, B. Sepiol, M. Sladecek, M. Rennhofer, S. Stankov, G. Vogl, B. Laenens, J. Meersschaut, T. Slezak, M. Zajac, Phys. Rev. B **75**, 054306 (2007)
Depth dependence of iron diffusion in Fe_3Si studied with nuclear resonant scattering

[31] I. Sergueev, H. Franz, T. Asthalter, W. Petry, U. van Bürck, G.V. Smirnov, Phys. Rev. B **66**, 184210 (2002)
Structural relaxation in a viscous liquid studied by quasielastic nuclear forward scattering

[32] S. Stankov, R. Röhlsberger, T. Slezak, M. Sladecek, B. Sepiol, G. Vogl, A.I. Chumakov, R. Rüffer, N. Spiridis, J. Lazewski, K. Parlinski, J. Korecki, Phys. Rev. Lett. **99**, 185501 (2007)
Phonons in iron: From the bulk to an epitaxial monolayer

[33] R. Röhlsberger, T. Klein, K. Schlage, O. Leupold, R. Rüffer, Phys. Rev. B **69**, 235412 (2004)
Coherent x-ray scattering from ultrathin probe layers

[34] H. Zabel, K. Theis-Bröhl, B.P. Toperverg, *Polarized neutron reflectivity and scattering of magnetic nanostructures and spintronic materials*, Handbook of Magnetism and Advanced Magnetic Materials, Vol. 3 - Novel Techniques, H. Kronmüller, S.P.S. Parkin, Wiley, New York (2007), pp. 2327 - 2362

[35] C. L'abbé, J. Meerschaut, W. Sturhahn, J.S. Jiang, T.S. Toellner, E.E. Alp and S.D. Bader, Phys. Rev. B **93**, 037201 (2004)
Nuclear resonant magnetometry and its application to Fe/Cr multilayers

[36] W. Sturhahn, Hyperfine interact. **125**, 149 (2000)
CONUSS and PHOENIX: Evaluation of nuclear resonant scattering data

[37] R. Rüffer and A.I. Chumakov, Hyperfine Interact. **97/98**, 589 (1996)
Nuclear resonance beamline at ESRF

[38] `http://www.esrf.eu/UsersAndScience/Experiments/HRRS/NRG/beamline_layout/id18_layout`

[39] A. Snigirev, V. Kohn, I. Snigireva, B. Lengeler, Nature **384**, 49 (1996)
A compound refractive lens for focusing high energy X-rays

[40] S. Stankov, R. Rüffer, M. Sladecek, M. Rennhofer, B. Sepiol, G. Vogl, N. Spiridis, T. Slezak and J. Korecki, Rev. Sci. Instrum. **79**, 045108 (2008)
An ultrahigh vacuum system for in situ studies of thin films and nanostructures by nuclear resonance scattering of synchrotron radiation

[41] `http://www.ill.eu/adam/home`

[42] M. Wolff, K. Zhernenkov, H. Zabel, Thin solid films **515**, 5712 (2007)
Neutron reflectometry with ADAM at the ILL: Present status and future perspectives

[43] *X-ray Absorption Fine Structure for Catalysts and Surfaces*, ed. by Y. Iwasawa, World Scientific, Singapore (1996)

[44] A.L. Ankudinov, B. Ravel, J.J. Rehr, S.D. Conradson, Phys. Rev. B **58**, 7565 (1998)
Real-space multiple-scattering calculation and interpretation of x-ray-absorption near-edge structure

[45] A. Erbil, G.S. Cargill III, R. Frahm, R.F. Boehme, Phys. Rev. B **37**, 2450 (1995)
Total-electron-yield current measurements for near-surface extended x-ray-absorption fine structure

[46] C.H. Booth and F. Bridges, XAFS **XII** conference proceedings, Physica scripta **T115**, 202 (2005)
Improved self-absorption correction for extended x-ray absorption fine-structure measurements

[47] D.V. Dimitrov, K. Unruh, G.C. Hadjipanayis, V. Papaefthymiou, A. Simopoulos, Phys. Rev. B **59**, 14499 (1999)
Ferrimagnetism and defect clusters in $Fe_{1-x}O$ films

[48] R.M. Cornell, U. Schwertmann, Wiley VCH, 2nd edition (2003)
The iron oxides: Structure, properties, reactions, occurences and uses

[49] J. García and G. Subías, J. Phys: Conden. Matter **16**, R145 (2004)
The Verwey transition - a new perspective

[50] N.F. Mott, Trans. Faraday Soc. **43**, 431 (1947)

[51] A.T. Fromhold and E.A. Cook, Phys. Rev. **163**, 650 (1967)
Kinetics of oxide film growth on metal crystals: thermal electron emission and ionic diffusion

[52] G.W.R. Leibbrandt, L.H. Spiekman and F.H.P.M. Habraken, Surf. Sci. **287/288**, 245 (1993)
Temperature dependence of thin oxide film growth on Fe(110)

[53] B.J. Kooi, M.A.J. Somers and E.J. Mittemeijer, Thin solid films **281/282**, 488 (1996)
Growth kinetics of thin oxide layers: Oxidation of Fe and Fe-N phases at room temperature

[54] P.C.J. Graat, M.A.J. Somers, A.M. Vredenberg and E.J. Mittemeijer, J. Appl. Phys. **82**, 1416 (1997)
On the initial oxidation of iron: Quantification of growth kinetics by the coupled current approach

[55] G.W.R. Leibbrandt, L.H. Spiekman and F.H.P.M. Habraken, Surf. Sci. **287/288**, 250 (1993)
Plane-specific oxide stoechiometries on Fe single-crystal surfaces

[56] S.J. Roosendaal, B. van Asselen, J.W. Elsenaar, A.M. Vredenberg and F.H.P.M. Habraken, Surf. Sci. **442**, 329 (1999)
The oxidation state of Fe(100) after initial oxidation in O_2

[57] S.J. Roosendaal, A.M. Vredenberg and F.H.P.M. Habraken, Phys. Rev. Lett. **84**, 3366 (2000)
Oxidation of iron: The relation between oxidation kinetics and oxide electronic structure

[58] H.-J. Kim, J.-H. Park and E. Vescovo, Phys. Rev. B **61**, 15284 (2000)
Oxidation of the Fe(110) surface: An Fe_3O_4(111)/Fe(110) bilayer

[59] M. Busch, M. Gruyters, H. Winter, Surf. Sci. **600**, 2778 (2006)
FeO(111) formation by exposure of Fe(110) to atomic and molecular oxygen

[60] K. Mori, Y. Yamazaki, T. Hiraki, H. Matsuyama and K. Koike, Phys. Rev. B **72**, 014418 (2005)
Magnetism of a FeO(111)/Fe(110) surface

[61] H.-J. Kim, J.-H. Park and E. Vescovo, Phys. Rev. B **61**, 15288 (2000)
Oxidation of the Fe(110) surface: An Fe_3O_4(111)/Fe(110) bilayer

[62] K. Koike and T. Furukawa, Phys. Rev. Lett. **77**, 3921 (1996)
Evidence for ferromagnetic order at the FeO(111) Surface

[63] L.Q. Pan, G.M. Zhang, C.F. Fan, H. Qiu, P. Wu, F.P. Wang, Y. Zhang, Thin solid films **473**, 63 (2005)
Fabrication and characterization of Fe3O4 thin films deposited by reactive magnetron sputtering

[64] T.G. Knorr and R.W. Hoffman, Phys. Rev. **113**, 1039 (1959)
Dependence of geometric magnetic anisotropy in thin iron films

[65] M.T. Umlor, Appl. Phys. Lett. **87**, 82505 (2005)
Uniaxial magnetic anisotropy in cobalt films induced by oblique deposition of an ultrathin cobalt underlayer

[66] E. Partyka-Jankowskaa, B. Sepiol, M. Sladecek, D. Kmiec, J. Korecki, T. Slezak, M. Zajac, S. Stankov, R. Rüffer and G. Vogl, Surf. Sci. **602**, 1453 (2008)
Nuclear resonant scattering studies of electric field gradient in Fe monolayer on W(110)

[67] J. Nogués and I.K. Schuller, J. Magn. Magn. Mater. **192**, 203 (1999)
Exchange bias

[68] P.J. van der Zaag, Y. Ijiri, J.A. Borchers, L.F. Feiner, R.M. Wolf, J.M. Gaines, R.W. Erwinand M.A. Verheijen, Phys. Rev. Lett. **84**, 6102 (2000)
Difference between blocking and Néel temperatures in the exchange biased Fe_3O_4/CoO system

Acknowledgment

At the end of three years of research at HASYLAB and DESY, I am indebted to many people who helped, supported or encouraged me during the course of this thesis. Before giving a personal word to some of the most important people which contributed to the success of this work, I would like to mention that being here at DESY was a great opportunity for me. Being in such motivated scientific environment opened for me unexpected perspectives and showed how challenging and fascinating the world of research can be. For that I am already grateful to all the people that welcomed me at HASYLAB.

First of all, I would like to thanks PD Dr. Ralf Röhlsberger, Prof. Dr. Hans Peter Oepen and Prof. Dr. Wilfried Wurth for supervising and reviewing this doctoral thesis.

My best thanks goes to PD. Dr. Ralf Röhlsberger, who supervised my work during these three years. I cannot be thankful enough in regards of the knowledge I gained from working with him. Although he was busy with other duties, he always considered my questions and requests with great attention. This usually lead to exciting discussion on current results and future experiments. Within his group, I discovered how fascinating experimental physics was, and i am already looking forward for many more joined experiments in the future.

The next two persons I would like to thank are the two postdocs which worked with me during this thesis. First come, first serve: Big thanks goes first to Dr. Thomas Diederich, who worked with me in the first year of my stay at DESY. I gained and learned a lot from his experience. I learned how to prepare correctly experiments involving "lab transfer" to Grenoble, and especially to think about every little things which should not be forgotten in such case! Thanks to his teaching, this kind of experiments were successfully reproduced at various places later on. It was always a pleasure to work with him. The second person is Dr. Kai Schlage, which almost directly succeeded Thomas. This last two years where really a big fun working with him. His extensive knowledge in magnetic multilayers, nuclear resonant scattering, and Mecklenburg-vorpommern came just on time for passionated discussion. His constant good mood and support made him a truly reliable co-worker and friend. I hope we will continue working together sometimes in Hamburg. Maybe then we can see the Hansa again in the arena...

I would also like to give my best thanks for the support I receive from the people working at the various beamlines I used in the course of this thesis. I can easily say that none of those experiments would have been made possible

without their outstanding support. At first, I would like to thank the complete team of the Nuclear resonance beamline ID18 from the ESRF, especially Dr. Rudolf Rüffer, Dr. Aleksandr Chumakov, Dr. Svetoslav Stankov and Dr. Cornelius Strohm. Thanks to them, it was always a success and a pleasure to come to Grenoble! At HASYLAB, the many people who helped me during various experiments are greatly acknowledged. In particular big thanks goes to Dr. Edmund Welter and Dr. Darius Zajac, which were of great help during the preparation of the XAFS experiment at the A1 beamline. I would also like to thanks Dr. Oliver Seeck and Dr. Wolfgang Caliebe for their help during the different x-ray reflectivity experiments carried out at the D4 and W1 beamline. It also happened to me to drift into the world of polarized neutron reflectometry. I would therefore like to thanks all those who helped me making my first steps in this field (both from the experimental and theoretical point of view) : PD. Katharina Theis-Bröhl, Dr. Boris Toperverg and Kyril Zhernenkov are greatly acknowledge.

In *experimental physics*, one can find the word *experimental*, which somehow incorporates all the "delay generating" problem one meets when performing experiments. This thesis would never have accomplished (in time) without the great technical support from the HASYLAB staff in general. In particular I would like to thank Heiko Schultz-Ritter, which was always first advisor in case of UHV related design, and sometimes problem. In the same way my big thanks go to Ernst Untiedt, from the vacuum group, which was always most prompt to help. From the electronic side, Rudiger Nowak deserves the honor, as he always has matching answers to technical problems. The people from the HASYLAB workshop should be thanked for their outstanding work, in regard of the many (usually last minutes) requests I made there.

One can do many, but not everything with hard x-rays. I would therefore like to thanks several people who helped at different occasion during this thesis by providing important measurements that were not possible to obtain at HASYLAB. In particular, many thanks goes to Dr. Armin Kleibert (Rostock university) who gived me an introduction in MOKE magnetometry and soft x-ray XMCD measurements at BESSY. Enrico Bucholz (Rostock university) performed the combined GMR and MOKE measurements presented in this work and is greatly acknowledge for all the help he provided there. Shengqiang Zhou (Forschungszentrum Dresden-Rossendorf) is greatly thanked for providing the low temperature SQUID measurement which allowed to discover the occurrence of exchange bias effect in Fe/Fe-oxide multilayers.

In principle nobody can work a complete day without a (short) entertaining break. For that reason, I guess I have to mention all the people I met on the first floor of 25C for top level discussions on "multiple scattering of spherical particles". Printing a list of names would, however, be too long!

What would be a good work experience without friendly neighbor? I want to thank all the people I spend my time with during my stay at HASYLAB: Bente, Fabian, Wojcieh, Marcin, Agnes, Kai, Lorenz, Ulla, Cristian, Bernd and all the people from the *second floor mafia*. It was a pleasure working with you, and I hope

we will meet again (eventually to finish the discussions mentioned in the previous paragraph).

Finally, I would like to give a special thanks to my family and my friends from Belgium. Thanks for all the supports, and the fun of course, you always provided me. A special thanks goes to Marie, who somehow succeeded to speed up my writing in the last months of this great adventure :-D Merci!